Degradation and Defects in Plasma Facing Components for Future Fusion Devices

Von der Fakultät für Maschinenwesen
der Rheinisch-Westfälischen Technischen Hochschule Aachen
zur Erlangung des akademischen Grades einer Doktorin
der Ingenieurwissenschaften genehmigte Dissertation

von

Anna Kapustina

aus Sewerodwinsk (Russland)

Berichter:
apl. Prof. Dr.rer.nat. F. Schubert
Univ.-Prof. Dr.-Ing. L. Singheiser

Tag der mündlichen Prüfung:
24. Mai 2004

“Degradation and Defects in Plasma Facing Components for Future Fusion Devices”

Anna Kapustina

Abstract

The main function of the first wall and the divertor are to remove the power generated by the plasma and to shield from neutrons. The plasma facing components (PFCs) are optimised the high heat flux energy removal. PFCs are composed of a thick armour joined to an actively cooled heat sink to provide the necessary transfer of the incident power to the cooling system. During normal operation these components have to dissipate a heat flux up to 5 MW/m^2 in the divertor and 0.5 MW/m^2 on the first wall. During short time off-normal events these loads can locally rise up to 20 MW/m^2. Consequently, only materials with excellent thermal properties and sufficient thermal shock resistance are tolerated in these regions. Three materials, beryllium, carbon fiber composites (CFCs) and tungsten, are selected as candidates for armour materials in the fusion facility ITER.

For basic studies of PFC heat transfer properties inspection and quality control an infrared inspection facility (IRINA) has been installed. The impact of local differences in emissivity of the armour materials on temperature measurements was studied. To compensate local temperature variations originating from emissivity inhomogeneities of the most specimens a temperature correction method was applied successfully. On different components defect zones with reduced heat transfer properties could be detected. In the combination with FE-calculations a correlations between defects within the component and the measured temperature field was found. On this basis the minimum temperature difference between intact and defect zones for detection by IR analysis could be given.

The heat transfer in defect areas of plasma facing components has been tested in the electron beam facility JUDITH under cyclic loads with different configurations. Special emphasis has been given on the thermal fatigue behavior of CFC flat tile divertor modules. Two regimes of surface temperature increase rate were detected. It was found that slow temperature increase characterizes small structure imperfections growing with thermal fatigue. A strong surface temperature increase indicated catastrophic crack propagation leading to armour detachment.

The heat transfer reduction of beryllium armoured modules during cyclic loading has in general been not detected. The tested first wall modules did not shown degradation of heat transfer rate during 1000 cycles at 1.5 MW/m^2. It was shown that complete failure of beryllium tiles progressed with heat flux $\geq$ 2 MW/m^2 during a few seconds. The reasons of failure were found to be joint damages including cracks, the formation of intermetallic phases and high thermal stresses.

Additionally, the neutron induced heat transfer degradation of tungsten and carbon-based modules was investigated. It was found that neutron irradiation did not reduced the heat transfer ability of tungsten armoured plasma facing components under static loads remarkable. But the heat transfer reduction of irradiated CFC modules was significant. It is caused by a strong decrease of thermal diffusivity of C-based materials after neutron irradiation. During cycling at loads of 10 MW/m^2 the surface temperature of irradiated CFC modules slightly decreased with time. It indicates an improvement of the that heat transfer properties due to annealing effects of armour material. The heat transfer degradation of irradiated modules due to thermal fatigue were observed at lower loads compared to non-irradiated reference samples.

Degradation und Defekten in plasmabelasteten Komponenten künftiger Fusionsanlagen

Anna Kapustina

Kurzfassung

Die grundlegenden Funktionen der ersten Wand und des Divertors bestehen in der Abfuhr von im Plasma erzeugter Wärme und der Neutronenabschirmung. Die plasmabelasteten Wandkomponenten (PFCs) sind für die optimale Abfuhr der hohen Wärmeströme an das Kühlsystem ausgelegt und bestehen aus einer dicken Armierung, welche auf eine aktiv gekühlte Wärmesenke aufgebracht ist. Im normalen Betrieb müssen diese Komponenten einen Wärmestrom von 5 MW/m² im Divertor und 0,5 MW/m² an der ersten Wand abführen. Zusätzlich werden kurzzeitige lokale Fehlbelastungen von bis zu 20 MW/m² auftreten. Daher können lediglich Werkstoffe mit hervorragenden thermischen Eigenschaften und ausreichendem Thermoschockverhalten in diesen Bereichen eingesetzt werden. Für ITER sind die drei Werkstoffkandidaten Beryllium, kohlefaserverstärkte Graphite (CFC) und Wolfram vorgesehen.

Im Rahmen der vorliegenden Arbeit wurde ein Infrarot-Teststand (IRINA) aufgebaut um grundlegende Untersuchungen zum Wärmetransport in den PFCs durchzuführen und darauf aufbauend eine Qualitätskontrolle zu entwickeln. Zunächst ist der Einfluss von lokalen Emissionsunterschieden auf die Temperaturmessung analysiert und eine Korrekturmethode zur Kompensation lokaler Ungleichmäßigkeiten erfolgreich eingeführt worden. An unterschiedlichen Komponenten konnten somit Bereiche mit geminderter Wärmeabfuhr bestimmt werden. Mit der Hilfe von FE-Berechnungen wurde eine Korrelation zwischen Defekten innerhalb der Komponenten und den gemessenen Temperaturfeldern erstellt. Dies ermöglichte die Festlegung eines minimalen Temperaturunterschiedes zwischen intaktem und fehlerbehaftetem Gebiet für eine erfolgreiche Defektzuordnung mittels IR-Analyse.

Die Wärmeabfuhr in den fehlerbehafteten Gebieten der PFCs wurde weiterhin in der Elektronenstrahlanlage JUDITH mit unterschiedlichen Lastzyklen untersucht. Spezielles Augenmerk galt dabei den CFC-Flachziegel-Modulen für den Divertor, wobei zwei Bereiche mit unterschiedlichem Temperaturanstieg als Funktion der Zyklenzahl mit Vorgängen innerhalb der Komponenten in Korrelation gestellt werden konnte. Ein langsamer Temperaturanstieg beschreibt demnach langsames Defektwachstum während ein schneller Temperaturanstieg mit massivem Risswachstum einhergeht und das baldige Versagen der Komponente ankündigt.

An Beryllium Modulen wurde eine Reduktion der Wärmeabfuhr im allgemeinen nicht festgestellt. Nach 1000 Zyklen mit 1,5 MW/m² zeigten die Bauteile der ersten Wand keinerlei Degradationserscheinungen. Es konnte jedoch gezeigt werden, daß Belastungen oberhalb 2 MW/m² innerhalb weniger Sekunden zum vollständigen Versagen der Flachziegel führen. Versagensursachen treten dabei in Form von Fehlern oder Rissen an den Fügezonen, der Bildung intermetallischer Phasen und hohen thermischen Spannungen, in Erscheinung.

Zusätzlich ist der Einfluss von Neutronenschäden auf die Wärmeabfuhr von Wolfram- und CFC-Modulen untersucht worden. Es zeigte sich, daß Neutronenbestrahlung die Wärmeabfuhr von plasmabegrenzenden Komponenten mit Wolfram Armierung nicht wesentlich beeinflusst. Dagegen war die Reduktion der Wärmeabfuhr bei CFC-Modulen beachtlich, hervorgerufen durch eine starke Abnahme der Wärmeleitfähigkeit des Kohlenstoff-Werkstoffs nach der Bestrahlung. Nach einigen Belastungszyklen mit 10 MW/m² nahm die Oberflächentemperatur der CFC-Module jedoch mit der Zeit langsam ab. Dies deutete auf eine Verbesserung der thermischen Leitfähigkeit des Werkstoffs hin, hervorgerufen durch thermische Erholungseffekte. An den zuvor bestrahlten Modulen konnten thermische Ermüdungserscheinungen bereits bei geringeren Belastungen beobachtet werden, als an den unbestrahlten Referenzproben.

Acknowledgments

I would like to thanks Univ.-Prof. Dr.-Ing. L. Singheiser for the possibility for the doctoral research in the Institute for Materials and Processes in Energy Systems (IWV2), for the lively interest and precious assistance during all the years of my research.

I also want to thank Prof. Dr. rer. nat. F. Schubert for reviewing and adding valuable critique of this PhD thesis.

I am grateful to Dr. J. Linke and Dr. M Roedig for being my scientific supervisors and a great influence on my thinking and practical advises. Similarly, Dr. T. Hirai and Dr. P. Majerus gave me a great for support and input.

I would like to thank Dr. A. Bukaemskiy for his support and criticisms, especially concerning the empirical part. The thesis would have been impossible without him. I would also like to express my personal admiration for his personality and his work.

W. Kühnlein and H. Münstermann deserve special recognition for carrying out of the electron beam experiments. Special thanks must be given to Gaby Gutzeit for realization of laboratorial experiments and Gerd Boeling for building and service of the infrared facility IRINA. My special thanks to Paul Joecken for technical support and making sure that the computer does not let me down.

And certainly I am very grateful to all the staff of IWV2 for their valuable participation in my research during 3 past years. Similarly, I greatly appreciate the support and attention of all my friends.

I would like to thank my sister Maria Kapustina for her assistance and insightful encouragement over the years.

My mother and farther deserve much more than I can express here; they have provided unflinching backing and patience. I dedicate this work to them.

Table of symbols:

t_W – pipe wall temperature, °C;

t_F – fluid temperature, °C;

w – fluid velocity, m/s;

v – fluid viscosity, m^2/s;

λ - thermal conductivity, W/(m K);

d_r – pipe wall diameter, m;

l – pipe wall length, m;

Pr - Prandtl number;

Nu- Nusselt number;

Re- Reynolds number;

α_k – heat transfer coefficient, $W/(m^2K)$;

χ – thermal diffusivity, m^2/s;

ρ – fluid density, kg/m^3

Contents

Chapter 1. Introduction

1.1. Energy demand and environment

Estimating for the year 2050 the population of the world to be 9 billion and basing on the equal distribution of the resources amongst the countries at the present average of Organisation for Economic Cooperation and Development (OECD) countries levels of consumption, the world would consume 2 to 7 times of the present amount of natural resources [1]. This estimations, and many other forecasts make it clear that the level of the world´s dependency on the energy will certainly increase over time. On the basis of available knowledge today, the world has enough coal, oil, and gas till the end of the centuries [2]. The problem of the ecological limits of these types of natural resources puts forward a greater concern.

The two major environmental concerns are acid rain and the 'greenhouse effect'. The power industry has a main responsibility for the emission of sulphur dioxide (SO_2) and nitrogen oxides (NO_x) resulting in acid rain. The greenhouse effect is caused by a number of different pollutant gases in the atmosphere. One of the most important is carbon dioxide (CO_2).

1.2. Fusion as an energy source

Due to the above mentioned problems scientists are devoting much effort to searching for new energy sources. In the last decades attention was focused on the development of controlled thermonuclear fusion energy. Fusion needs hydrogen, i.e. its two isotopes, deuterium and tritium, as fuel. Deuterium can be easily extracted from seawater. Tritium can be bred from lithium, which is abundant in the earth's crust. Even a very small mass of fuel can yield a considerable amount of energy. The fusion energy released from just 1 g of deuterium and tritium mixture equals the energy from about 10 t of oil. Additionally, the use of fusion energy is not associated with the release of CO_2 or other greenhouse gases, with smog, or with acid rain.

1.3. R&D for ITER

The actual project in this field is the international experimental fusion reactor ITER. ITER is a joint scientific project of the EU, USA, Russia, Japan, Canada, South Korea and China. The aim of ITER is to demonstrate the possibility of energy production on an industrial scale using fusion reactions in magnetic confinement experiment. The beginning of the construction of ITER is foreseen for 2005. The major candidates to host the reactor are France and Japan.

A major issue in the construction of the experimental reactor is the safe and reliable operation under forecasted work conditions. As second important task is the development of the plasma facing materials and components for the inner wall of plasma vessel, which have to ensure reliable operating under extreme heat loads. Several materials and solutions for plasma facing components were developed.

A further task of vital importance is the analysis of new materials and improved design solutions. Therefore, it is a technical challenge to undertake a profound analysis of the physical and mechanical properties of the commercially available and newly developed materials and design solutions and of their behavior under heat and irradiation influence. These investigations allow to select the best solutions for plasma facing components (PFCs) with highly reliable performances. The investigation itself gives additional necessary information about required material properties. One of the effective methods to calculate and optimize the technological solutions is the method of numerical modelling.

Moreover, an important issue is the quality control of PFCs. The surface of the plasma vessel consists of more than 400 shield modules with about 200 primary first wall panels, and 54 divertor cassettes with about 2600 units of vertical targets and 54 dome/liner components. The costs of changing and repairing of the PFCs can be expected to be high as well as it will arise additional technological problems. Thus, to avoid unnecessary technological difficulties and expenses, it is required to measure and to improve the effectiveness of heat transfer by each of the components to choose the most reliable ones. Therefore, it is necessary to adapt existing nondestructive methods to PFCs and to find new approaches for the quality control of PFCs. High heat flux simulation experiments in electron or ion beam test facilities represent an important tool for the analysis of actively cooled components. Another new approach is infrared thermography.

Figure 1 - 1 schematically presents the methods which are used nowadays for the detection of defects in industrially produced PFCs.

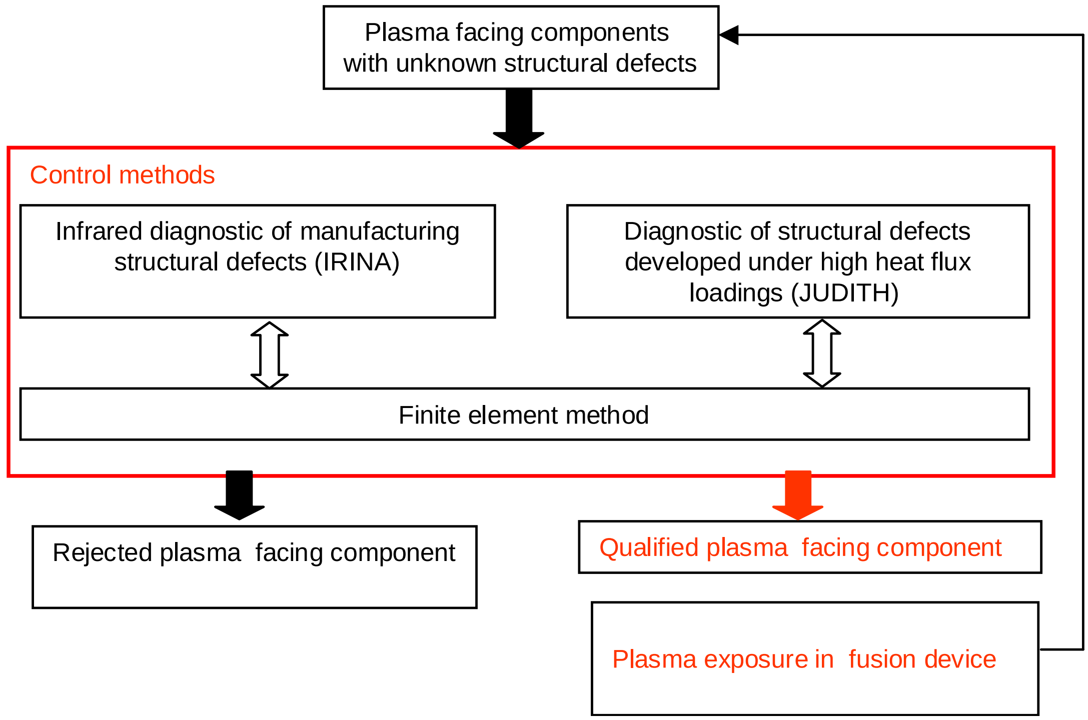

Figure 1 - 1. Procedure of quality control of plasma facing components

1.4. Scope of the work

The considerations above pose several important questions concerning the development and investigation of PFCs. This work seeks to find appropriate technological solutions by solving the following tasks:

1. to develop and to construct a facility for nondestructive control of heat transfer properties in PFCs based on infrared thermography;
2. to develop criteria which determine the heat transfer efficiency of water cooled PFCs;
3. to investigate the heat transfer degradation of different types of PFCs under high heat flux loads in the electron beam facility JUDITH;
4. to study the heat transfer properties of plasma facing components with different armour materials and geometries and to define possible reasons for thermal fatigue failure of PFCs;
5. to investigate the heat transfer degradation in plasma facing components induced by neutron irradiation;
6. to simulate structural defects and their impact on heat transfer using finite element methods.

Chapter 2. Background

2.1. Physical foundation of fusion

The fusion takes place continuously in the sun and the stars. In the core of the sun at temperatures of 1-1.5 keV (10-15x10^6 K), hydrogen is converted to helium. For the energy production on earth, different fusion reactions have been proposed. The most suitable reaction occurs between the nuclei of the two isotopes of hydrogen - deuterium (D) and tritium (T) [3]:

$$D + T \rightarrow {}^{4}He\ (3.5\ MeV) + n\ (14.1\ MeV) \qquad (2-1)$$

The fusion of 1 g of tritium (together with 2/3 g of deuterium) produces 1.6x10^5 kWh of thermal energy [4]. Deuterium exists at 0.0153 at.% in the water and thus it is an almost unlimited fuel source. Tritium undergoes beta decay with a half-life of 12.5 year. Thus it must be produced artificially, for example, by neutron capture in lithium.

10 g of deuterium can be extracted from 500 liters of water and 15 g of tritium from 30 g of lithium, would produce enough fuel for the lifetime electricity needs of an average person in an industrialized country.

At the temperatures required for the D-T fusion reaction - >50-100x10^6 K (i.e., 5-10 keV) - the fuel changes its state to plasma. Fusion reactions occur with a sufficient rate only at very high temperatures. More than 100x10^6 K are needed for the deuterium-tritium reaction whilst other reactions require even higher plasma temperatures. The hot plasma must be well isolated from material surfaces in order to avoid releasing material atoms (impurities) that would contaminate and cool down the plasma. Since plasma consists of two types of charged particles, ions and electrons, magnetic fields can be used to isolate the plasma from the vessel walls. In a magnetic field the particles move along the field lines but diffuse only slowly across them. The most promising magnetic confinement systems have a toroidal configuration (ring-shaped). Among these, the most advanced concept is the tokamak configuration. JET (Joint European Torus), Culham, UK is the largest Tokamak in the world.

Once a critical ignition temperature for nuclear fusion is achieved, it must be maintained for a sufficient confinement time with a high ion density to obtain a net yield of energy. In 1957, J. D. Lawson showed that the fusion product of ion density $\boldsymbol{n}$ and confinement time τ determined the minimum conditions for productive fusion. Lawson's criterion [5] for equal mixtures of a D-T fuel above 10 keV is:

$$n\tau \geq 10^{20}\ \mathrm{s\ m^{-3}} \qquad (2-2)$$

The value of $n\tau$ is a minimum for which the fusion reaction continues in the plasma without an external energy supply.

Numerical values for D-T Reaction are:

- Plasma temperature (T): 100-200 x 10^6 K
- Energy confinement time (τ): 1-2 s
- Central plasma density (n): 2-3 x 10^{20} particles m^{-3} (~1/1000 g/m^3)

2.2. Fusion experimental facilities

ITER (Figure 2 - 1) is a collaborative project carried out by the EU, Japan, the Russian Federation and Canada. In the beginning of the year 2003, the United States came back to the negotiating table (it had withdrawn from the project in 1999 in order to make a reassessment). China and South Korea have also joined the project in 2003. The objectives of this project are to demonstrate the scientific and technological feasibility of a fusion power plant.

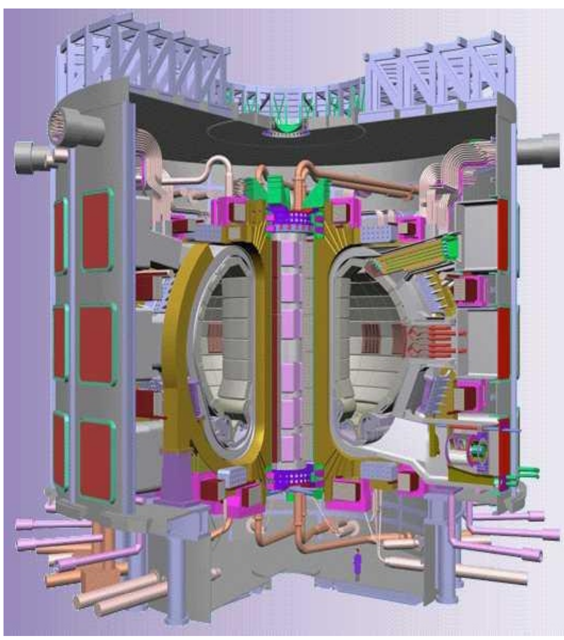

Figure 2 - 1. ITER design [6]

In order to construct and to run a fusion reactor, three main steps are planed: ITER, DEMO and finally – a commercial reactor.

First step: The ITER project aims to solve three main technological problems: first, demonstration of thermonuclear fusion energy production under the current technological capacities; second, tests and demonstration of the following critical technologies: i.e. superconducting magnet systems, plasma facing components (PFC), which are subjected to high heat and neutron fluxes, tritium fuelling and handling systems; third, functional tests of breeding blanket concepts. When ITER is constructed, it is supposed to produce 500 MW (thermal energy) of fusion power during 400-500 s pulses.

Second step*:* The aim of DEMO (demonstration reactor) is to generate electric energy in the range of 1000-1500 MW. The physics and engineering developed on ITER will be applied to DEMO. However, a DEMO reactor based on the ITER technology would not be economically competitive to conventional commercial power stations using fossil fuel and fission will be taken into account [7].

Third step: It is expected that within this century the fusion power plant will be utilized commercially to obtain energy.

According to the current design [7], more than 400 shield modules with about 200 primary first wall panels, and 54 divertor cassettes with about 2600 units of vertical targets and 54 dome/liner components will be produced in the ITER construction phase. Eight years of design and research and development efforts enabled to establish the manufacturing of the components in accordance with design and operation requirements [8] .

2.3. Main parameters and design of ITER

The latest parameters of ITER are summarized in Table 2 - 1 [7,8].

Table 2 - 1. Main ITER parameters

Fusion power	500 MW
Q=fusion power/additional heating power	≥10
Average 14 MeV neutron wall loading	0.6 MW/m^2
Plasma inductive burn time	400 – 500 s
Plasma major radius (R)	6.2 m
Plasma minor radius (a)	2.0 m
Plasma current (I_p)	15 MA
Toroidal field (BT)	5.3 T
Plasma volume	837 m^3
Plasma surface area	678 m^2

First wall: the major part of the vacuum vessel is covered with primary first wall (PFW) modules each with a thickness of 450 mm, and a surface area of around 2 m^2. The components have flat surfaces. They are composed of a thick stainless steel (SS) shield block, a copper alloy heat sink cooled by water flowing in SS tubes and armour beryllium on the plasma facing side. The first wall absorbs heat radiation from the plasma as well as provides neutron shielding [11].

The PFW will be loaded by a moderate heat flux and also will be exposed to the highest neutron load of 0.7 dpa. During plasma disruption and vertical displacement events (VDE), the PFW will also be subjected to thermal shocks and to high electromagnetic loads. Coolant pressure stresses are minimized by usage of circular channels [10].

ITER will operate with a shielding blanket which two main functions are:

- to absorb most of the neutron energy and the particle energy generated by the plasma;
- to provide shielding of the vacuum vessel structure and superconducting coils.

Blanket modules are attached to the vessel. Each module is connected to a permanent water cooling manifold by two tubes. Stainless steel and pressurized water provide the necessary shielding against the neutron flux. The modules consist of a separate first wall, made of flat panels, joined to a steel shielding block. When modules are repaired, often only the first wall or part of it will need to be replaced, so this approach minimizes the operational waste. The modules are maintained by a special remotely driven invessel transporter inserted through the equatorial port.

The PWF panels need to sustain ~30 000 burn pulses with a duration of ~400 s at average surface heat loads of 0.25 MW/m^2 and peak values of 0.5 MW/m^2.

Divertor: at the bottom, the vacuum vessel accommodates the divertor cassettes (Figure 2-2) that are composed of the vertical targets and the dome/liner as the plasma facing components (PFC). The vertical targets intersect with the separatrix (i.e the magnetic surface, that divides the closed plasma from the open one, intersects the material walls), and they are, therefore exposed to substantially higher surface heat loads than the PFW. The PFCs have triplex structures like the PFW panels. However, they have to be curved, and need to combine Cu alloy coolant tubes and plasma facing armour to cope with the high heat fluxes. Both tungsten alloys and carbon fiber reinforced composites (CFCs) are used as plasma facing materials at the inner and outer vertical target. The dome/liner components are located in between, and its surfaces are covered with W alloy.

The main function of the divertor system is to exhaust He and impurities from the plasma [9]. The main components of the divertor system are (Figure 2- 2):

- inner and outer vertical targets, which are the plasma-facing components (PFCs) and in their lower part interact directly with the scrape-off layer plasma and in their upper part act as baffles for the neutrons;
- PFCs in the private flux region (i.e. the space below the separatrix that has no flux line connections to the main plasma) consist of a dome, reflector plate, liner:
- a dome, located below the separatrix X-point, facing main radiation and charge exchange neutrals;
- inner and outer neutral particle reflector plates;
- a semi-transparent liner that protects the cassette body from direct line-of-sight of the plasma, allowing He and other impurities to be pumped away;
- a divertor cassette body, that is reusable to minimize activated waste and provides neutron shielding and a mechanical support for different possible arrangements of plasma interfaces:

The divertor cassette is designed to provide a neutral particle pressure reduction of 10^4 between the divertor and the main chamber and of 10 between the private flux region below the dome and above the dome.

According to code simulations, for steady-state scenarios up to 136 MW of thermal power is delivered via the scrape-off layer onto the targets. Preliminary simulations indicate a peak heat flux of about 15 MW/m^2. Although the targets can certainly sustain this heat load since they are rated to handle transient (10 μs) heat flux perturbations of up to 20 MW/m^2, it will have a reduced lifetime [9].

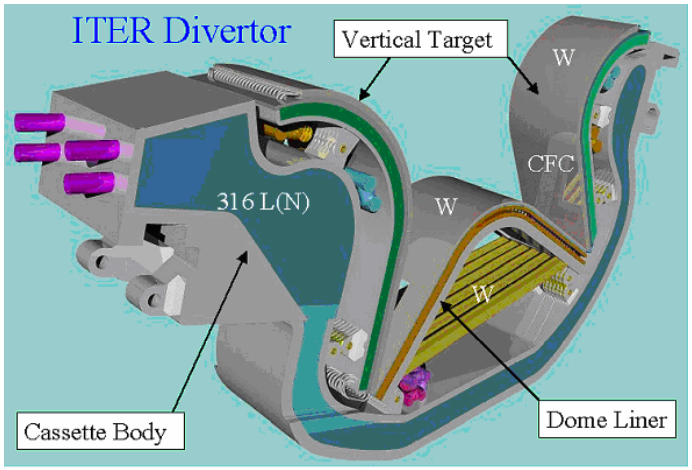

Figure 2- 2. ITER Divertor [10]

The divertor components are designed for ~3000 cycles and heat loads up to ~5 MW/m^2 and peak value of 20 MW/m^2 in the regions which are covered by carbon fiber composite (CFC) and tungsten [11]. CFC has been selected as the reference armour for the strike point regions of the divertor. The absence of melting at high power operational conditions (slow transients and disruptions) and therefore the potential of higher erosion lifetime, and the proven thermo-mechanical performance at high heat fluxes of CFC led to this choice [18]. Tungsten has been selected for all other plasma-facing surfaces of the divertor, for the baffle regions of the target and the surface of the dome where there are charge-exchange neutrals, because of its low sputter yield, and for the private region PFCs because of its low tritium retention and high melting temperature.

Loads*:* Table 2 - 2 summarizes the operation conditions for these components [8].

Table 2 - 2. Operation conditions for ITER high heat flux components [8, 9]

Component	Armour material, geometry and thickness	Max heat loads	Neutron damage and He production in the armour, ion/atom flux (D-T) and energy
Divertor vertical target: upper region	W macrobrush or W monoblock (10 mm)	3 MW/m^2x 3 000 discharges of 400 s duration. Possible runaway electrons up to 25 MJ/m^2. *	0.7 dpa, 0.4 appm He, 10^{20}-10^{21}/m^2s, 10-100 eV
Divertor vertical target: lower region	CFC monoblock (15 mm)	10 MW/m^2 x 3 000 discharges of 400 s duration. One in ten discharges 20 MW/m^2 during the 10 s slow transients. One in ten discharges ending in a major disruption (up to 30 MJ/m^2 of 1 ms duration)	0.7 dpa, 230 appm He, <10^{24}/m^2s, <15 eV
Dome	W macrobush (10 mm)	3 MW/m^2x 3 000 discharges of 400 s duration. 20 MW/m^2 during the slow transients for a 10 s duration. Possible runaway electrons up to 25 MJ/m^2. *	0.5 dpa, 0.3 appm He, 10^{21}-10^{22}/m^2s, 10-100 eV
First Wall	Be flat tile	0.25 MW/m^2 x 30000 discharges of 400 s duration. Peak values of 0.5 MW/m^2[8]	

* Possible VDE after each major disruption (up to 60 MJ/m^2 of 100-300 ms duration).

2.4. Divertor- and First Wall – Components

2.4.1. Geometry and materials used for plasma facing components

The actual important issue is to investigate the thermal fatigue performances of plasma facing components (PFCs), designed for heat removal in the form of electromagnetic radiation and fluxes of neutrons, electrons, neutrals, and ions produced by the plasma in plasma vessel of a fusion reactor. A plasma facing component consists of an armour (plasma facing material with high heat transfer properties and thermal resistance) and a heat sink (a material with high thermal conductivity) removed the heat to the cooling cannels. Armour is joined to heat sink via HIP or brazing. There are two geometrical options for the plasma facing components – the so-called monoblock and the flat tile design. Monoblocks are made from armour material and a cooling tube, located inside the monoblock.

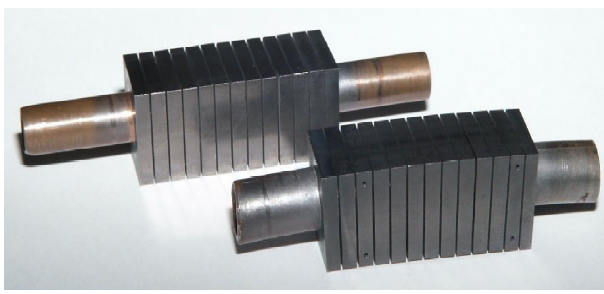

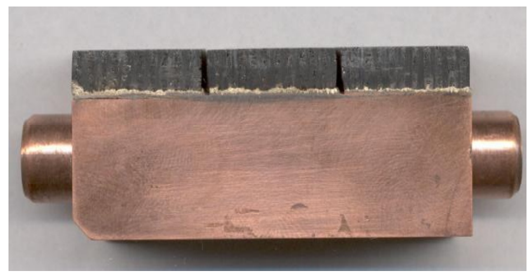

Figure 2 - 3. A monoblock and a flat tile mock-ups

Monoblocks are typically 15-20 mm thick (armour thickness). Flat tiles have a heat sink made from a material with good thermal conductivity (normally Cu alloy) or stainless steel and attached to armour (thickness of 10-15 mm). A cooling tube is drilled in the heat sink (Figure 2 - 3). Both options have normally a swirl tape inside the cooling tubes to raise the critical heat flux limit by a factor about 1.6 [8]. Moreover, other coolant channel configurations are considered to provide an acceptable critical heat flux, including hypervapotrons, screw tubes and channels with porous coating [11].

Main material groups were chosen as armour material: CFC, beryllium and tungsten. The components with plasma facing materials CFC and tungsten are intended for divertor, where the heat loads reach up to 20 MW/m^2. Beryllium PFCs will be installed in first wall of a reactor, where the armour is exposed to 0.5 MW/m^2.

Carbon fiber composites armour

Carbon fiber composites (CFCs) are consisted of two components: carbon fibers and a carbon matrix. CFCs have better mechanical properties than graphite and have the excellent machinability. CFCs are, however significantly more expensive than graphites. CFC materials are categorized into uni-directional (1D), two-directional (2D), or three-directional

(3D), indicating the number of the directions of fiber bundle. In a 3D CFCs the fiber bundles are usually mutually perpendicular [12].

The manufacturing of CFCs involves two basic processing steps: production (weaving, lay-up, needling, etc.) and densification. The CFCs are prepared from carbon fibers derived from either pitch or PAN and generally have diameters in the range of 7-15 µm. The woven perform is converted into a densified composite material by repetitive impregnations, using resins or pitch, followed by carbonisation and graphitisation. Alternatively, densification can be achieved using chemical vapor infiltration (CVI) or a combination of pitch or resin impregnation and CVI. Typically, the final density achieves the range of 1.9-2.0 g/cm^3. The entire production process takes up to nine months from the preparation until final machining. A typical 3D CFC has a fiber volume fraction <50 %, distributed in the three fiber axes, and additionally will contain approximately 35 % impregnant derived matrix graphite.

The rest of the composite volume is occupied by porosity, which is distributed in the fiber bundles, between them, and in the matrix pockets.

Several factors influence on the properties of CFCs, including fiber types, preform designs, matrix precursor, and processing history. The properties of CFCs, particularly the electrical resistivity, thermal conductivity, strength and coefficient of thermal expansion are strongly influenced by the final heat treatment [13].

There are two dominant types of carbon fibers, polyacrylonitrile-based (PAN-based) and mesophase pitch-based. PAN is a linear polymer containing highly polar nitrile pendant groups. Because of its highly polar nature, pure PAN has a glass transition temperature of ca. 120°C and tends to decompose before sublimation. Therefore, PAN precursor fibers must be produced by either wet- or dry-spinning processes using highly polarized solvents. The peculiarities of pitch-based fibers are the direct result of the precursor and the process used to convert it to fiber. In this case, the precursor is mesophase pitch, a liquid crystalline material consisting of large polynuclear aromatic hydrocarbons [14].

A systematic development of high thermal conductivity CFCs has been carried out in the framework of the European Fusion Research and the Development Program. A series of commercial available CFCs were used for investigation on high heat flux behaviors, neutron effect on thermal conductivity, mechanical properties, tritium retention, oxygen reactivity and plasma compatibility [15].

As CFC armour for high heat flux components, EU industries have developed several advanced materials (SEP NB31 and NS31, Dunlop Concept 1 and 2) with the following main features [16]:

- high thermal conductivity (about 350 and 150 W/m K at 20 and 800°C, respectively) in one direction along pitch fibers;

- 3D fiber structure with high resistance to thermal shock events and to neutron-induced swelling [12].

The specific issues associated with the operation of the ITER PFCs with CFC armour are: erosion lifetime due to chemical sputtering and erosion during disruptions and vertical displacement events (VDEs), the life time of the CFC-heat sink material joints at very high heat fluxes, and changes of the CFC thermal properties due to neutron irradiation (mainly thermal conductivity) [8]. The utilisation of CFC armour is mainly limited by tritium retention and by radiation damage due to neutron at 0.7 dpa [16].

NB31 is produced by SEP (France). 3D CFC constituted a NOVOLTEX preform, with P55 ex-pitch fibers in x direction and ex-PAN fibers in y direction; needling with PAN fibers in perpendicular direction (z). The volumetric fraction of fibers is 35% (27% in x direction, 4% in y and z directions). This 3D structure is densified with pirocarbon through a CVI (Chemical Vapour Infiltration) process. The densified material is heat treated at 2800°C to make it high conductive. The final treatment is densification at 1000°C with pitch coke. Total amount of impurities: less than 100 ppm, ash content less than 0.01% [17].

SEP N31 is developed also by SEP (France). This 3D CFC constituted of P55 ex-pitch fibers (80% vol.) in one direction and ex-PAN fibers (20% vol) in the perpendicular direction; this CFC undergoes a subsequent needling which gives a fibers orientation in the third direction (z direction). The high thermal conductivity direction is that of the P55 ex-pitch fibers. NS31 is densified by chemical infiltration of pyrocarbon and heat treated at a temperature > 2500°C. Finally, liquid silicon is injected under pressure leading to the formation of silicon carbide. NS31 contains about 8-10% at. of silicon and its porosity is about 3-5%. The resulting material consists of a mixture of elemental Si, SiC, CVI carbon and carbon fibers [17]. Silicon reduces chemical erosion, tritium retention and the reactivity with oxygen [15]

Tungsten armour

Tungsten has been selected for the lower baffle, the divertor dome, the cassette liner and the upper part of the vertical target. The higher threshold energy for physical sputtering causes smaller erosion under the high density and low temperature divertor plasma [18].

The divertor target erosion lifetime of tungsten was estimated to be 1400-4500 pulses, based on 50 disruptions in total with 10% melt layer loss. Due to the melt layer loss, W armour is proposed in areas with moderate off-normal heat loads.

Plasma spraying (PS) is one of the options for applying a coating of tungsten to the copper heat sink. Problems, related to the manufacturing of thick tungsten coatings on copper substrates, are the low adhesion values and the high residual stresses that follow the deposition process due to the difference in the thermal expansion coefficient, which is 4 times smaller for tungsten than for copper. For ITER application a thickness of at least 5 mm of PS W is required. The PS W/Cu joints should withstand the operational heat fluxes. Moreover, the additional requirements of low porosity and low oxygen content are deemed necessary to obtain a high quality coating.

Tungsten coated tiles, manufactured by plasma spray on graphite, were mounted in the divertor of the ASDEX Upgrade (Axial Symmetrisches Divertor EXperiment), Garching (Germany) and exposed to approximately 800 plasma discharges at heat fluxes of up to 6 MW/m^2. After the experimental campaign, cracks were detected on almost all tiles. The W-coated tiles in the inner divertor were found to be covered by deposited layers of low-Z material with thicknesses in the µm range and only a few percent tungsten remaining on the surface. In contrast to this deposition pattern erosion dominates the outer target area, where the surface tungsten content was found to be unaltered compared to the initial surface composition [19].

Since 1998 an area of tungsten coated tiles has been installed at the central column of ASDEX Upgrade. The W-coating was applied on carbon tiles by plasma arc deposition to a thickness of 1 µm. The post-mortem analyses of the W-coating show that the erosion is mainly due to ions, consistent with the spectroscopic measurements, that show increased W-influx during plasma ramp-down [20].

Beryllium armour

Beryllium metal was discovered at first by the French chemist, L.N.Vauquelin in 1798. For more than a century, beryllium was extracted only in comparatively small amounts and sufficient quantity of the metal is available since 1920.

Beryllium is one of the strongest of the light metals, lighter than aluminium with a stiffness 40% higher than steel. The high melting point of beryllium (1285°C) enables it to be used effectively at temperatures where the other light metals will soften or melt. In addition, beryllium has excellent electrical and thermal conductivities with high specific heat. Beryllium has an outstandingly low absorption cross-section to thermal neutrons.

Of the available processes, vacuum hot pressing of powder is often used for the production of primary beryllium billets and for further processing. The blocks are machined to final shape by rolling, extrusion, forging or other hot working processes. The metal must, in any case, be coated to prevent oxidation if they are used at very high temperatures [21].

Three main areas of beryllium application in fusion reactors are the first wall protective armour, neutron multiplier in a solid breeding blanket, and some invessel components of the plasma diagnostics system [22].

Beryllium has been used with success as an armour in plasma-facing components in Joint European Torus (JET). PFCs have sustained in total, several thousand full power plasma discharges. Thermal fatigue has been studied for a variety of geometries, including thin castellated layers bonded to a heat sink. It is found that the tokamak environment admits more severe localised loading of these PFCs leading to local melting and microcracking of small regions. The large area failures of loaded surfaces were seen under test bed conditions have not been produced by PFC exposed to plasma in JET [23].

Beryllium was selected as the reference armour for all plasma facing components (PFC) at the beginning of the ITER engineering design activity. However, the divertor target erosion life-time was found to be only <100 pulses due to melting under off-normal transients [13]. The main reasons for the selection of beryllium are the plasma compatibility, good oxygen gettering probability, absence of chemical sputtering (in comparison with carbon), low bulk tritium inventory, and the possibility of in-situ (or in hot-cell) repairing of damaged surfaces using plasma spray. The main function is to protect the actively cooled wall structures from high heat fluxes and direct contact with plasma in order to satisfy the required component lifetime and plasma compatibility [22].

Commercially available beryllium grades from the USA and from the RF have been selected as candidate materials. Among various grades, S-65C VHP (vacuum hot pressed) grade (Brush Wellman Inc., USA) has been selected as a reference grade. The main reasons were lowest BeO and metallic impurity content among the other grades; high ductility at elevated temperature and excellent cycling thermal fatigue performances, and thermal shock resistance. The similar grade DShG-200 (manufactured by the RF) was selected as a backup. The basic properties of these grades can be found elsewhere[22].

The key issue for the application of Be as armour is its degradation due to neutron irradiation and critical damage during thermal transient heat loads. Embrittlement of Be at low temperature could lead to brittle destruction of the tiles and influence on the erosion of Be during transient heat loads. The studies on Be S-65C VHP confirm that this grade has best thermal shock resistance [22].

The disadvantage of beryllium and its compounds is that they are highly toxic, producing chronic and acute respiratory diseases that can be fatal. Fine particles of beryllium, that may be produced in machining, cutting, filing or heating, are the main danger. Extremely small amounts of beryllium can cause chronic berylliosis [21].

Another key problems in the application of Be armour in ITER first wall was the development of the bonding of Be–Cu alloys. The main issue is that Be reacts with almost all metals at moderate and high temperatures and forms brittle intermetallic compounds that are critical to reliability of joining and fatigue lifetime. To solve this problem and to provide good quality Be/Cu joints, different approaches have been studied. The results are described in chapter 3. In recent years, the main efforts were performed in the field of the optimisation of joining technology, manufacturing and testing of various mock-ups [22].

Cu heat sink PH-Cu and DS-Cu

The heat sink of the high heat flux components in ITER is interposed between the armour and the cooling circuit. The main functions of the heat sink are to transport elevated heat fluxes to the cooling water and to reduce thermal stresses in the structural material.

Due to their excellent thermal conductivity, copper alloys are the obvious choice for the heat sink. Currently, two classes of copper alloys are investigated as a candidate for ITER: precipitation hardened copper alloy PH-Cu (CuCrZr-IG) and alumina dispersion hardened copper DS-Cu (CuAl25-IG) (IG-ITER Grade) [24].

Cu-Cr-Zr alloys exhibit the best combination of high strength and, good electrical and thermal conductivity of any copper alloy. The proposed composition of CuCrZr alloy differs from the standard one mainly by its narrower range of the Cr (0.6–0.9%) and Zr (0.07–0.15%) contents. The reason for limiting the Cr is that it may result in the formation of coarse Cr precipitates which affect the radiation resistance. Zr promotes the hardening of the alloy by providing a good homogeneity of precipitates; moreover, it influences the aging time and the recrystallisation temperature. Based on industrial experience the reference ITER heat treatment for CuCrZr–IG is as follows: solution anneal at 980–1000°C for 1 h, water quench then age at 450–480°C for 2–4 h. Aging could be performed either before, during or after the component manufacturing [25].

The finely dispersed alumina particles in DS-Cu alloys provide an extremely stable microstructure which can retrain a cold worked structure at elevated temperatures. GlidCop® is the trade name for the dispersion strengthened copper alloys commercially produced by OMG Americas Corporation. The alloy GlidCop® CuAl25 is comprised of a pure copper matrix with a small amount of Al (0.25%) in the form of extremely fine Al_2O_3 (3 to 12 nm in size) dispersed throughout the matrix. The insoluble oxide particles in the matrix make the alloy resistant to recrystallization, allowing the material to maintain excellent strength and ductility up close to the alloy's melting temperature. A high temperature annealing (at 950°C) is performed after cross-rolling [26].

2.4.2. Joining techniques

The design of the ITER plasma facing components (PFCs) includes various combinations of joints between armour and Cu alloy heat sink materials. The joints must withstand the cyclic thermal mechanical loads and neutron loads under vacuum, providing at the same time an acceptable lifetime and high reliability [13].

The main requirements to the joints will limit the scope of the joints that can be possibly used. Among these requirements are:

1. residual stresses from the manufacturing process cause the additional thermal stress in joint during operation [27]. Materials with low difference in elastic modulus and

coefficient of thermal expansion have to be used. Joining methods have to be modified to reduce residual stresses;

2. due to high fluxes of 14 MeV neutrons irradiation in the plasma vessel Ag cannot be used as a braze material in ITER (transformation to Cd by neutrons). Silver free brazing materials have to be found [28];
3. joining interlayer materials used for the formation of an efficient joint between two different materials should have a high reactivity with the armour and the heat sink;
4. during the joining process the good mechanical properties of a Cu-heat sink have not to be damaged (for example, the heat treatments may affect the physical and mechanical properties of CuCrZr by dissolution and/or coarsening of the precipitates).

The PFC operating conditions in the ITER are summarised inTable 2-3.

Table 2 - 3. Operational conditions for the joints in ITER PFCs [29]

Components	Joints	Heat flux (MW/m^2)	Number of pulses	Neutron fluence (MWa/m^2)	Damage armour/Cu (dpa)	Maximum temperature of joints (°C)	
						Steady state	Transient
First wall	Be/Cu	0.25-0.5	10 000	0.3	1/3	230	~<600
Limiter	Be/Cu	$(3.4\text{-}8)^a$-0.5	10 000[b]	0.3[b]	1[b]/3	350-200	~<600
Baffle	Be/Cu	1-2	10 000	0.17	0.6/1.7	280	~<600
	W/Cu	1.5-3	10 000	0.15	0.5/1.5	280	~<600
Divertor	CFC/Cu	10-20	~3000	0.06[b]	0.3[b]/0.6	300	~<500
	W/Cu (VT, D)	1-5	~3000	0.18[b]	0.016[b]/0.5	300	~<600
	W/Cu (L)	0.1-0.7	~3000	0.15	0.1[b]/0.4	250	-

[a] During start-up/shut down [b] Without planned replacement

VT – vertical target, D- dome, L- limiter

One of the critical problems in joints is the combination of materials and processes used. This problem is particularly severe for the brazing of CFCs to copper alloys. Due to the large difference of coefficients of thermal expansion, CFCs and copper alloys are typically brazed with reactive metal (e.g., Ti-Cu) at 800-850 °C. Cooling from the braze process produces high residual stresses that can initiate subsequent cracking during service. The problem of residual stresses can be suppressed by braying at low temperature with reactive metals.

Other techniques to reduce residual and thermal stresses are (a) castellation (segmentation) of the armour and (b) compliant interlayers that undergo plastic deformation during fabrication [30].

Several joining technologies will be discussed in detail in the following sections.

Be/Cu-alloy joining technologies

The most critical characteristic of beryllium from a viewpoint of joining is its high reactivity. Beryllium forms stable compounds with almost every element in the periodic Table. These compounds are typically hard and brittle; their presence in a joint can degrade mechanical properties such as ductility and toughness. Also, beryllium oxidizes very easily in air. Therefore, in order to form appropriate metallurgical bonds, the bonding surface of beryllium must be cleaned (i.e. removal of the surface oxides) and kept clean throughout all handling and processing steps until the bonding process is complete [30].

To solve the problem of the extensive formation of the brittle phases and provide the good quality of Be/Cu joints different combinations of materials have been investigated:

- materials as fillers or interlayers between Be and Cu alloy that do not form intermetallic phases with Be (e.g. Al, Ge, Si) or with intermetallic phases (AlSi or AlBeMet);
- diffusion barrier materials with less affinity to the formation of beryllide intermetallics;
- materials as fillers or interlayers with high ability for reaction (e.g. Cu) to control the formation of the intermetallic phases by process parameters [13].

Several techniques for Be/Cu joining were developed:

1. Vacuum plasma spraying of beryllium on copper

   One of the requirements for selecting a joining process will be the feasibility of large scale flat and curved surfaces of beryllium to copper alloy. Plasma spray coating can be an option. It has been identified for beryllium as a potential primary or backup technology to fabricate the armour on the primary and limiter first wall modules. Advantage is the potential for providing thick armour coatings directly on large flat and curved copper surfaces. Even in-situ repair possibilities are given [30].

2. HIP joining with interlayers

   Hot Isostatic Pressing (HIP) is a process that uniquely combines pressure and temperature to produce components from diverse materials, including metals and ceramics. During the manufacturing process, materials are placed in a container, typically a steel can. The container is subjected to elevated temperature and a very high vacuum to remove air. The application of high inert gas pressures and elevated temperatures results in the removal of internal voids and creates a strong metallurgical bond throughout the material. Low temperatures and high isostatic pressures yield a controlled grain growth and generate isotropic properties. This results in the high performance characteristics.

   Good thermal fatigue performance of a Be/DS-Cu/SS structure fabricated by solid HIPing has already been achieved using intermediate layers for a primary wall small scale mock up [31]. The use of a Ti interlayer as a diffusion barrier material with a few hundreds micron coating of pure Cu (OFHC Cu) and HIPed at 580 °C, 60 MPa, 2 h seems to be promising [36].

3. Brazing

The good quality of the Be/Cu joints produced by induction brazing with the use of Ag–Cu (InCuSil-ABA) brazing alloy has been reported by Ibott et al. [32]. Brazing with Ag- or Cu-based alloys at temperatures above 700°C was investigated by Frankoni et al. [33]. The Be/Cu joint quality after conventional furnace heating and induction heating with Ag–Cu brazing alloy has been studied. It was concluded that the quality of joints is much better after induction brazing. But use of Ag as brazing alloy was forbidden due to transformation to Cd. It makes necessary the development of the other brazing materials.

The use of a diffusion barrier (e.g. Al) explosive welded to Be and then brazed with AlSi to a Cu alloy was investigated and have also shown a promising resistance to high heat fluxes [31].

Different types of silver-free brazing technologies have been developed for ITER. CuMnSnCe, CuMn, TiZr, CuInSnNi alloys have been studied. All these alloys have been applied together with fast heating technologies (via induction brazing or heat by e-beam). The metallurgical quality and, more important, high heat flux performance are acceptable [34].

W/Cu-alloy joining technologies

The main problems in the development of W/Cu joints are the large difference in the elastic modulus (408 GPa for W vs. 84 GPa for Cu) and coefficient of thermal expansion between the two materials ($4x10^{-6}$/K for W vs. $18x10^{-6}$/K for Cu). This results in large thermal stresses during the cooling phase from the bonding temperatures. With conventional flat tile geometry, this difference creates very large stresses at the interface [29].

This was evidenced in early attempts to bond a tungsten plate (7 mm thick) to a copper heat sink. High residual stresses caused deformation and cracks in the interface between tungsten and copper. The second challenge is that relatively low bonding temperatures (<500°C) are required by the copper alloy heat sink material. The CuCrZr is hardened to optimum strength in the 480°C range by aging. Overaging occurs rapidly above 500°C and results in the degradation of the mechanical properties. As a result, it will be necessary to apply solution annealing at 1000°C and a rapid quench, what brings again distortion and residual stress problems.

The most reliable process for W/Cu joints proved to be casting of a pure Cu layer, followed by electron beam welding onto the heat sink. However, this is only applicable for flat tiles [8].

The US approach to these fabricational challenges utilizes a tungsten brush structure which is joined to the Cu heat sink. In this technique, tungsten rods (1.7 or 3.25 mm in diameter) are hold in position by Inconel honeycomb core. The brush is a design that accommodates the large difference in coefficient of thermal expansion between W and Cu. Various coatings are applied to improve the bond strength of tungsten-copper. The precoated rods are then bonded to the copper heat sink using diffusion bonding techniques. Currently the most favourable technique is HIP. The HIP temperature is commensurated with the aging characteristics of the CuCrZr heat sink alloy (450~480°C). The heat sink material is clad with 3 mm thick OFHC copper, that provides a soft compliant layer for the tungsten rods. The resulting deformation at the interface enhances the diffusion process and results in a larger bonding surface [30].

The EU and Russian Federation Home Teams fabricated the brush tiles by casting pure Cu onto W pins. The Cu and W brush composite is then e-beam welded (EU Home Team) or CuMn fast brazed (RF Home Team) to the Cu heat sink [35].

CFC/Cu-alloy joining technologies

The problem in the development of CFC/Cu joints is the even larger difference in the coefficient of thermal expansions of materials to be jointed. This difference generates high joint interface stress during manufacturing and operation. The fact, that Cu does not wet carbon, prevents direct casting. The first issue is handled by means of a pure Cu soft interlayer between the CFC and the CuCrZr heat sink. The absence of wetting is overcome by a proper activation of the CFC surface prior to casting or by using a brazing alloy with good wetting characteristics. Several joining technologies have been developed and studied [36].

1. Brazing of CFC/Cu materials

   Brazing with silver-free alloys (e.g., CuMn, Cu SiAlTi, Ti-Cu-Ag) is usually applied at 800-850°C. Cooling from the braze cycle produces high residual stresses that can promote subsequent cracking during service [30].

   The Ti–15Cu–15Ni brazing alloy with liquidus temperature at 960 °C was used by Appendino [37]. The brazing temperature is below the copper melting point and above the maximum working temperature foresees in the heat sink. Furthermore, the presence of titanium in the alloy improves the wettability and the adhesion to the CFC substrate, while the absence of silver is mandatory.

2. Active metal casting onto the CFC surface and HIP of CFC/Cu

   Active metal casting (AMC®) was originally developed for limiters in the facility Tore Supra (France). It consists of casting of a pure Cu layer onto a laser-textured and Ti-metallised CFC surface. The laser-texturing helps keying of the Cu onto the CFC and the Ti coating aids wetting the CFC surface. The main advantages of the AMC® technology are its high re-melting temperature (1083 °C) and its excellent reliability [36].

The pure Cu layer is then joined onto the Cu alloy heat sink or coolant tube via an eutectic titanium brazing at 880°C or via low temperature HIP at 450-600°C. Low temperature HIP is performed for CFC plasma facing components with CuCrZr heat sink in order to recover the material properties of this alloy that were degraded by the high temperature of the HIP process [38]. Additionally, the joining at lower temperatures that is necessary needed for reactive metal brazes reduces residual fabrication stresses [38]. Basic metallurgical examinations and FEM simulations of the solid HIP process have been performed by Plansee AG to define a set of parameters for monoblock-HIP. Different interlayers in the CuCrZr tube–AMC Cu joint have been examined as well as different HIP parameters and HIP-can designs. The outcome of this R&D phase was the optimised selection of: the interlayer, the thickness of the steel capsule, the clearance between the CuCrZr tube and AMC, the applied HIP pressure, the clearance between the steel capsule and the CFC composite, the pressure - temperature history during cooling [39].

2.5. Neutron irradiation effect

Radiation effects in the plasma facing materials can be categorized as near surface damage caused by interaction with the plasma, and/or bulk displacements caused by neutrons emanating from the plasma or back scattered by the surrounding structure.

High energy particles, that travel through material, can interact with their surroundings. As the particles interact with material they lose energy in three ways: elastic collisions, electron excitations, and nuclear interactions. The interactions, which are of primary interest from the materials point of view, are the elastic collisions. If an ion or a neutron impacts sufficient energy to overcome an atom's binding energy (for example, E_d of carbon ≈20 eV), the atom is displaced from its original lattice position. If the energy transferred to the displaced atom (less its binding energy) is sufficient to displace further atoms, a series of displacement events or a "cascade" occurs. According the simplest interpretation of Kinchin-Pease for carbon, if a carbon atom were ejected by the plasma and reimpacted onto the carbon tile with a kinetic energy E of 1 KeV, the estimated number of atoms displaced (n) is estimated as follows:

$$N=(E/2*E_d)=25 \text{ atoms} \qquad (2 - 3)$$

The interaction of high energy neutrons with material is very similar to that of ions. The primary difference between the two being the amount of energy transferred in a single collision, and the distance over which the interactions take place. An ion, which has a relatively large radius and interacts coulombically, loses its energy over a short path length (typically less than a micron). In contrast, the comparatively small uncharged 14.1 MeV fusion neutron which undergoes only simple elastic collisions, has a mean free path of ~ 10 cm. So, on average, a fusion neutron will have an elastic collision with a carbon atom once in 10 cm of graphite. The amount of energy transferred to the carbon on this first collision (E_c) is calculated by simple elastic theory as:

$$Ec = \left[\frac{4m_c m_n}{(m_c + m_n)^2}\right] E_0 \cos^2\alpha = \left[\frac{4\times 6\times 1}{(6+1)^2}\right](14.1MeV)\cos^2\alpha \qquad (2 - 4)$$

Where m_c and m_n are the carbon and neutron mass, respectively, E_o is the neutron energy, and α is the angle between neutron path before and after the collision. For a totally back scattered neutron (the maximum imparted energy) the energy transferred to the displaced carbon is 4 MeV. From (2-3) and (2-4), the number of displaced carbon atoms resulting from this 4 MeV neutron displacement event is approximately 80 000 [40]. The vast majority of these atoms do not stay “displaced”, but diffuse back into the graphitic structure within a few picoseconds. To assess the effects such collision events have on a material, a convention has been adopted to compare irradiation doses. The displacement per atom, *dpa*, is the average number of times an atom has been knocked from its original lattice position. The dpa is an integrated average quantity and takes into account the density, the interaction cross section, and neutron energy spectrum. It has been estimated that the physics phase of ITER will accumulate approximately 1 dpa. In the DEMO, which more closely represents a power producing system, as much as 80 dpa is expected [40].

Irradiation impact on CFC materials

At the range <0.01 dpa there are essentially no mechanical property changes expected in graphite materials. However, even at these low doses thermal conductivity and stored energy are of concern. For displacement levels >0.01 dpa other property charges are significant: strength, elastic modulus, specific heat, Poisson’s ratio, and thermal conductivity. In addition, the dimensional stability under irradiation is important because the induced stresses may be significant, and because of the need for very tight dimensional tolerances at the plasma edge. It has been shown in fission neutron experiments that specific heat (C_p) and Poisson’s ratio are not greatly affected by irradiation. Moreover, only moderate changes in the CTE occur, but the magnitude and nature of the CTE change is highly dependent on the type of graphite [40].

Dimensional changes in CFCs dominated by the behaviour of fibres: neutron irradiation leads to shrinkage in the direction parallel to the fibres and to swelling in the perpendicular direction. Dimensional changes of 2- and 3D CFCs such as A05, CX 2002U, N112 in the temperature range ~350–840°C and damage dose of ~1 dpa are in the range of 0.5%. Increase of the irradiation temperature leads to an increase of the dimensional changes [41].

A marked increase in strength and elastic modulus occurs in graphite and CFCs at dose as low as 0.01 dpa. These increase continue to high displacement levels until volumetric expansion and extensive micro-cracking occur and the material begins to degrade. Structural degradation typically occurs at several to tens of dpa depending on the graphite type and irradiation temperature. The initial increase in modulus is a result of dislocation pinning by lattice defects produced by neutron irradiation. For most graphites a modulus increase of 2 to 2.5 times the unirradiated value is typical for irradiation temperatures less than 300°C, with the change becoming less pronounced at higher irradiation temperatures. Irradiation-induced increase in strength occurs in a similar fashion as the elastic modulus [40].

The irradiation-inducted thermal conductivity degradation of graphite and CFCs will cause serious problem in fusion system PFCs [41]. Thermal conductivity of irradiated CFCs may be partially restored by high temperature annealing. The level of the thermal conductivity recovery depends on the annealing temperature and neutron fluence. The full recovery of thermal conductivity of CFC irradiated up to 0.01 dpa was shown, while for CFC irradiated up to 0.84 dpa the recovery was not complete [41].

The performance of mock-ups using the different CFCs armour tiles has been studied including irradiation effects. Generally, the performance was as expected (higher temperature due to the loss of thermal conductivity). The decrease in the thermal conductivity due to neutron irradiation leads to an increase in thermal erosion under disruption conditions, and this may have to be taken into account during the erosion lifetime assessment [42].

Irradiation effects on Be

For ITER operational conditions, there is no significant influence on the physical properties of beryllium (including swelling). Generally, neutron irradiation causes an increase of tensile strength and a decrease of ductility and fracture toughness due to combined effects of neutron damage and helium generation. It is typical for all beryllium grades. It was proved that for expected ITER conditions (damage ~1–1.4 dpa, irradiation temperature ~200–400 °C) the behaviour of the recent Be grades is very similar, and the ductility will remain in the level of ~1% [42].

The changes of beryllium properties under neutron irradiation strongly depend on the irradiation temperature. At low irradiation temperature (~<300°C) the major changes are due to the displacement damage that leads to hardening and embrittlement of beryllium, while at high temperature (~>550°C) the helium production by gaseous transmutation results in a high level of gas driven swelling and grain boundary embrittlement [43].

Irradiation effects on W

Typically, neutron irradiation leads to an increase in the ductile-to-brittle transition temperature (DBTT) of tungsten alloys. Based on the available data, it could be concluded that all W grades have the problem of brittleness, at the expected fluence of 0.1–0.5 dpa in the region near the heat sink, for an irradiation temperature of less than ~500 °C [42]. Moreover, possible heating during transient events could lead to partial restoration of the ductility due to annealing of radiation defects. It is recommended to avoid the use of W in geometries with crack initiators. One possible way to solve this problem is to orientate W armoured design toward those concepts which reduce thermal stresses in the armour and in the joints (brush, rod or lamella structures) [41].

The maximum reported swelling during neutron irradiation was ~1.7% at 9.7 dpa and 800°C. However, a significant change of the microstructure is observed in tungsten, mainly the formation of a superlattice of voids. For instance, a superlattice of voids with diameter ~20 nm and lattice parameter ~120 nm was observed after irradiation at 550°C at neutron damage ~7 dpa. The presence of this type of defect is very important for the assessment of bulk tritium retention [44].

A maximum change of electrical resistance of 24% was measured in pure W after a maximum dose of $2x10^{22}$ n/cm^2 (~ 4 dpa). The main reason for this change is the accumulation of radiation defects and transmutation of the W to Re (after 0.5 dpa ~ 0.1% Re will be formed). Since in accordance with the Wiedemann-Franz law the electrical resistance of metals is inversely proportional to thermal conductivity, the latter should have changed accordingly. At the fluence expected in ITER, the thermal conductivity change will be negligible (~ 3%) [13].

Irradiation effects on copper alloys

Even low irradiation doses (~0.1-0.3 dpa) result in a significant change in the mechanical properties of Cu alloys. The irradiation results in an increase in strength of Cu alloys at low temperatures, approximately below 300 °C. Strength properties of unirradiated materials should be used for the design analysis as more conservative. At higher temperatures, approximately above 300 °C, the strength of irradiated materials is lower, and those values (strength of irradiated materials) should be used.

The ductility of CuCrZr-IG (IG – ITER Grade) alloy grows with increasing irradiation temperature. At irradiation temperatures <230 °C, uniform elongation is below 2%, and therefore, criteria for immediate plastic strain localisation and fracture should be used for the design analysis due to exhausting of ductility. At temperatures exceeding 230 °C, the material will be ductile (uniform elongation is above 2%), and high-temperature criteria should be used.

2.6. High heat flux performance of plasma facing components

During the last years the divertor and the first wall plasma facing components with different joining techniques were manufactured and tested under the high heat flux.

Figure 2 - 4 presents schematically some results of the high heat flux tests of the CFC/Cu actively cooled mock-ups. The figure shows clearly the tendency that the mock-ups with monoblock geometry sustain higher loads.

Last results reported by M. Merola et al. [45] show significant progress in manufacturing of PFCs.

In their experiments CFC monoblocks have been tested at 24-25 MW/m^2 up to 1000 cycles. The vertical target medium scale prototype endured 20MW/m^2 for 2000 cycles plus a number of critical heat flux tests in excess of 30 MW/m^2.

CFC flat tiles were tested up to 15-18 MW/m^2 for 1000 cycles without failure.

W monoblocks were tested up to 18-20 MW/m^2 for 1000 cycles (absorbed, that is more than 35 MW/m^2 incident heat flux) without failure.

W flat tiles were tested up to 16-18 MW/m^2 for 1000 cycles (absorbed) without failure.

Monoblock geometry generally proved to have a superior behaviour under high heat flux testing when compared with flat tile geometry. This is particularly appreciable with CFC armour. Furthermore, monoblock is not prone to cascade failure under heat flux loading with a glancing incidence and demonstrates to have an impressive high defect tolerance Taking this into account, the adoption of the CFC monoblock appears mandatory at least for the first set of the ITER divertor. On the other hand, flat tile geometry is cheaper and is recommended for those applications not exceeding 10-15 MW/m^2 [45].

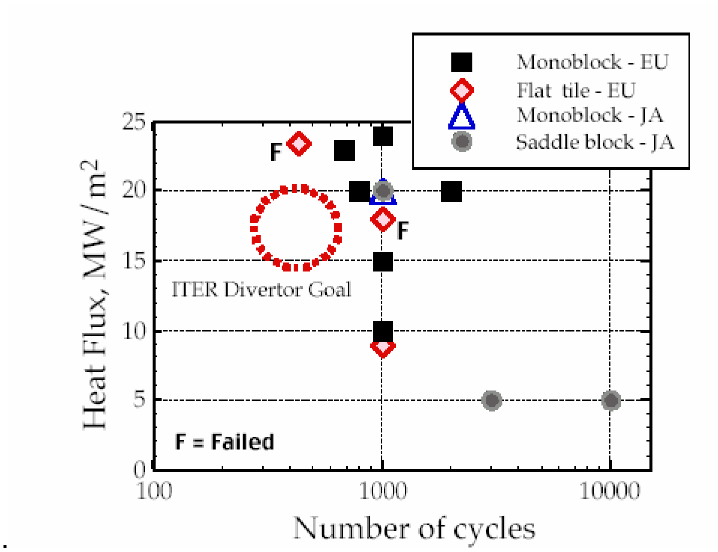

Figure 2 - 4. Results of high heat flux tests of the CFC/Cu actively cooled mock-ups [13]

Chapter 3. **Methods of investigation**

3.1. Non-destructive quality control methods

The quality control of plasma facing components (PFCs) is one of the key technological issues for the next generation fusion devices such as ITER. On the one hand, a fusion facility will be so complex that the costs to change the broken parts and as well as technological problems will be extremely high. On the other hand, only those methods can be used which allow a non-destructive examination, as the quality of a produced plasma facing components needs to be tested. Therefore, one methodological task to be solved is the adaptation of the existing non-destructive methods to assure quality and reliability of the joining techniques used in the divertor.

The modern technologies provide a wide spectrum of the non-destructive methods to the disposal of the scientists, these technologies for non-destructive testing are successfully applied in aerospace, nuclear and medical industries. An extensive R&D programme was carried out to investigate the suitability of the different methods to the current ITER divertor design [46]. The methods that can be applied for the quality control of the plasma facing components are: ultrasonic inspection, x-ray computer tomography and infrared thermography

In x-ray tomography, the structure of a three-dimensional body is reconstructed from a collection of projection images of the body. This method could be used in a whole range of industries, but it is not precise enough to reassure the quality of the bonding techniques of the divertor. Though this method is widely used for control of the brazings, this technique allows only to insure that the microholes are filled with brazing material [47]. The Japan Home Team has used X-ray methods. The method was able to detect a braze flaw of 2 mm diameter [46]. As the previous researches [47] have shown supplementary control by another non-destructive method, for example, infrared imaging, is required. Testing on the SATIR facility developed at CEA Cadarache [48] has proved that X-ray method does not give satisfactory results, some elements which had passed the X-ray control were rejected at the IR control.

The ultrasonic method is very useful in recognizing the joint defect via mapping the intensity of the reflection at the joint interface according to the coordinates of ultrasonic scanning [49]. This method was successfully applied and it proved to be adequate to inspect W/Cu and Cu/CuCrZr joints. Using an in-bore ultrasonic probe defects between AMC copper and Cu alloy tube with size 2 mm equivalent diameter are readily detected, and those of 1 mm can be detected with a high probability [46]. However, in the ultrasonic method, an ultrasonic wave is drastically damped in CFC armour because of its high porosity [49] that makes it difficult to apply this method for non-destructive analysis of CFC plasma facing components.

The important field where the infrared thermography can be used is to control the interface quality between tiles and heat sink. Several tests were performed by transient thermographic measurements on the SATIR test facility developed at CEA in 1994 [50] . Hereby surface tile temperature evolutions were compared to well brazed tiles temperature of a reference element, that was hydraulically connected in parallel [51]. Through the monitoring of 350 fingers dedicated to antenna limiters, 650 manufactured elements devoted to toroidal pump limiter and at least 200 toroidal pump limiter repaired elements, SATIR test bed has demonstrated its capability to inspect large amount of series elements [51]. Moreover, the method has been proven to be complementary to the X-ray radiography and ultrasonic inspections [47].

The infrared thermography proved to be a complementary and necessary non-destructive quality control method, which gives global information about the soundness of the heat path thus being a fast and economical way to assess the acceptability of a component [46]. Moreover, infrared thermography proved to be an important inspection technique able to predict well the component behaviour under high heat flux loading [52].

Due to the considerations above it was decided to use in this research the infrared thermography to analyse the heat removal in plasma facing components in order to control their manufacturing quality. For these investigations an IR facility, called IRINA (InfraRed Inspection for Non-destructive Analysis) was build up.

The electron beam facility JUDITH was used to study the peculiarities of the heat transfer and the thermal fatigue behavior of the PFCs under high heat flux loads. This facility is able to simulate high power heat loads similar to those imposed on the components in the plasma vessel in ITER.

Additionally, the numerical calculations by finite element using an ANSYS program were carried out to define the temperature fields and thermal stresses.

The detailed description of investigated components is presented in Table A3-1 (Appendix).

3.2. Infrared observation facility IRINA

3.2.1. Principal of infrared observation

Infrared thermography is a non-destructive inspection technique, that allows the assessment of surface temperature variations by means of a sensitive IR camera [53].

The principal of IR quality control is applied in fusion techniques, in particular, for the quality control of PFCs before being inserted into the plasma vessel of fusion devices. For example, CEA (France) uses the IR thermographic facility SATIR (Station d'Acquisition et de Traitement Infra Rouge) for non-destructive analysis of divertor and the first wall PFCs [54].

For the inspection, a plasma facing component is heated up by hot water flowing in the coolant tube from start temperature RT. This affects a non-linear increase of the surface temperature, recorded by the IR-camera. The inspection ends up with steady state. The temperature changing rate during heating and cooling reflects heat transfer properties of the component. For example, areas with small temperature changing rates indicate poorer heat transfer properties compared to areas with large temperature changing rates. Accordingly an area with small temperature changing rate can be related to a malfunctioning heat transfer, what is a strong indication of a major defect within the armour material or the joint interface [55].

3.2.2. Development and design of IR facility

IRINA (Figure 3 - 1) consists of hot and cold water loops combined with a temperature measuring system. The length of the mock-up can be up to 600 mm. It is mounted to the water loops by Swagelok connectors (the standard outer diameter of the coolant tube is 12 mm). The water loops are connected to a cold (room temperature) and hot (95°C) water supply. A magnetic valve handles the switch between hot and cold water. Hot water, the heat source in this infrared inspection, is provided by two reservoirs (2 x 80 liters), both equipped with a heater. From this supply, hot water flows under pressure (6 bar) through the mock-up. The inlet and outlet temperatures monitored by thermocouples. The inlet temperature is controlled to be 95°C. The flow rate is adjusted by a needle valve and measured by a turbine type flow meter. The water flow rate can reach up to 22 l/minute. Two lines of connectors enable the inspection of a testing mock-up with a reference mock-up. An IR camera (FLIR TV 900, Agema) is used to scan the surface temperature and the temperature

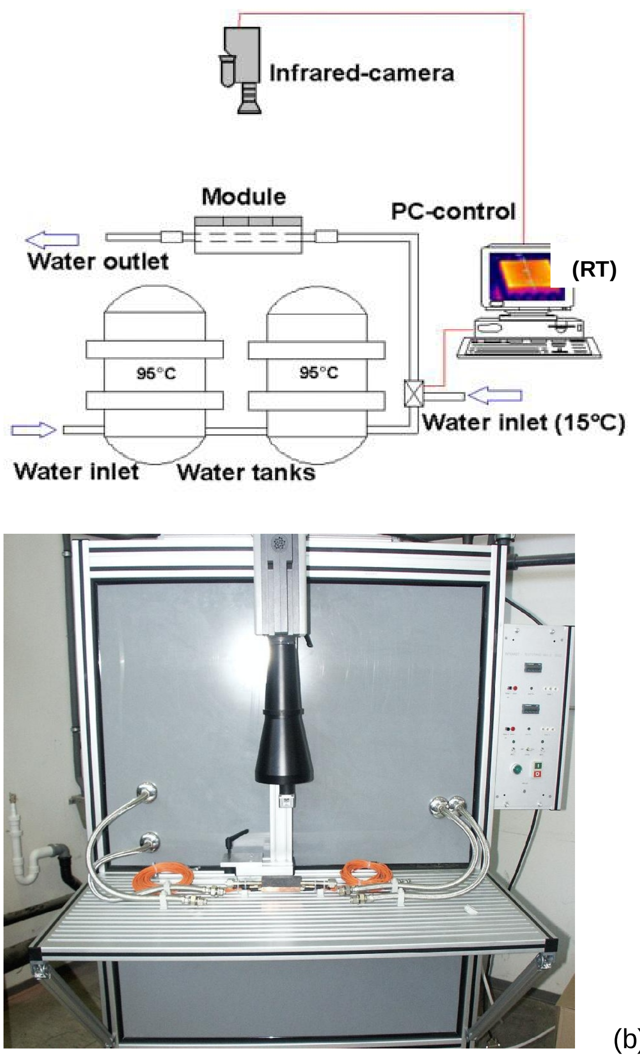

(a)

(b)

Figure 3 - 1. (a) The schema and (b) view of infrared facility IRINA

changing rate. The camera can be operated with two different lenses. One has a viewing angle 10° and an area 100x250 mm^2 can be observed from the distance of 1 m with spatial resolution of 1 mm^2. The second lens is a special design to investigate small material surface areas (20x20 mm^2) with high spatial resolution. The time resolution is 100 ms and the operation range is from -80°C to 2000°C. The temperature resolution of IR camera TV 900 is 0.1 K. Additionally, a digital IR camera (FLIR SC3000, Agema) with high spatial resolution and temperature resolution of 0.01 K can be used. The measurements are performed at ambient atmosphere. The module is surrounded by the special shield in order to eliminate the influence of the other IR sources (human bodies, sources of light etc.).

First, the mock-ups are cooled down by cold water to room temperature. The measurements by the IR camera are performed after switching to the hot water loop.

The experimental facility is used (1) to test newly produced PFCs in order to detect manufacturing defects and (2) to test modules after loading under electron beam in order to detect defects generated during high heat flux loads.

Essential elements of the construction were calculated before the facility was built. Special attention was paid to the problem of the heat transfer from the water to the module and also to the conditions of water flux inside the water pipe. For the sake of calculations the temperature of cold water was set to 10°C, and temperature of hot water was 95°C. The module was presumed to be 32 mm high, 25 mm width and 100 mm length and had cooling tube with a diameter of 10 mm.

Heat transfer

The heat flow transferred from water to a surface (wall) can be defined by formula [56]:

$$\dot{Q} = \alpha_K A(t_F - t_W)\text{ , [W]} \tag{3-1}$$

Taking into account the turbulent nature of water flow the following equations are applicable to describe the heat transfer conditions with turbulent coolant flow:

$$\mathrm{Re} = \frac{w d_R}{\nu}$$ Reynolds number (3-2)

$$B = \frac{1}{(5{,}15\lg(\mathrm{Re}) - 4{,}64)^2}$$ Compensation coefficient (3-3)

$$K_L = \left[1 + \left(\frac{d_R}{L}\right)^{0{,}667}\right]$$ Correction coefficient of length impact by turbulent pipe flow (3-4)

$$Nu = \frac{B(\mathrm{Re} - 1000)\,\mathrm{Pr}\,K_L}{1 + 12{,}7B^{0{,}5}(\mathrm{Pr}^{0{,}667} - 1)}$$ Nusselt number (3-5)

$$\alpha_K = \frac{Nu\lambda}{d_R}$$ Heat transfer coefficient (3-6)

The equations are reliable as long as 2320<Re<106; $d_R/L<1$; Pr, λ, ν by t_F

The most important parameter during the experiment in the facility IRINA is the time-period within which the T of the module rises from 10°C up to about 95°C (heating time-period). Prior to the construction of the facility IRINA this time-period was calculated with the help of FEM using program ANSYS. The equations (3-1)-(3-6) provided the necessary heat transfer parameters. The thermo-physical properties of a CFC material (thermal conductivity, heat capacity) were variables used for heating time-period calculation of this module.

Figure 3 - 2 presents the results of the calculations showing necessary time-period for raising the module temperature up to the temperature of hot water in relation to the water flow velocity.

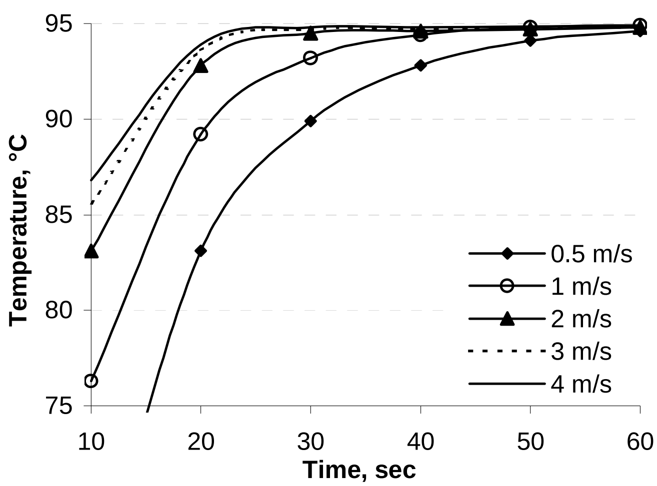

Figure 3 - 2. Time-period of PFCs heating in the IR facility IRINA according to FEM calculations

Figure 3 - 2 demonstrates that with increasing water flow velocity the heating time-period of a module is decreasing. For example, at a velocity of 0.5 m/s the heating time-period to achieve a temperature, that corresponds to a temperature rise of 93% of the temperature difference of two levels (about 93°C) is 41 s, and at 4 m/s this time decreases to 18 s. This is due to an increase of the heat transfer coefficient with increasing velocity. The same effect is applicable when a swirl is inserted into the cooling tube. This also increases the heat transfer between medium and PFC.

Table 3 - 1 gives the necessary amount of water for the heating of a module from 10°C up to 95°C for different water flow velocities.

Table 3 - 1. Necessary parameter of water pipe

Water flow velocity, m/s	0.5	1	2	3	4
Water flow rate, l/min	2.4	4.7	9.4	14.2	18.9
Heating time-period, s	41	29	21	19	18
Necessary water amount, l	1.6	24	3.1	4.5	5.7

According to FEM calculations, increasing water flow velocity from 2 to 4 m/s does not significantly affect the heating time-period. Moreover, the increase of water flow velocity leads to the rise of the water amount used. Two commercially available tanks (each of a size of 80 liter) were chosen in order to limit the water used to the reasonable amount.

Based on these results the parameters for the IR facility were chosen and the facility was built up. Figure 3-1b presents IRINA.

3.3. Electron beam facility JUDITH

One of the few available experimental set-ups for thermal fatigue investigation of PFCs in the world is the electron beam facility JUDITH (JUelich DIvertor Test facility in Hot cells). JUDITH has a beam power of up to 60 kW at an acceleration voltage of ≤150 kV (Figure 3 - 3).

The electron beam characteristics were measured by Y. Koza [57] and diameter is estimated to be approximately 1 mm at incident currents above 100 mA. A uniform heating on mock-ups is achieved by scanning the electron beam at high frequencies of typically 31 and 40 kHz. During the heat loading, the electron beam stays 1 mm away from all sample edges, and accordingly, the loaded area in the x- and y-directions are 2 mm smaller than the length and width of the mock-up surface [59]. Samples are mounted in a vacuum chamber with a dimension of 800 x 600 x 900 mm and actively cooled by water at room temperature with flow rate ϕ up to 60 l/min. The inlet and outlet temperature in coolant loop are measured with thermocouples.

Absorbed power density in a module will be determined as $P_{abs}=C_p(T_{outlet}-T_{inlet})\phi$ (C_p- specific heat of water). The vacuum chamber is equipped with a turbo molecular pump (2200 l/s). The technical data for the test facility are described in Table 3 - 3 [58]:

Table 3 - 3. Technical data of the electron beam facility JUDITH

total power:	≤ 60 kW
acceleration voltage:	≤150 kV
power density:	≤ 15 GW/m²
max. loaded area:	100 x 100 mm²
scanning frequency:	≤ 100 kHz
pulse duration:	1 ms...continuous
beam rise time:	130 µs (for short pulses <100 ms)
coolant loop: water, pressure, velocity, temperature	<40 bar, ≤ 1 l/s, RT

JUDITH is equipped with various diagnostics [58]:

- two infrared pyrometers, covering a temperature range between 200°C and 3000°C;
- a fast pyrometer from 1200°C to 3500°C (rise time < 10µs);

- infrared camera system (scanner) with cooled detector for temperature monitoring on module surfaces between room temperature and 3000°C;
- residual gas analyser (quadruple mass spectrometer);
- ionisation chamber to measure tritium release ;
- video camera system;
- thermocouples with data logger system;
- photodiodes and spectrometer (400-800 nm).

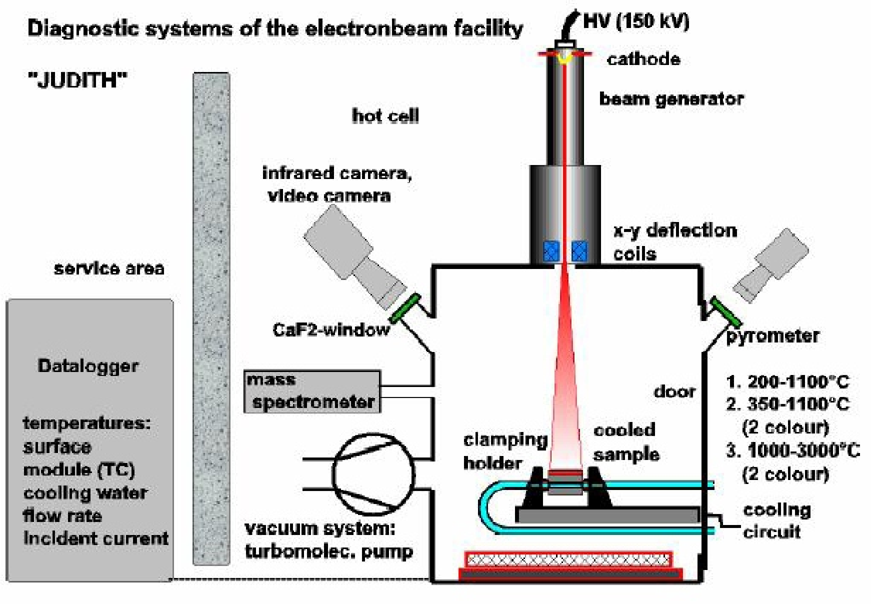

Figure 3 - 3. JUDITH electron beam facility with diagnostics [58]

Beside thermo-couples, that allow the exact temperature measurement at certain positions inside the modules, several diagnostics for surface temperature measurements are installed. A single colour infrared pyrometer and infrared camera measure the surface temperature (emissivity should set beforehand). In addition to these diagnostics, a two-colour pyrometer is used to measure surface temperature above 550°C [59].

In general two kinds of tests are performed in this facility [60]:

1. thermal shock tests to study the materials erosions behaviour during off-normal heat loads (e.g. simulation of plasma disruption or vertical displacement events)
2. tests with actively-cooled samples, in order to study the performances of PFCs under high heat flux, in particular, the performance of joints between armour and heat sink materials (steady state heating or thermal fatigue).

Different types of tests are performed in JUDITH. The combination of Screening Test (ScT) and Thermal Fatigue Test (TFT) forms the loading scheme to investigate the thermal behaviour of a module. In general, these tests are performed at power densities well below the design values of the components.

In screening test the surface is scanned by the electron beam until the armour surface temperature achieves steady state. In the next thermal cycle the surface is loaded at a higher power density. Increment of power density is typically 0.5…2 MW/m^2. The aim of ScT is to study the uniformity and stability of the heat transfer into a module by increasing beam power density.

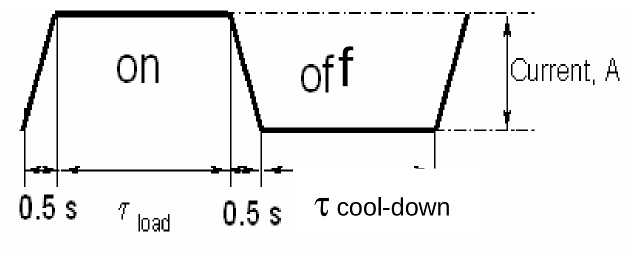

Figure 3 - 4. Profile of a thermal fatigue cycle

Thermal fatigue tests are carried out between screening tests at different power densities on actively cooled modules. During heating the surface is loaded by a high heat flux with a holding time τ_{load} at constant beam power density up to steady state. After switching off the beam the module cools down during the time τ_{load}. Then the cycle is repeated. Figure 3 - 4 shows a cycle scheme.

The thermal fatigue tests simulate the operating conditions in ITER divertor. In chapter 4 thermal fatigue tests of different plasma facing components tested in JUDITH are described.

3.4. Finite element method

The finite element method has become in last decades an indispensable tool for the analysis of stress and temperature distributions within a loaded component [61]. There are many practical engineering problems that require the analysis of problems involving the transfer of heat. Problems of this type can be investigated by a heat conduction analysis, taking in account latent effects and allowing variation in the thermal properties of the materials with temperature [62]. The application of finite element method for calculating the heat transfer problem is also of interest in the present work.

Theoretical fundaments of Finite Element Method to model heat conduction

The equation governing heat conduction in a continuous medium can be derived by imposing of conservation of heat energy over an arbitrary fixed volume, V, of the medium, that is bounded by a closed surface S [62].

If the medium is anisotropic, i.e. the conductivity depends on the direction; the form of the heat conduction equation is modified to

$c\frac{\partial T}{\partial t} = div(\boldsymbol{\lambda} gradT) + Q$, where

$$\boldsymbol{\lambda} = \begin{bmatrix} \lambda_{xx} & \lambda_{xy} & \lambda_{xz} \\ \lambda_{yx} & \lambda_{yy} & \lambda_{yz} \\ \lambda_{zx} & \lambda_{zy} & \lambda_{zz} \end{bmatrix}$$

is a conductivity tensor and, for example, λ_{xy} denotes the thermal conductivity in the x direction across a surface with normal in the y direction.

If the conductivity λ and the specific heat capacity ρc are assumed to be constant, and if the heat generation rate Q does not depend of T, the equation is linear and can be written as

$$\frac{1}{\alpha_1}\frac{\partial T}{\partial t} = \nabla^2 T + \frac{Q}{\lambda}$$

where $\chi = \lambda/\rho c$ is termed the thermal diffusivity of the medium and ∇^2 denotes the Laplacian operator defined, in Cartesian coordinates, by

$$\nabla^2 = \frac{\partial^2}{\partial x^2} + \frac{\partial^2}{\partial y^2} + \frac{\partial^2}{\partial z^2}$$

ANSYS

Several commercial finite element softwares are available. For thermal and structural calculation was applied a program ANSYS developed by ANSYS, Inc.

Many different types of problems may be analysed using the ANSYS code: structural, thermal, magnetic field, electric field, coupled field, and fluids analyses. ANSYS can couple the effects of different types of physical phenomena-indicating their combined impact on a design, thus creating more realistic simulations [63].

A typical ANSYS analysis has three distinct steps: build the model, apply loads and obtain the solution, review the results.

First, the element types, element real constants, material properties, and the model geometry, and than the analysis type and analysis options, apply loads, specify load step options, and initiate the finite element solution are defined using the PREP7 preprocessor.

Several methods of solving the simultaneous equations are available in the ANSYS program: frontal solution, sparse direct solution, Jacobi Conjugate Gradient (JCG) solution, Incomplete Cholesky Conjugate Gradient (ICCG) solution, Preconditioned Conjugate Gradient (PCG) solution, and an automatic iterative solver option. Selection of solver is depended on a given problem.

In postprocessing phase of an analysis the results can be reviewed. Two postprocessors are available: POST1, the general postprocessor, and POST26, the time-history processor. POST1 allows to review the results over the entire model at specific load steps and substeps. POST26 allows to review the variation of a particular result item at specific points in the model with respect to frequency, or with respect to some other result points. The ANSYS program enable to portray almost any aspect of a model in pictures or graphs on a file, or plot out as hard copy [63].

Chapter 4. Infrared inspection of plasma facing components

4.1. Preface

Development of high heat flux component is one of the most important tasks for fusion devices. Within this a main issue is the quality control of the high heat flux components, that is essential for a reliable operation of ITER. Standard methods of quality control (for example, ultrasonic inspections) are not able to detect the small defects in the components interfaces, responsible for early failure [64]. Therefore the development of alternative methods of non-destructive inspection and quality control for ITER components is an actual scientific and technical issue. The facility IRINA (Infrared Inspection by Nondestructive Analysis) was built up with the aim to check the integrity of components before and after they are tested in the electron beam facility JUDITH.

Further the possibility to use the IRINA working principle for studied manufacturing quality control should be elaborated.

The principle of infrared inspection consists in heat transfer phenomena through a layer of material with heterogeneous thermal-physical properties. The differences of heat transfer properties can be due to imperfection of materials (CFC armour) and due to defects in the joining of the plasma facing component.

A defect can be represented as a local variation of density in the material (pores, impurities) or as a mechanical defect in the joining area (cracks, imperfect joint). These modified zones in the structure of materials have different heat transfer properties in comparison with the surrounding. Possible defects can be classified in 3 main groups: (1) material surface defects, (2) defects of armour material, (3) defects in the joint between armour and cooling tube (monoblock concept) or between armour and heat sink (flat tile concept). The defects of types 1 and 3 are the most frequently observed in plasma facing components.

The aim of this chapter is to study the impact of different defect types on heat transfer in a module and the development of methods for the evaluation of heat transfer. Moreover, the objective of IRINA experiments is to determine the manufacturing quality of a module and to forecast its behavior during electron beam loading.

4.2. Components and experimental set-up

In order to investigate the possible capability of the infrared inspection method, a number of experiments were carried out in the facility IRINA. Peculiarities of heat transfer in PFCs with different design were carefully investigated. The following components have been thoroughly inspected for the features specific to heat transfer:

1. components with different geometries: a flat tile and a monoblock;

2. components with different armour material: CFC and beryllium armoured modules;
3. components with variable sizes (length and width);
4. components with different types of cooling tube (straight coolant channel, internal flow reversal).

This chapter discusses in details how to apply the infrared inspection method to investigation of heat transfer induced by water flow through the cooling tube of a plasma facing component. The development of the typical parameters for infrared inspection was done using the CFC monoblocks FT 113-1 and FT 113-2 described in Table A3-1 (Appendix). High thermal conductivity of CFC and high emissivity (about 0.8-0.95) [65, 66] allow infrared inspection during heating. The investigated CFC materials (as described in Chapter 2.4.1) have 3D structure and their thermal conductivities are different in direction x, y and z. Cu alloy used for heat sink is isotropic. The same modules were additionally tested in the electron beam facility JUDITH to observe their behavior under high heat flux loads. The results from the tests are described in section 4.7.

The dimensions of the modules were 28x19x160 mm^3 (FT 113-1) and 33x22x100 mm^3 (FT113-2) (width, height, length). The modules had a swirl tape in the cooling tube to increase the cooling efficiency.

The manufacturing of the CFC monoblock consisted of following steps:

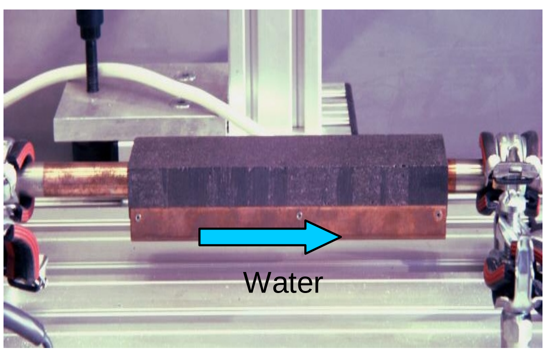

Figure 4 - 1. Experiment scheme

1. manufacturing of the CFC tiles to size;
2. drilling of the CFC tiles;
3. laser structuring of the CFC tiles at the inner wall of the holes;
4. AMC of CFC tiles with OFHC copper;
5. assembly of CFC monoblocks with CuCrZr tubes;
6. HIP (400°C/2h+550°C/6h/1000 bar);
7. final machining of CFC monoblocks.

During manufacturing the inspection procedures were carried out: dimension control, visual control, radiographic inspection of AMC, ultrasonic inspection of the HIP joint [67].

The experimental scheme is shown in Figure 4 - 1. A module is rigidly fixed in the cooling loop by Swagelok connectors. The surface temperature of the modules was observed with an IR camera. The water flow rate in cooling loop was 17 l/min or 4.0 m/s.

4.3. Impact of surface state

Figure 4 - 2 shows an infrared image of a module at steady state temperature. The diagram represents the temperature distribution along a line 1-1. The emissivity setting during IR measurement impacts strong the temperature interpretation. The average measured

temperature along this line was 93.2°C (red curve) (CFC emissivity of 0.95). The temperature deviation from this average temperature was up to ± 1 K. This can be explained by: the surface morphology, the cooling conditions.

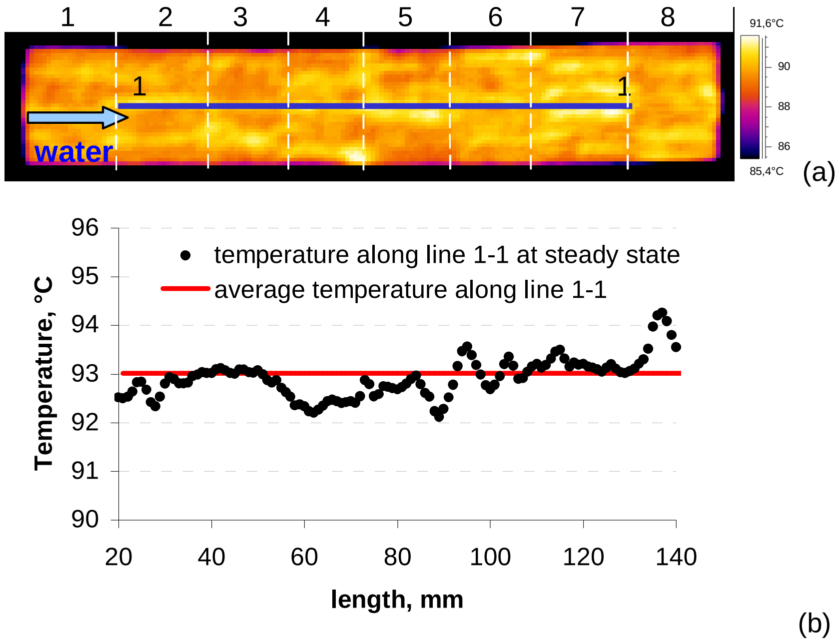

Figure 4 - 2. Module FT113-1: Steady state surface temperature during heating up with water of 95°C

The surface morphology includes structure and phase composition and surface roughness. In particular, the CFC material has a 3D structure with different types of fibers (PAN- and pitch) in three directions. The porosity of this CFC material is about 6-8%. In order to determine the influence of the surface roughness on infrared imaging a profilometric analysis of the module in a laser profilometer Polarus (Meier Messtechnik) was carried out. Due to the reflection of a 670 nm laser beam the vertical position of the surface was determined with a precision 0.1 µm [68].

In Figure 4 - 3a picture and an infrared image of the surface in steady state (temperature around 93°C) of the module FT 113-1 are presented. The infrared picture was made with a sensitive IR-Camera FLIR SC3000 with high spatial resolution and temperature resolution of 0.01 K (Figure 4 - 3). In the direct comparison of the two pictures, the similarities of the pattern became obvious.

It indicates that the measured temperature was higher in the visual darker areas (for example, the area A).). But in steady state the temperature of the whole surface must be the same. The fluctuation of surface temperature on the infrared image is caused by the variation of the emissivity on the CFC surface. This condition was not taken into account in the infrared imaging.

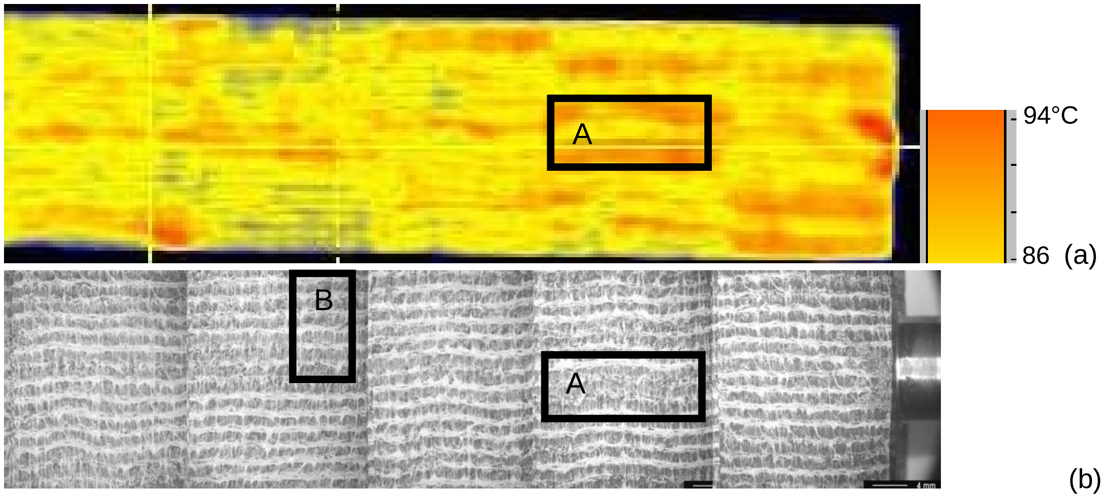

Figure 4 - 3. Module FT113-1. IR image and optical surface picture

Figure 4 - 4 shows the surface roughness in area B of the module FT 113-1. The light value of reflectivity and surface roughness were measured. The reflection curve (Figure 4 - 4b) corresponds to the position of bright zones in an optical image of the investigated area (Figure 4 - 4a). The roughness profile shows that the module has a well prepared surface, and several pits are also observed. Accordingly, the measured surface roughness did not have an apparent impact on the temperature distribution of the infrared image.

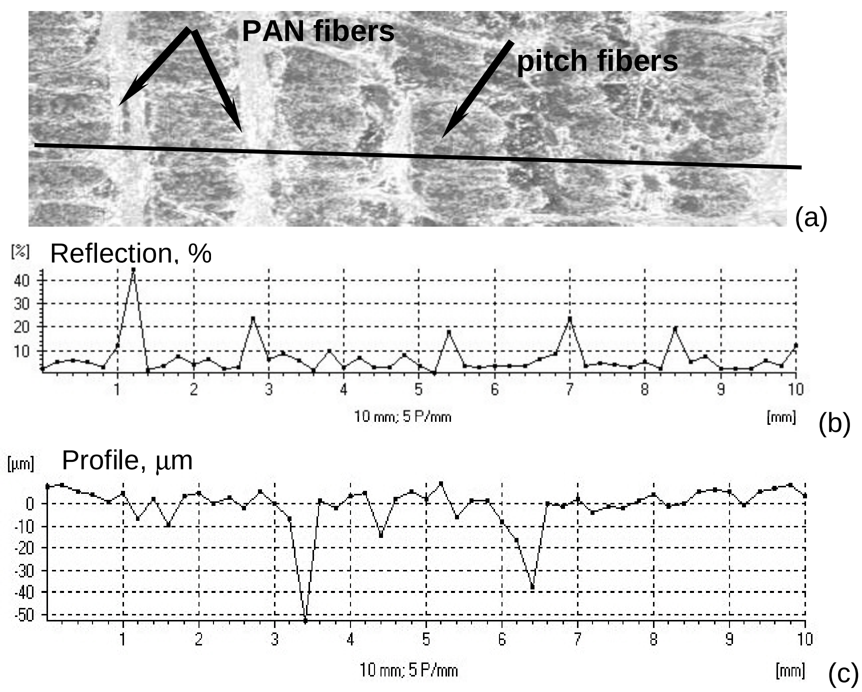

Figure 4 - 4. Module FT113-1. Reflection and profile of surface

Another reason for the surface temperature variation at steady state consists in different cooling conditions of the module. The module is not heat-insulated during the IRINA experiments. Therefore, the areas close to the edges are stronger cooled by convection compared to central areas (Figure 4 - 3a). The thermo-insulating shields should be used in order to eliminate this effect.

4.4. Correction of surface temperature

Next point of investigation concerned the transient observation of the temperature increase on the top surface of a module during heating up with hot water. Due to local fluctuation of emissivity, the reliability of surface temperature measurement at steady state (near to 95°C) is about 2 K.

To eliminate this effect, a method for surface temperature correction was developed. A correction coefficient was defined in assumption that the module surface has homogeneous temperature distribution at steady state. The interpretation of the temperature on an infrared image is made through emissivity, that is specified by the IR camera software for the whole observed area. In reality, the emissivity changes in dependence of the local surface character.

The correction of measured temperature was carried out for each pixel. First, the average temperature $T_{average}$ of a studied area was measurement at steady state. Then a correction coefficient matrix has been defined:

$$K_S = T_{average}/T \qquad (4\text{-}1)$$

where T is the locally resolved temperature in each pixel.

In the temperature working range (20°C<T<95°C) the emissivity coefficient changes insignificantly and can be assumed to be constant. At any moment of infrared observation, the temperature can be written as:

$$T_{corrected}=T_{observed}\times K_S$$

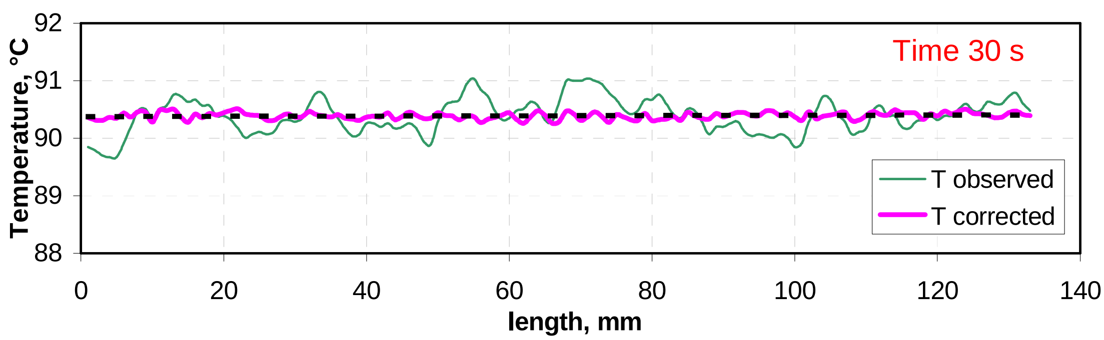

Figure 4 - 5. Module FT113-1. Steady state: observed and corrected temperature

Figure 4 - 5 presents the results after temperature correction at steady state of the module FT 113-1 (after 30 s heating) along the line 1-1 (s. Figure 4 - 2). By this correction the scatter of surface temperatures from average value at steady state is reduced from 2 K to 0.2 K.

In heating up and cooling down phases, different values of temperature occur not only due to different local emissivity, but also due to different heat transfer properties in those areas.

After the correction of the local emissivity, the local surface temperature corresponds to the local heat transfer properties.

Figure 4 - 6 shows the effect of the temperature correction during the heating up phase.

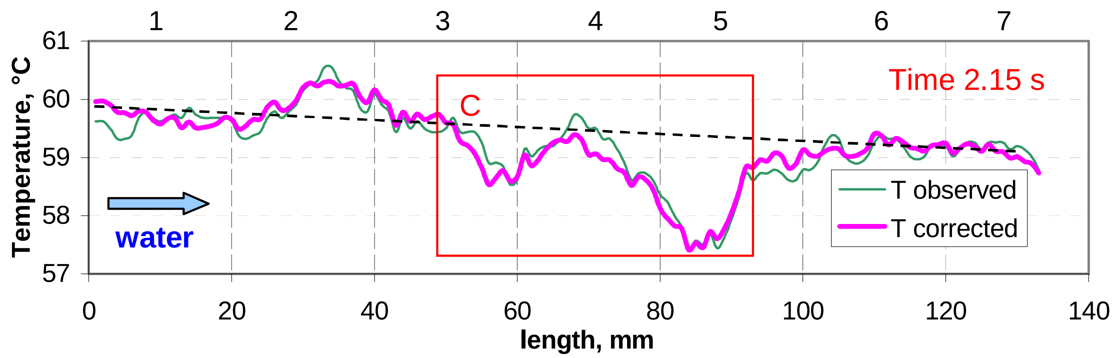

Figure 4 - 6. Module FT113-1. Heating phase: measured and corrected temperature

The corrected temperature (magenta curve) replicates the tendency of the original temperature measured with the infrared camera (green curve). After correction the temperature along the module does not equalize and there are areas where the temperature differs strongly from the temperature gradient curve (dotted line in Figure 4 - 6). This suggests that in these areas there are some imperfect structures with an impact on the heat transfer. The most probable structural imperfections in this case are errors in the joint layer between the armour and the cooling tube (small cracks or pores). In all following areas, that show lower temperatures than the surroundings are named “defects”.

The presence of this type of defects caused a reduction of heat transfer properties, and as consequence, the surface has a lower temperature level (e.g. area C in Figure 4 - 6). Moreover, Figure 4 - 6 demonstrates the contribution of the surface condition and the value of the surface temperature on the “defects”. The contribution of the surface state can be estimated from the difference between the measured temperature (green curve) and the corrected temperature (magenta curve). The maximum difference was 0.5 K. The contribution of defects can be seen as the temperature difference from the temperature gradient curve (dotted line). In area A, the maximal difference was about 2 K.

4.5. Temperature distributions

The procedure described above was applied for the surface temperature correction on module FT113-1. The area over the cooling tube was selected for a detailed investigation. The results of temperature correction at different time intervals during the heating up phase are shown in Figure 4 - 7. It shows clearly the defect area around the center, especially, after 2-3 s of the heating up phase. At this time the temperature difference ΔT between different areas along the cooling tube reached up to 6 K. During subsequent heating the surface temperature reaches the same level over the area. For example, after 7 s, ΔT did not exceed

3 K and after 10 s, when steady state was reached, ΔT became 0.2 K, and the cooling tube is no longer visible in the infrared image.

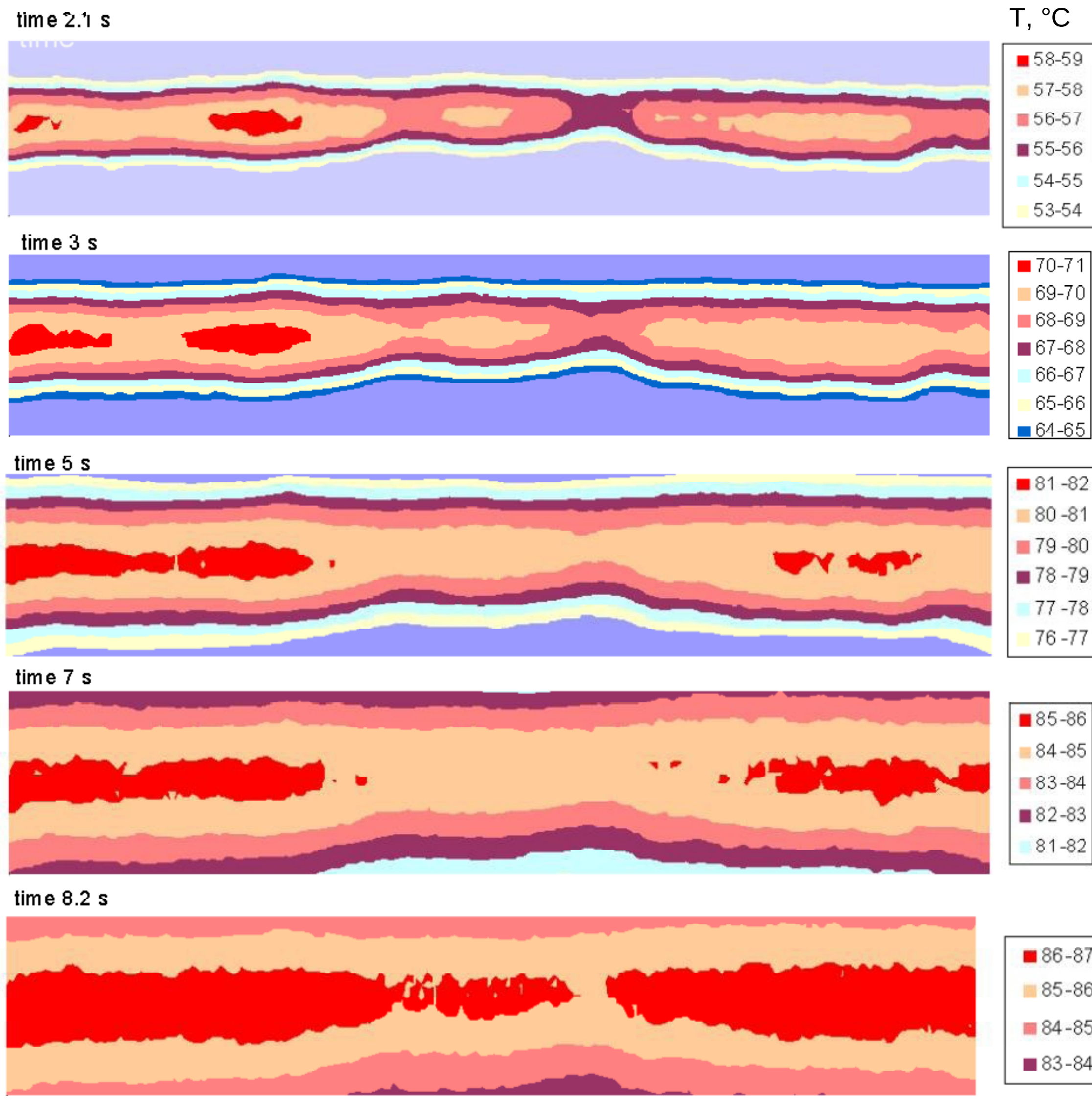

Figure 4 - 7. Corrected temperature on the top surface for the module FT113-1 during the heating in IRINA

3 s after switching from cold water to hot water the temperature difference ΔT between different areas became maximum. At this time moment the defect is observed most distinctively, therefore the method sensibility to detect the defect zone reaches its maximum (maximum detection sensibility - MDS). The infrared images of the top and the lateral surfaces of the module FT 113-1 and FT 113-2 after correction of surface emissivity are shown in Figure 4 - 8 and Figure 4 - 9, respectively. The original infrared images taken by the IR camera during the experiment are presented in Figure 1, Appendix 3.

A temperature gradient from center of the cooling tube to the edges is observed on the top surface of the module FT 113-1 and FT 113-2. The temperature gradient is explained by a cylindrical heat front perpendicular to the hot water flow direction.

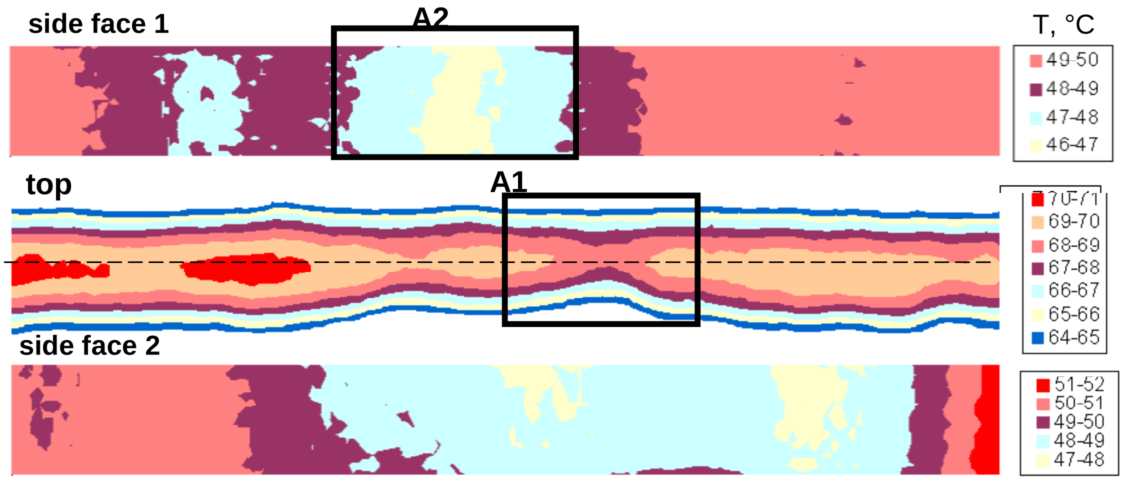

Figure 4 - 8. Temperature distribution of the module FT113-1 after 3 s of hot water heating

Moreover, an appreciable asymmetry of the cooling tube area on infrared image is observed. It indicates the existence of a structural defect on side face 1 in area A2 in the case of the module FT 113-1 (Figure 4 - 8). The infrared picture indicates this supposition (Figure A4 -1, Appendix). The defect area A2 is translocated to the left in comparison to the defect area A1 on the top surface. It indicates the existence of an additional defect on the lateral side face 1. The area with lower temperature on the side face 1 is small.

The temperature gradient on the lateral surfaces was observed along the cooling tube, but a temperature gradient from the cooling axis to the top surface was not clearly observed. This fact is explained by nonhomogeneous heat transfer properties of the armour material CFC. This aspect was studied in more detail by modelling of the module heating conditions using finite element (s. chapter 4.6).

Figure 4 - 9 shows the temperature fields on the surfaces of the module FT 113-2. A significant temperature drop was observed in the center on the top surface. It indicates the reduced heat transfer in this region. Furthermore a significant lower temperature was found on the left part of the side 2, although the hot water inlet was on the left side. This indicates a defect on the left side. Thus, the corrected temperature for eliminating of local emissivity fluctuations allows to determine the location of the pre-existing defect in the module.

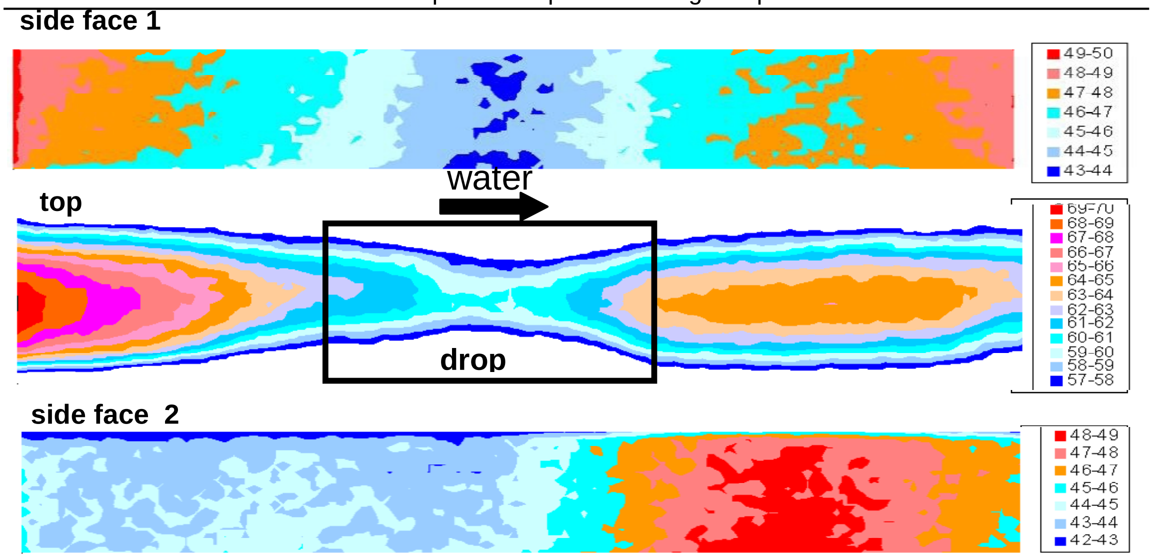

Figure 4 - 9. Temperature distribution of the module FT113-2 after 2.95 s of hot water heating

4.6. Numerical modeling

The 2D- and 3D-FEM calculations were carried out in order to study the impact of non uniform heat transfer properties of the armour material CFC during the heating phase in IRINA.

The following loading conditions were modelled: A module with the geometry similar to FT113-1 is heated in vacuum by hot water flowing through the cooling tube. Thermal conductivity of module materials depends on temperature. The heating time corresponds to the time till MDS of defects in the experiment and as a consequence set to 3.0 s.

Figure 4 - 10 shows the temperature distribution in the cross section of an ideal module calculated by FEM. The temperature front is not cylindrical due to different thermal conductivities in x- and y-directions. In y-direction thermal conductivity of CFC is about 2 times higher than in x-direction (thermal conductivity in x-direction is 0.105 W/mm K, in y-direction 0.227 W/mm K). The components in a tokamak are designed in such a way that the fibers in y-direction have highest thermal conductivity in order to remove a maximum of heat from the surface.

The curves in Figure 4 - 10 represent the temperature distribution on the top surface (a) and the lateral surface (b). The temperature intervals, in which the infrared images are shown in Figure A4-1 (Appendix), are outlined with red contour.

Figure 4 - 10 demonstrates that the temperature gradient from the center to the edges is about 15 K on top-surface, whereas the temperature gradient on lateral surface is only 1.5 K. It explains the different character of temperature fields distribution on top-surface and sides in Figure 4 - 9. The level of the calculated surface temperature after heating up during 3 s is higher than measured in the experiment.

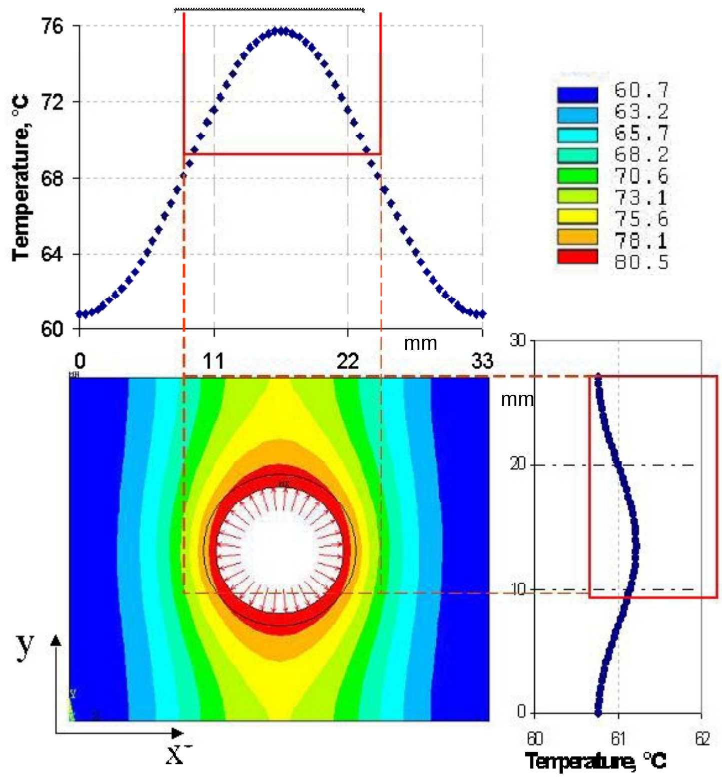

Figure 4 - 10. FEM calculation of temperature fields in module FT 113-1 during heating in IRINA

The fact that the calculated temperature is higher than experimental one can be explained with the used thermal conductivity data of an ideal CFC material. A real module has some imperfections such as internal defects in the joint layer between cooling tube and armour, or inhomogeneous CFC materials. The thermal conductivity of joining layer also was not taken into the account. Moreover, the real module is additionally cooled by convection from ambient air. These conditions were not included in the numerical model. All of these factors result in different levels of calculated and measured temperatures. Nevertheless the character of temperature distribution is identical.

Another study, that was realized using FEM analysis, is the investigation of the impact of defect areas on the heat transfer behavior in a CFC monoblock by the modelling of defective spots in the volume of a module. The modelling was applied for the module FT 113-2. For this purpose it was assumed that a defective spot can be specified as an area with reduced thermal conductivity [69] in the joint layer as shown in Figure 4 - 11. The defect locations were predicted by the results of the infrared inspections of heat transfer of the module FT 113-2 in IRINA. Defective spots were modelled in the following way: 2 defective spots were created in joint area around the cooling tube and their thermal conductivity was set at zero level.

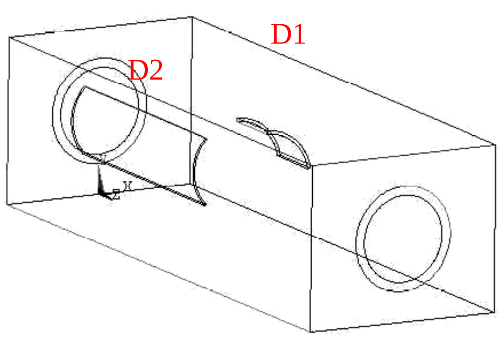

Figure 4 - 11. Location of defective spots in numerical model

Figure 4 - 12a demonstrates the experimental temperature distribution measured with the infrared camera. In Figure 4 - 12b calculated temperature fields are presented. Heating time

is 3 s. In the center of the module the temperature reduction is clearly observed in both pictures. In a numerical model a defect area D1 was assumed. A lateral defect area D2 causes the asymmetry in the temperature fields relative to length axis.

Thus, during modelling it was shown that due to defect areas in the joint layer the surface temperatures can be distributed as it was in experimental case.

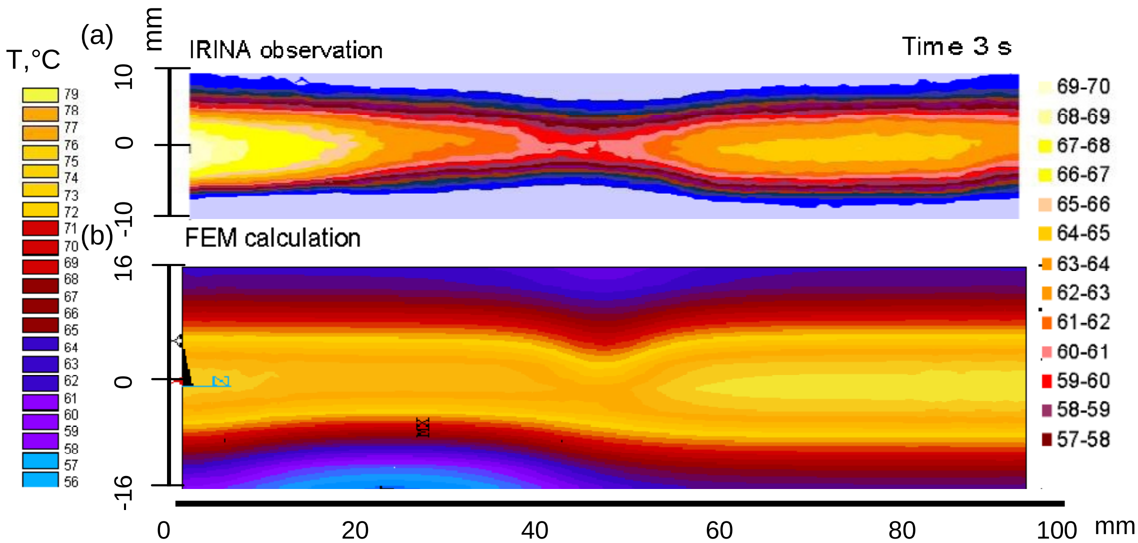

Figure 4 - 12. Temperature on the front surface of the module FT 113-1: (a) measured with IR camera, (b) calculated with finite element method assuming defective joints as indicated in Figure 4-11

4.7. Determination of defect zones

The important task of infrared inspections is to identify, to describe and to classify “defects” in the module’s structure. Moreover, it is necessary to define the optimum modelling parameters of “defects” measured during infrared observation, that will be described below.

Figure 4 - 13 presents the results of an analysis of relative temperature $T/T_{average}$ along a line 1- 1 in the area of expected defects. For each relative temperature curve heating time and average surface temperature are given. The infrared image shown in Figure 4 - 13 is taken at the moment of maximum detection sensibility (MDS) τ_d (the definition will be discussed in this section). The relative temperature decreases over the length of the module. At approximately 85 mm a strong drop of the relative temperature was observed. It can be seen that the amplitude of this drop in relative temperature decreases with increasing heating time. At more than 5 seconds the relative temperature deviation in this area is not significant anymore. The maximal deviation amounted about 5 % after 1.4 seconds of heating.

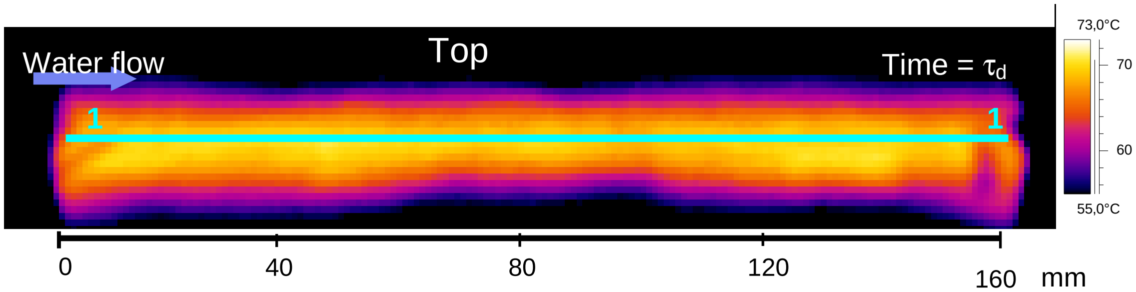

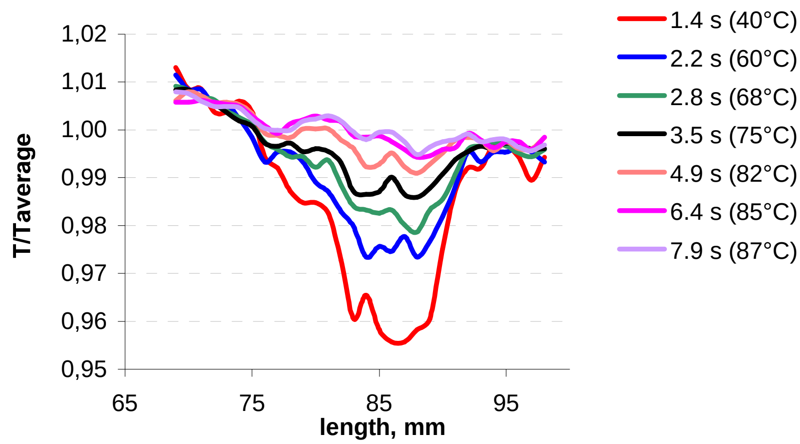

Figure 4 - 13. Evolution of surface temperature in the region of a supposed defect during heating of the module FT 113-1

A similar temperature distribution was also observed for the module FT 113-2 (Figure 4 - 14.). The evolution of the surface temperature fields in the region of internal structure defects had a similar character. Here the maximum relative temperature deviation from the average temperature reached up to 12% after 1.9 seconds of heating. This is twice as much as for the module FT 113-1. But it has to be considered that at this moment the deviation of surface temperature from average temperature in absolute value was not a maximum, since the level of surface temperature was low (40-50°C) and difference between the surface temperature and average temperature was not big.

In Figure 4 - 14. it is clearly shown that with time the temperature difference in the defect region becomes smaller and completely vanishes when it approaches steady state. It is in agreement with the character of surface temperature changes in a glued joint by presence of some known defects in [70].

Thus, the internal structure defects can be observed only during heating up or cooling down phase.

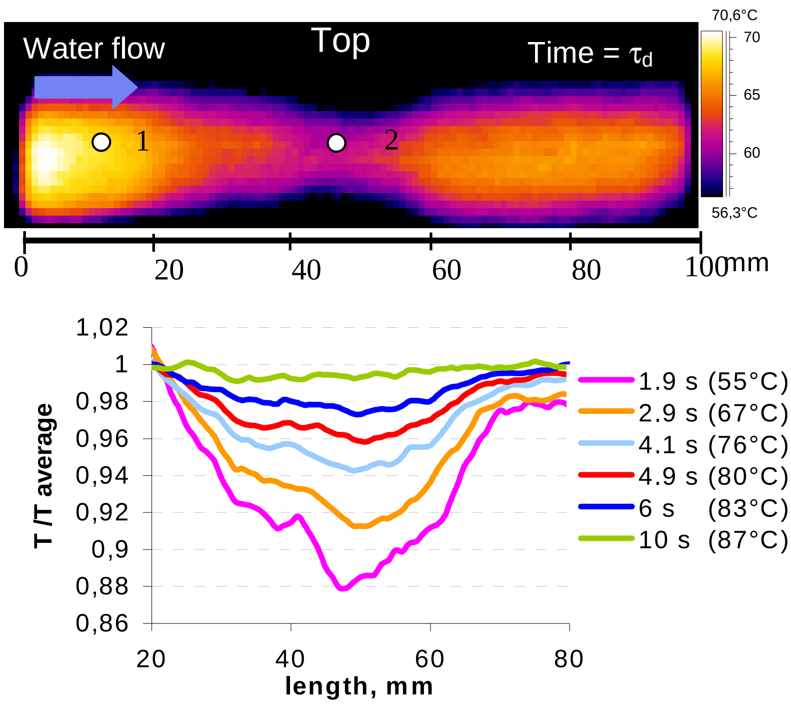

Figure 4 - 14. Evolution of surface temperature in region of a supposed defect during heating of the module FT 113-2

Figure 4 - 14.a shows the temperature fields in infrared spectrum during heating up of the module FT 113-2 after 2.9 seconds of heating. For the analysis two points on the surface 1 and 2 are chosen. Point 1 is located in a region with good heat transfer from the cooling tube to the surface. Point 2 is placed in an area with a relatively lower surface temperature in the infrared image.

Figure 4 - 15a demonstrates the temperature increase at these points during heating up of the module from 20 to 95°C. It can be clearly seen, that at any moment the temperature in point 2 (T_2) is lower than the temperature in point 1 (T_1). This means a reduced heat transfer in point 2 compared to point 1.

Figure 4 - 15b shows the temperature difference (T_1 - T_2) as a function of time. First the temperature difference increases sharply up to a maximum at the time τ_d and then decreases slowly down to zero, when steady state is reached.

From this picture three important aspects can be deduced: the moment of maximum detection sensibility (MDS) of defect areas τ_d, the optimal interval of defect zones observation during heating up $\Delta\tau_{observation}$, and the threshold of sensitivity of infrared inspection method ΔT_{min}.

The moment of MDS of defect areas τ_d was determined by comparing the surface temperature in points 1 and 2. The temperature difference (T_1 - T_2) reaches the maximum value during heating after τ_d =2.9 s. Time τ_d reached before the steady state conditions on the module. The surface temperature at the moment τ_d is about 65°C (2/3 of T_{max} =95°C). The maximum temperature difference in points 1 and 2 was ~7.5 K.

The dotted line in Figure 4 - 15b corresponds to a value of ΔT_{min}=2 K. This is a threshold value of temperature difference on the module surface. This parameter characterizes the sensitivity of the infrared inspection method for an investigation of the defect zones. The physical meaning of the parameter ΔT_{min} is the following: if the temperature in the studied area is lower than the average surface temperature ($T_{average}$) and their difference is more than ΔT_{min}, internal barriers are presented and it deteriorates the heat transfer. The most probable reason for heat transfer reduction is the different internal imperfections of structure. If the reduction in temperature is less than 2 K, the presence of structure defects in this area is questionable. The value of the sensitivity threshold for the infrared inspection method of the studied modules ΔT_{min} was estimated according to the proposal described by Durocher et al. [54]. Different factors have a strong influence on the IR measurement: the morphology of the surface, the homogeneity of thermal material properties, the atmosphere, the coolant conditions, the sensibility of the IR camera. The impact of all of these factors on the measured temperature was estimated to be ~2 K (0.1 K due to the IR camera sensitivity, 0.2-0.3 K due to the impact of surface morphology on temperature measurement, temperature fluctuations of about 0.2 K occur due to environment conditions, 0.8 K is the impact of thermo-physical properties variation of CFC, and 0.6 K is the influence of heat transfer properties of the module on the surface temperature).

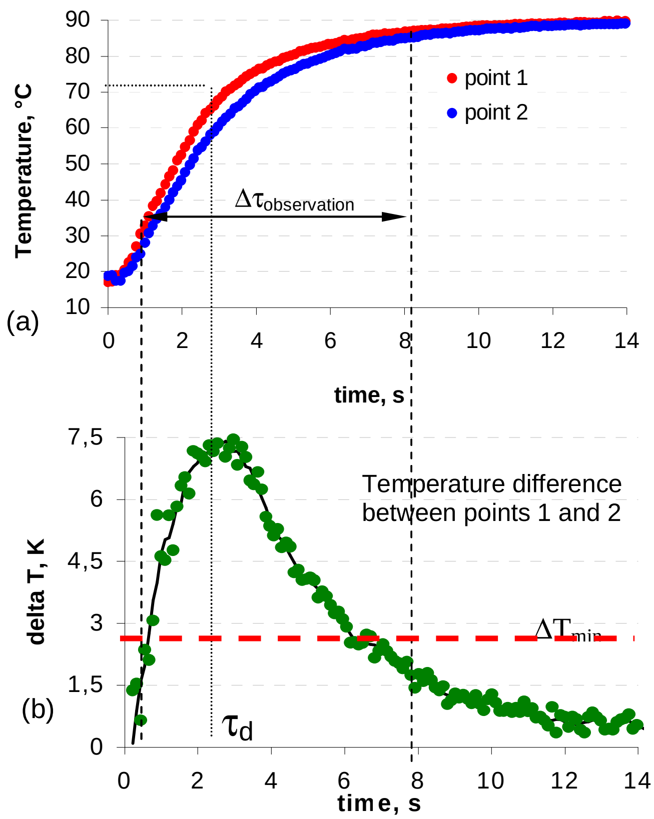

Figure 4 - 15. Temperature behavior in points 1 and 2 during heating up

Moreover, Figure 4 - 15b allows define other important parameter of the experiment - the optimal interval of the defect zones observation during heating up $\Delta\tau_{observation}$. It is an interval, in which the curve of the temperature difference (T_1 - T_2) is higher than the threshold of sensitivity of infrared inspection method ΔT_{min}. Thus, in this time interval the deviation of the local surface temperature from the average surface temperature indicates the presence of faults in the structure and its impact on the heat transfer behavior of a module.

4.8. Experimental modeling of a defect in the joint interlayer

The results of experimental and numerical investigations of heat transfer properties of the modules FT 113-1 and FT 113-2 showed, that the presence of areas with reduced heat transfer properties (defect areas) in a module has a strong impact on the module behavior during heating up. The high heat loading was supposed to be performed after the experiments on the IRINA facility. Therefore, type and geometrical size of the discovered defect zones in the investigated modules cannot be determined by metallographic analysis. Therefore it is necessary, to study the impact of defects with a predetermined geometry in the joint interlayer on the surface temperature distribution during the heating up phase.

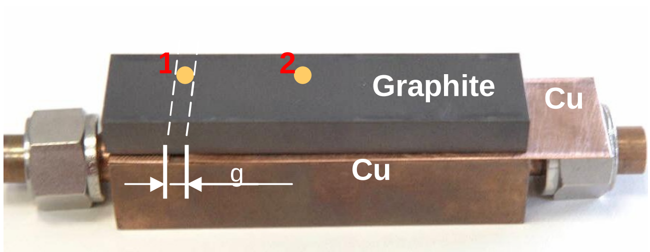

Figure 4 - 16. A model module with predetermined defects: size 30x30x100 mm, armour 10 mm.

For this purpose several modeling experiments have been done. A scheme of a model module is shown in Figure 4 - 16. As a material for heat sink, pure copper was chosen. A joint interlayer was modeled with a copper foil (thickness 0.5 mm). As armour a plate from isotropic graphite (grade R6650) was taken. A transverse defect (a gap) with a width g was adjusted between 0 and 15 mm by pulling out the Cu-interlayer. The module was kept together by special clamping system made of heat-insulating material.

The surface temperature response as a function of gap size was investigated in the facility IRINA.

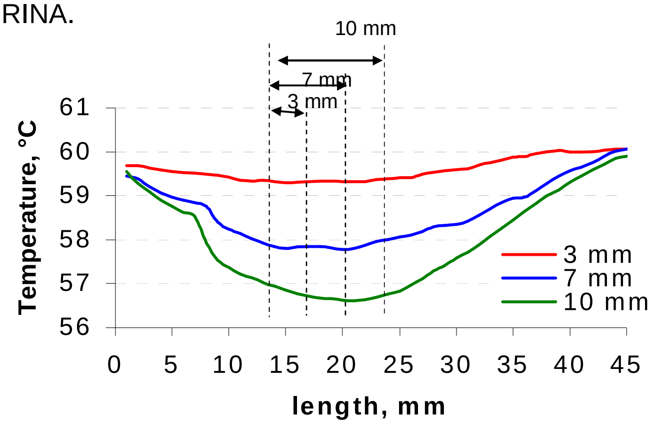

Figure 4 - 17. Surface temperature over a defect area at the moment of MDS τ_d

In a Figure 4 - 17. the temperature curves of the module surface for three different defect sizes for the moment of MDS τ_d=3 s are presented (see Chapter 4.7).

At a small gap size (3 mm) the temperature deviation in the gap area from the average temperature is not significant, namely less than 1 K. With increasing the gap size the temperature reduction is increased. Additional studies showed that the position of temperature minimum corresponds to the center of the gap. The temperature difference $\Delta T=T_1-T_2$ between points 1 and 2 was verified. Point 1 was taken at the center of the gap. The position of point 2 is located at the geometrical center of the module surface.

Figure 4 - 18 presents a dependence of this difference, ΔT on the gap size. The dependence has a linear character.

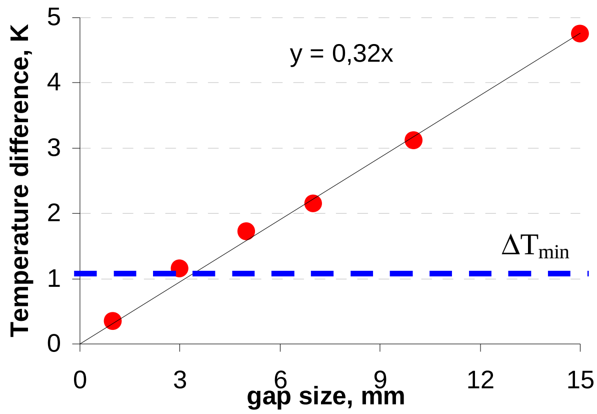

Figure 4 - 18. Dependence of surface temperature difference ΔT from gap size

Thus, if the relation between ΔT and gap size is known, it is possible to forecast the dimensions and location of the defect zone in a real plasma facing component. However, it becomes necessary to define in a first step the experimental dependence of ΔT versus gap size. For plasma facing components this has to be done by infrared and metallographic analysis of a defect module. In a second step, other modules of the same kind can be observed by infrared inspection in the IRINA facility to analyze the temperature fields during heating up phase.

For this propose a series of new model experiments are needed to develop a quality control method of heat transfer properties of plasma facing components. It is essential to investigate the impact of the gaps with different geometrical configuration and with different locations in a module on the change of the heat transfer properties. In addition, there is also a need to investigate the influence of different joining and armour materials on the heat transfer behavior of a module during the presence of defects for experience in quality inspection of different types of PFCs.

For this experiment the sensitivity threshold of the infrared inspection method ΔT_{min} was estimated to be 1 K (0.1 K due to the IR camera sensitivity, 0.2-0.3 K due to the impact of surface morphology on temperature measurement, temperature fluctuations of about 0.2 K occur due to environment conditions, and 0.4 K is the influence of heat transfer properties of the model module on the surface temperature) (Figure 4 - 18). This estimation of method sensitivity and dependence of temperature difference due to the gap size is available only for this configuration. Also this criteria has to be defined for each configuration of modules.

4.9. Comparison with electron beam inspection method in JUDITH

From the IRINA-experiments it was concluded that the modules FT 113-1 and FT 113-2 should have defect areas. To confirm this suspicion tests in the electron beam facility JUDITH under steady state heating conditions were carried out.

The modules were loaded in screening regime at absorbed power densities of 1 -7.5 MW/m^2.

In Figure 4 - 19a and Figure 4 - 20a the infrared images of temperature distribution at steady state on the surface of the modules FT 113-2 and FT 113-1, respectively, are presented.

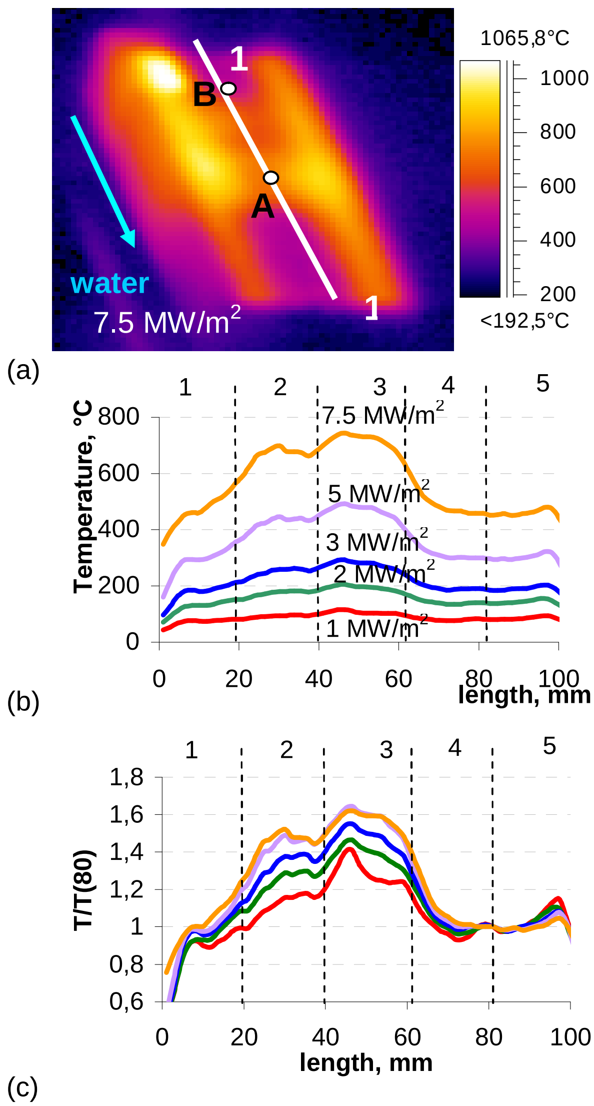

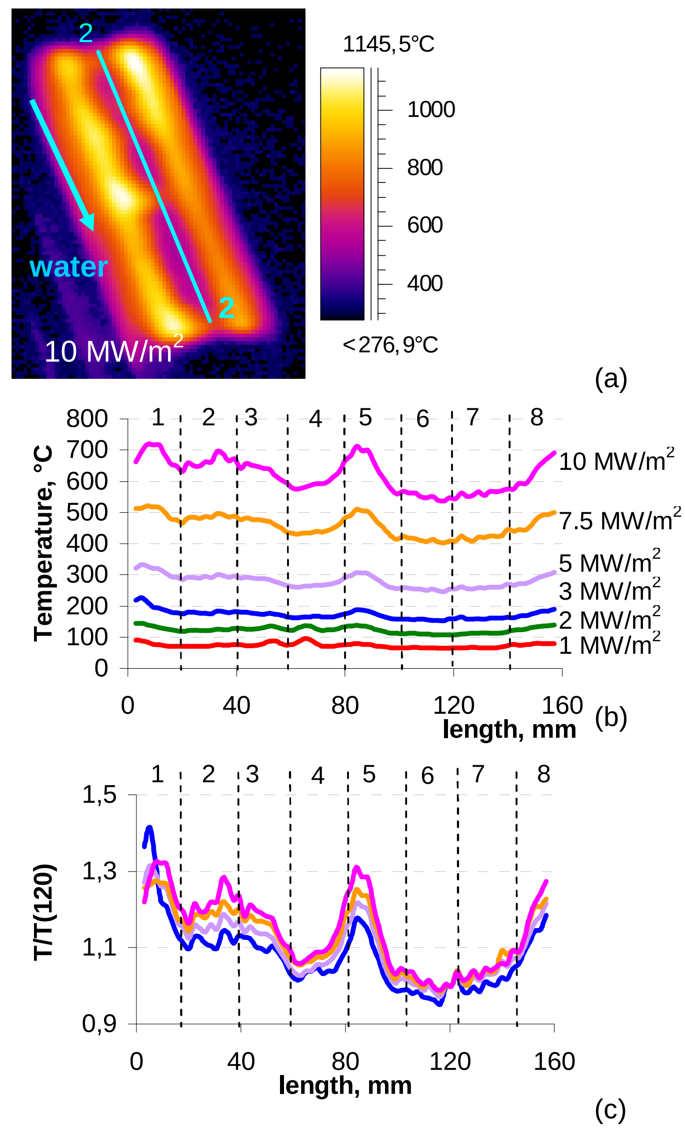

Figure 4 - 19. Module FT 113-2:
(a) surface temperature distribution at steady state in JUDITH at 7.5 MW/m^2;
(b) temperature distributions for different power densities along the line 1-1;
(c) relative temperature T/T(80)

Figure 4 - 20. Module FT 113-1:
(a) surface temperature distribution at steady state in JUDITH at 10 MW/m^2;
(b) temperature distributions for different power densities along the line 2-2;
(c) relative temperature T/T(120)

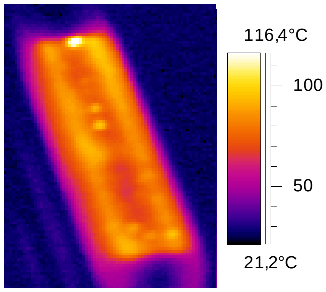

Figure 4 - 21. Hot spots on the surface of the module FT 113-1 at 1 MW/m^2

In both infrared images several characteristic areas can be picked out. The location of the cooling tubes can be clearly seen on the surface due to the lower surface temperature along the cooling tube. Temperatures on the edges of the modules are the highest, as a result of different cooling condition in the cross section of the modules. This effect is studied in detail below by using finite element. Overheated zones along the cooling tube are observed in the central area of both modules. Their presence can be explained only by a reduction of heat transfer rate from the surface.

Figure 4 - 19b shows the temperature distribution curves along the line 1-1 (Figure 4 - 19a) at absorbed power densities of 1-7.5 MW/m^2. Dotted lines show the borders of the single CFC blocks of the module. At each heat flux level the temperatures on tiles 4 and 5 are at the same level. On tiles 2 and 3 the temperature is higher than on the other tiles. Tiles 2 and 3 are located in the central part of the module.

In Figure 4 - 19c, a diagram of the relative temperature T/T(80) clearly demonstrates the increase of the temperature in the central tiles. T(80) is the temperature at a reference point selected in the position of 80 mm along the line 1-1. The area around this point does not show any temperature level changes at each power density. In Figure 4 - 19c the colours of the relative temperature curves correspond to the colours of temperature curves in Figure 4 - 19b. Figure 4 - 19c shows that in the form of relative temperature T/T(80) the surface temperature distributions look similar, and the curves of relative temperature lie close together for all heat fluxes. This means, that in the central part of the module the heat is transferred from the surface to the cooling tube with a reduced rate probably due to a defect area on the interface leading the cooling tube in the module.

However, it is necessary to note that the stable temperature field distribution in relative coordinates, that does not depend on the level of steady surface temperature, is observed at an absorbed power density of 5 MW/m^2 (curves T/T(80) at 5 MW/m^2 and 7.5 MW/m^2 coincide). At low power densities and, consequently, low surface temperatures the error of temperature measurement by means of the IR camera increases. The measuring error appears in particular due to inhomogeneous emissivity value on the CFC armour surface. The emissivity and surface temperature corrections measured in this experiment by IR camera were not performed. Small difference of temperature field distribution in relative coordinates can be explained also by the phenomena of temperature dependent thermal conductivity of CFC. This conductivity significantly decreases (in factor about 2) with temperature increasing from RT to 400°C and decreases slowly at high temperatures (see Chapter 5.3).

Figure 4 - 20 illustrates the analogical analysis for the module FT 113-1. Small areas with low overheating are characteristic for this module. The minimum temperature at each load was observed during the experiment on the surface of tiles 6 and 7. T(120) selected as reference temperature. An insignificant overheating (about 15-20% in diagram of relative temperature T/T(120), Figure 4 - 20c) is observed on tiles 2 and 3 at all power densities. The highest values were found on tile 5, its overheating is up to 30% in comparison to tiles 6 and 7 (Figure 4 - 20c).

The interesting peculiarity in surface behavior during heating up is the presence of temperature jumps on tiles 3 and 4 at low power densities of 1-2 MW/m^2 and temperature jump on the tile 1 at 3 MW/m^2. With increasing of the load this local surface overheating disappears (Figure 4 - 20b). Evidently, in this place the surface emissivity strongly differs from the average surface emissivity of the CFC material. This fact influences on the temperature interpretation measured by an IR camera at low surface temperatures. This suspection becomes clear in Figure 4 - 21. On tiles 3 and 4 the local spots with different emissivity (pores, potholes) are placed. Present distinguish of CFC surface behavior indicates, that primary selection of modules according to their heat transfer homogeneity has to be carried out at medium loads (from 5 MW/m^2), when the impact of surface state on temperature interpretation is much less than impact of structure imperfections. Moreover, local temperature jump on an infrared picture can be also caused by dust on the surface, that is removed after several beam pulses.

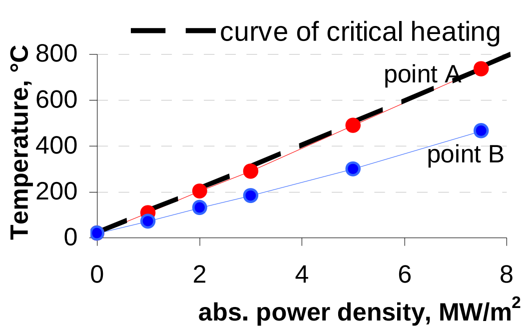

Figure 4 - 22. Temperature increase on the surface of the module FT 113-2 during steady state heating in JUDITH

The dependence of the surface temperature on the absorbed power density for the surface points A and B of the module FT 113-2 is demonstrated in Figure 4 - 22 (the position of points A and B is shown in Figure 4 - 20a). Point A is situated in the central area of the module where overheating occurred (on the tile 5). Point B lies in relative cold area on the tile 1. The rise of the temperature in point A happens faster than in point B. It indicates inhomogeneous heat transfer from surface to the cooling tube in this area.

Thus, Figure 4 - 22 illustrates that in the studied heat load range (P_{abs}=1-7.5 MW/m^2) the dependence of surface temperature $T(P_{abs})$ has a linear character. Moreover, a special study carried out using FEM showed that by expansion of heat loads range up to 20 MW/m^2 this dependence deviates from linear (Figure 4 - 23). Calculated surface temperatures was fitted with a polynomial $y = -0.075x^3 + 3.12x^2 + 49.2x + 27.9$. At low power densities (up to 10 MW/m^2) the temperature can be also fitted good with a linear function $y=70.3x+20$ (dotted line in Figure 4 - 23). In the range of high loads (10-25 MW/m^2) the deviation of calculated temperature T(P) from linear does not exceed 15%.

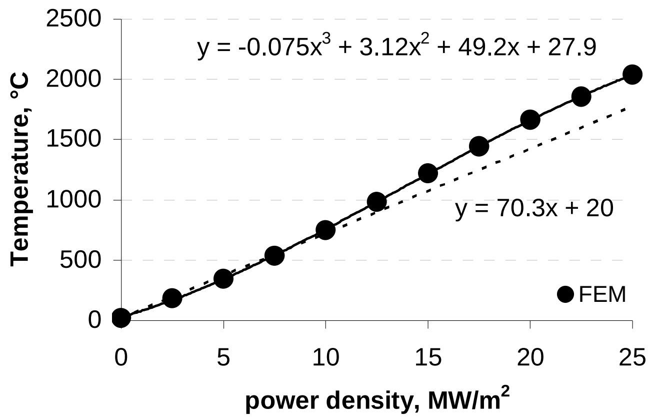

Figure 4 - 23. FEM calculation of surface temperature during heating of a CFC monoblock module

Therefore, one may plot a curve of critical heating. In [71] it is pointed out that the surface temperature of CFC plasma facing components during operation at power density of 20 MW/m^2 mostly does not exceed 2000°C (due to sublimation of CFC and high thermal stresses in module's construction). Without heat load the module surface has room temperature. The curve of critical heating is build by simple linear extrapolation of these two parameters (Figure 4 - 22).

Thus, if an experimental curve of surface temperature $T(P_{abs})$ is lower than the critical heating curve, a reliable thermal fatigue behavior of a module can be expected with high probability. If there is a convergence of the experimental curve and the curve of critical heating than the predictions about maximum permitted high temperature can be made for high loads. It may be caused by (1) module design (edge areas normally have higher temperature); (2) module sizes; and (3) heat transfer degradation due to presence of some internal imperfections.

As it is presented in Figure 4 - 22, the temperature in the point B of the module FT 113-2 is situated well below the curve of critical heating and therefore the point B can be evidently described as reliable. In the point A the heating curve is close to the critical heating curve, however, point A is located in area with similar heating-cooling conditions as the point B. Hence, the behavior of an area around the point A attracts attention. According to Figure 4 - 19 exactly here the internal defects in the joint layer are located, which reduce heat transfer from surface to cooling tube and cause the overheating.

FEM calculations have been performed to explain the high temperature areas on the edges of the modules. The results and the comparison with experimental data are given in Figure 4 - 24. Figure 4 - 24a shows temperature fields in the cross section of the module at a power density of 7.5 MW/m^2. In Figure 4 - 24b an infrared image of the module surface at the same load is presented. At a line 2-2 the results of calculation and experimental temperature are compared (Figure 4 - 24c). Evidently, the calculated and experimental temperature curves are in good agreement. The light temperature drop on the edges might be due to a surface radiation effect, which was not included in the numerical model.

Figure 4 - 24 clearly shows, that the surface temperature distribution for a module with given geometry under electron beam heating is not uniformly. There is a significant temperature gradient from the center to the edges and in the example of Figure 4 - 24 the temperature differences are above 300°C. The module has too wide for a module typically designed for divertor.

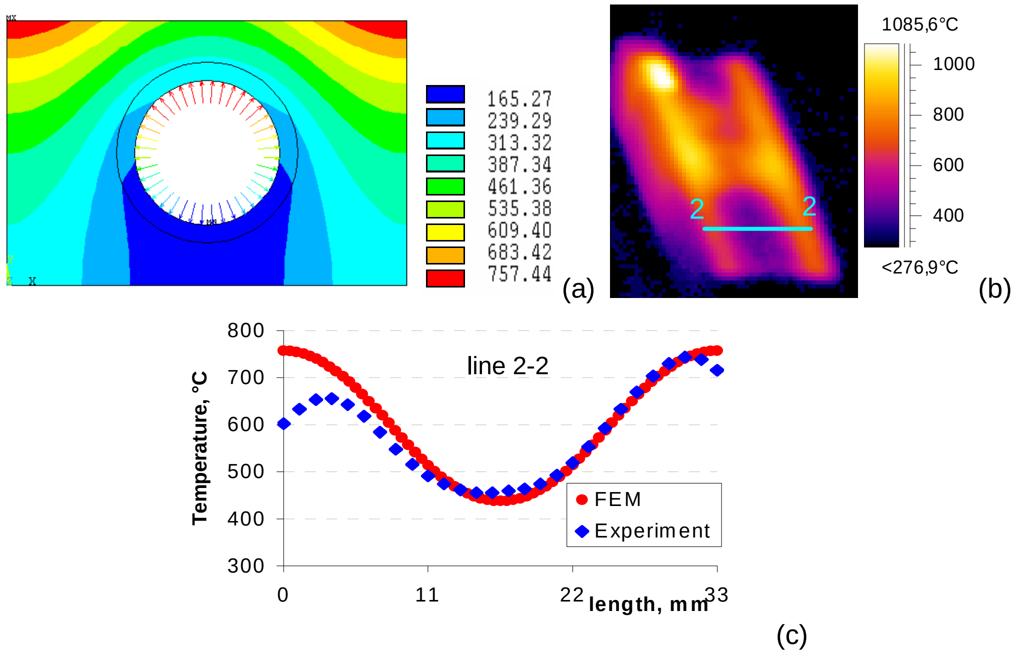

Figure 4 - 24. Calculated and experimental temperature distributions across the module FT 113-2 heated at 7.5 MW/m^2

Both methods – infrared inspection during heating up of a module from inside using hot water and electron beam heating by step-by-step increasing the beam power density – are investigation methods to study the uniformity of heat transfer in a module with the aim to guaranty the manufacturing quality.

The distinction between the two experimental methods is the different directions of heat flow gradient: in IRINA the heat is transported from the cooling tube to the module surface, in JUDITH the heat is conducted from the surface to the cooling tube. Moreover, IRINA operation is easier and cheaper compared to JUDITH. The integration of IRINA in fusion activities is therefore an actual practical and scientific task.

The comparison of the experimental results of module quality investigation obtained by these two methods is discussed below.

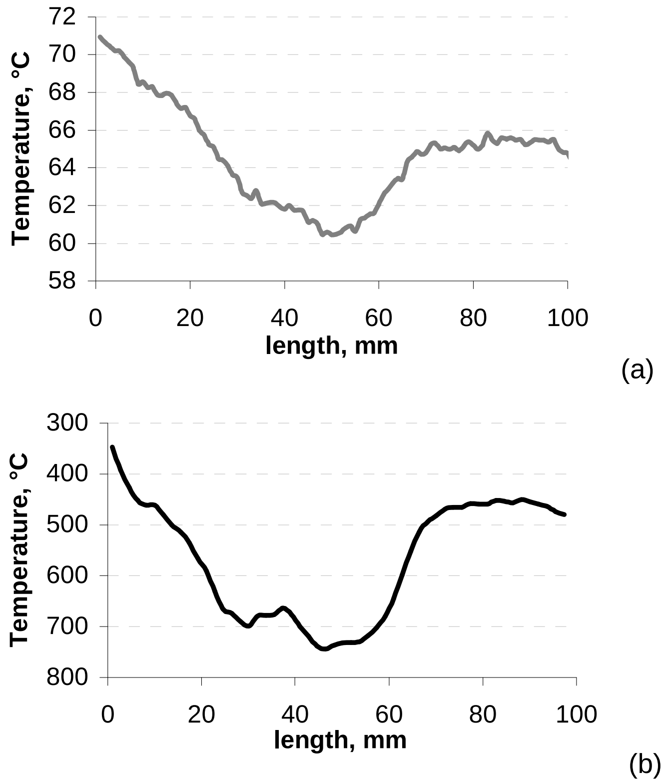

Figure 4 - 25. Surface temperature distribution during (a) IRINA and (b) JUDITH testing of the module FT 113-2 (temperature scale is in reversed order)

Figure 4 - 25 shows the surface temperature curves for module FT 113-2 in IRINA and in JUDITH. The temperatures are given along the module (the line 1-1 in Figure 4 - 19). In the IRINA experiment, the temperature is taken at the moment τ_d (Figure 4 - 15). In JUDITH the temperature distribution is taken at steady state for an absorbed power density of 7.5 MW/m^2.

It can be shown that the thermal curves have a very similar profile. In other words, the temperature response of the heat transfer properties on the module surface agrees well for the IRINA and JUDITH experiments.

Significant differences lie in the steady state level of the surface temperature. The temperature difference between a defective area and a zone with good heat transfer in IRINA is in the range of several degrees. In JUDITH it is in the range of several hundred degrees due to higher heat flux. The low value of maximum temperature difference that characterizes a defect area in IRINA high demands on used apparatus for infrared observation (time resolution, spatial resolution) and needs the surface emissivity correction.

The comparison with experimental results for electron beam tests proves the high efficiency of the infrared inspection method. But this method needs additional development and should be used in the future for provisional screening of plasma facing components. In long-term outlook the IR inspection system such as IRINA facility can be used for a first overview on defect zones in modules as quality control tool.

Other examples of infrared inspection in the facility IRINA are described in Appendix.

4.10. Conclusions:

During infrared heat transfer inspection in the IRINA facility the following results were obtained:

1. A correlation of the CFC surface state with the infrared visualization of temperatures has been done. A correction method for the infrared image was proposed taking into account variations of local surface emissivity.
2. The heat transfer properties of CFC armoured high heat flux components were investigated in IRINA. The top and lateral surfaces were observed using an IR camera. Defect zones with reduced heat transfer were detected.
3. An analytical procedure to define areas with reduced heat transfer was developed. Optimum conditions for defect observation were determined.
4. Numerical calculations were carried out for the studied components. Heat transfer during heating up in IRINA and in JUDITH was simulated using FEM. Areas with reduced heat transfer were modelled by the decrease of the thermal conductivity in the joint interlayer.
5. A model experiment to simulate a transverse defect with variable width has been done. An almost linear dependence of the temperature deviation during heating as a function of the defect size was shown.
6. Investigation of the high heat flux behavior of components was carried out in the electron beam facility JUDITH. The results of screening tests confirmed the presence of the defect areas that had been previously identified in IRINA. The potential to use IRINA as preliminary quality control tool was shown.

Chapter 5. Inspection of electron beam loaded plasma facing components

5.1. Preface

The previous Chapter discussed the possibility to apply the infrared inspection method to investigate the heat transfer in a plasma facing component. The aim of such inspection is to detect the defect areas in the structure of a component. This analysis will be able to reveal the pre-existing imperfection caused by manufacturing procedures.

The fact that during the infrared thermography on IRINA some PFCs did not shown areas with reduced heat transfer can be also related to the sensitivity issue of the infrared inspection method. These PFCs are still potential to have the defect areas in their structures. The development of these defect areas can possibly occur during high heat loading in a fusion facility. The tool to investigate the heat transfer degradation of the modules under high heat loads is the electron beam facility JUDITH. This facility is able to subject the PFCs to thermal loads adequate to those in a fusion facility. The facility JUDITH enables a researcher, firstly, to detect the areas with deteriorated heat transfer, and secondly, to analyse the heat transfer degradation in PFCs with different configurations during thermal fatigue loads.

Furthermore, the facility JUDITH was used to investigate the heat transfer degradation induced by neutron irradiation.

5.2. Analysis of CFC flat tile modules

5.2.1. Investigated modules and experimental set-up

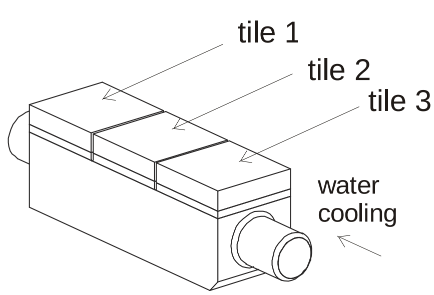

Figure 5.2 - 1. Appearance of the modules FT 107-1,2,3 and FT 109-2,3

The heat removal and the thermal fatigue performance of 5 flat tile modules with the same geometry (FT 107-1,2,3 and FT 109-2,3, see Table A3-1 in Appendix) were investigated under high heat fluxes. Figure 5.2 - 1 shows the schematic drawing of the mock-ups. The armour of the mock-up consisted of three CFC tiles (19 mm x 22 mm x 6 mm) with a gap of 0.5 mm between. The detailed design of the mock-up is illustrated in the Figure A5.2-1 in

Appendix. The thermal fatigue tests were carried out in the electron beam facility, JUDITH (see Chapter 3. 3). During the heat load tests, the mock-ups were actively cooled by water.

The fabrication procedures of the mock-ups FT107-1,-2,-3 was as follows [72]:

1. Machining of the CuCrZr heat sink, CFC (NB31) armour tiles and OFHC Cu interlayer.
2. Metallization of the CFC surface by a Ti foil to produce TiC in order to enhance wettability of the CFC surface
3. Joining of the OFHC Cu interlayer to the CuCrZr heat sink by diffusion bonding. This joining was performed at about 1000 ºC . The OFHC Cu interlayer between the joining surfaces enhances the reliability of the process.
4. Brazing of the metallized CFC to the Cu/CuCrZr using a TiCuNi braze metal
5. Solution annealing, fast cooling and aging
6. Final machining of the component.

The fabrication method of the mock-ups FT109-2,-3 was a combination of joining with laser structuring of the CFC NB31, Active Metal Casting (AMC) with OFHC Cu and joining of the OFHC Cu surface and CuCrZr heat sink by low temperature solid HIP (see Chapter 2.4.2). The HIPing temperature for FT109-2 was 550ºC , whereas, it was only 480º C for FT109-3. This low temperature HIPing process does not influence the mechanical and thermophysical properties of CuCrZr [36].

The material CFC SEPCARB NB 31 is described in Chapter 2.7.

5.2.2. Experimental results

The heat load tests in the electron beam facility, JUDITH are summarized in Table A5.2-1 (Appendix). Two different testing modes were performed: screening test (steady state heating) and thermal fatigue test. Screening tests were performed by increasing the heat loads step-wisely and thermal fatigue tests were performed by cyclic heating at the same heat load up to 1000 cycles. A thermal fatigue cycle consisted of two steps: power loading during typically 10 s and subsequent cooling for 10 s. During the cycles, the surface temperature of the mock-up was monitored by a IR camera. Figure 5.2 - 2 shows the heat loads and the cycle number for each module, where failure occurred. The modules FT107-2, FT109-2 and FT109-3 did not show any failure up to 10

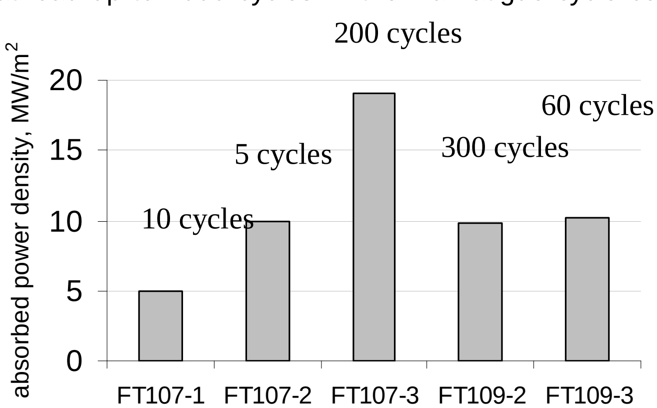

Figure 5.2 - 2. Failure limit of the modules FT 107-1, 2, 3 and FT109-2, 3 in thermal fatigue tests

MW/m^2, on the other hand, failure of the module FT107-1 occurred after 10 cycles at 5 MW/m^2.

FT 107-3 shows the best thermal fatigue performance and heat removal efficiency among the modules. The module was tested during 1000 cycles without significant increase of surface temperature at the absorbed power density of 15.3 MW/m^2. After increasing the power density to 19 MW/m^2 one of the armour tiles finally detached after 200 cycles. Nevertheless, the remaining armour tiles survived under 19 MW/m^2. Figure 5.2 - 3a and Figure 5.2 - 3b present an IR image and the surface temperature evolution of the mock-up, FT107-3 during screening tests. The figure shows surface temperature profiles along the coolant axis (line A - A in Figure 5.2 - 3a). The surface temperature profiles at absorbed power densities below 12 MW/m^2 were constant on all the tiles. However, tile 1 showed slightly higher temperature at 12 MW/m^2 and the temperature difference between tile 1 and the other tiles increased with the higher power densities.

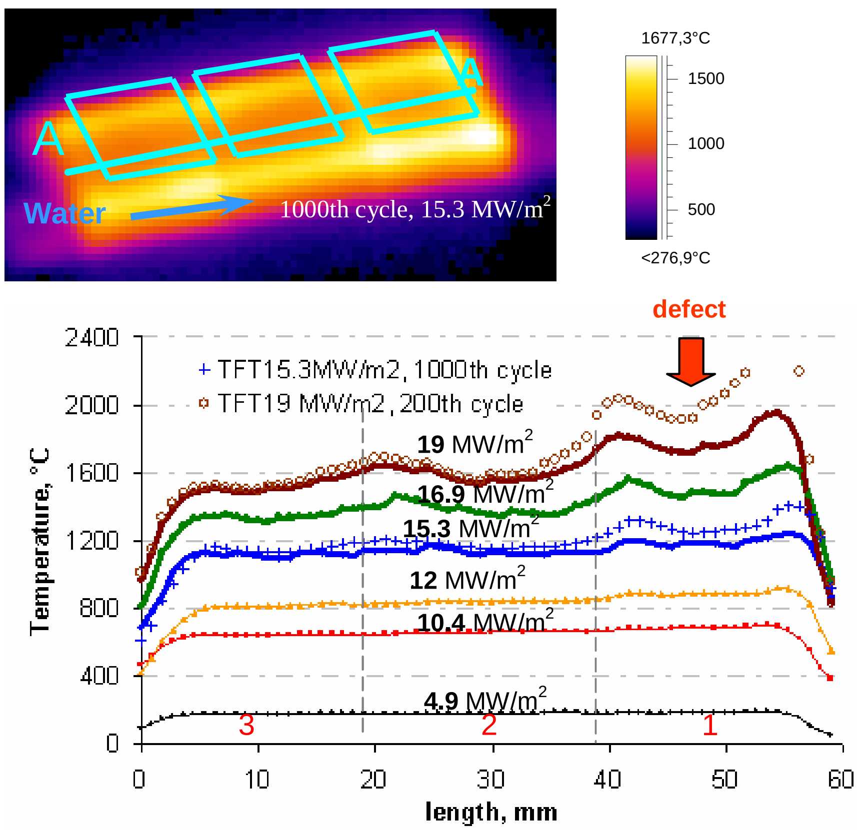

(a)

(b)

Figure 5.2 - 3. Temperature evolution by screening and thermal fatigue tests of the module FT107-3

One thermal fatigue test was performed at an absorbed power density of 15.3 MW/m^2. The temperature distribution along the line A-A of the last cycle (1000th) at this power density is additionally shown in Figure 5.2 - 3 (blue symbol "+"). The surface temperature of tile 1 increased slightly compared to the former screening test. Then a thermal fatigue test was performed at an absorbed power density of 19 MW/m^2. During this loading, the temperature of tile 1 increased continuously and finally after 200 cycles the tile detached (brown circle).

Figure 5.2 - 4a illustrates the surface temperature change of the tiles of the module FT107-3 during thermal fatigue testing at 15.3 and 19 MW/m^2 in logarithmic scale. This surface temperature on a tile was taken from the boxes (shown in Figure 5.2 - 3a) as an average temperature in each cycle. At an absorbed power density of 15.3 MW/m^2, all tiles sustained 1000 cycles of the thermal fatigue test, but the average surface temperature in each cycle of the tiles increased slowly during the test. The increase rate of temperature had a linear character. Surface temperature of the tile 1 was always higher at this load than of the tiles 2 and 3. The increase rate on tile 1 was also close to linear. At a absorbed power density of 19 MW/m^2, the surface temperature of the tile 1 increased rapidly after the 110th cycle and finally the tile detached after 200 cycles, whereas the surface temperature on tiles 2 and 3 increase only slightly. Surface temperature of tile 1 was always higher at this load than the tiles 2 and 3. The increase rates show again linear characters. In case of the tile 1, the increase rate seemed to have two different slopes, below 100 cycles and above 110 cycles (the discussion is in Chapter 5.2.3, Figure 5.2 - 7).

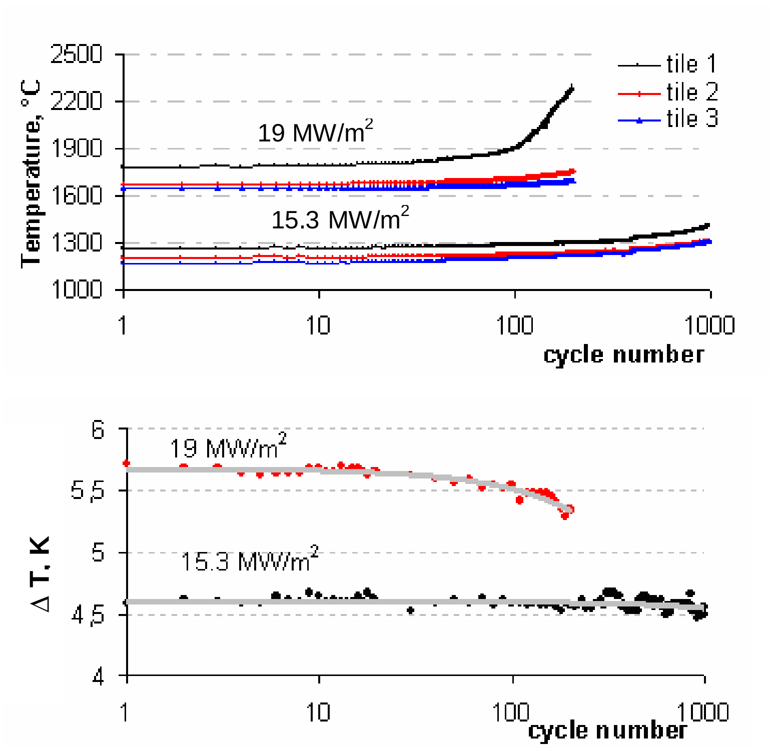

(a) (b)

Figure 5.2 - 4. Temperature increase during thermal fatigue testing of the module FT107-3

Inlet and outlet cooling water temperature were measured by thermocouples. The differences of the temperatures ΔT_{water} are presented in Figure 5.2 - 4b for the two thermal fatigue tests on this module at different power densities. It is obvious that ΔT_{water} decreased with the increase of the surface temperature of the module during the thermal fatigue test at 19 MW/m^2. It can be concluded that this indicates the degradation of heat transfer properties of this module, as the absorbed power density calculated by water calorimetry decreased in the thermal fatigue test with a constant incident power density. Total reduction of absorbed power density reached 1.2 MW/m^2 during 1000 cycles.

The behavior under high heat flux loading and heat transfer degradation of the modules FT 107-1, FT 109-2, FT 109-3 is described in Appendix in Figures A5.2 – 2 – A5.2 – 6.

5.2.3. Discussion

The results of these 5 flat tile CFC modules are presented in Figure 5.2 - 2 and in Table 5.2 - 1. The brazed CFC-module FT 107 achieved the best performance during thermal fatigue loadings. The distinction in manufacturing of this module lies in the surface cleaning process of the interlayer during the joining phase. This process obviously improved the quality after joining. The brazed modules show good thermal fatigue performance generally at higher loads than the HIPed modules [29,38].

Table 5.2 - 1. Overview of mock-ups failure history

Module	Failure	Test, absorbed power density, number of cycles
FT 107-1	Detachment of tile 2	TFT at 4.9 MW/m^2 after 10 cycles
FT107-2	Detachment of tile 1 Detachment of tile 2 Detachment of tile 3	ScT at 9.9 MW/m^2 ScT at 10.1 MW/m^2 TFT at 10 MW/m^2 after 5 cycles
FT107-3	Detachment of tile 1	TFT at 19 MW/m^2 after 200 cycles
FT109-2	Detachment of tile 1 Detachment of tile 2	TFT at 5.2 MW/m^2 after 35 cycles TFT at 9.8 MW/m^2 after 300 cycles
FT109-3	Detachment of tile 1	TFT at 10.2 MW/m^2 after 60 cycles

(a) FT107-2, tile 1 is absent, tile 2

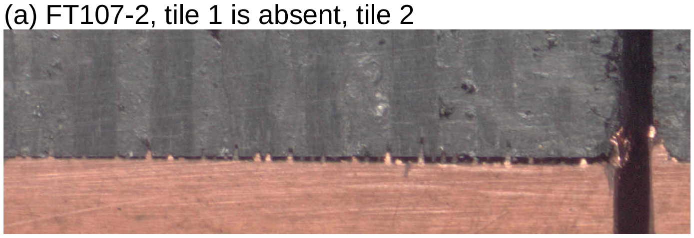

(b) FT109-3, tile 1

Figure 5.2 - 5. Tiles detached during thermal fatigue loading

The analysis of data for the five modules showed that for 4 modules tile 1 was the first to detach. In the experiments tile 1 is situated on the water outlet side. Another reason of this might be apparently connected to technological peculiarities of manufacturing. Figure 5.2 - 5 demonstrates the high resolution image of detached tiles after electron beam loading. From the analysis of typical failures of the armour during thermal fatigue it can be concluded that the structural damage of a mock-up happens due to detachment of CFC armour from the interlayer material (Figure 5.2 - 5). For example, for the modules manufactured by AMC and HIP technology (series FT 109-2, -3) the most brittle layer is the thick titanium carbide TiC. In the brittle layer cracks formation occurred due to thermal stresses during thermal cycling [73].

The heat transfer degradation of the module during cyclic loadings is characterized by the evolution of the surface temperature. The surface temperatures as a function of cycle number in logarithmic scale for all tiles of the investigated modules FT 107-3, FT 109-2, FT 109-3 are presented in Figure 5.2 - 6. The average surface temperatures of each tile per cycle were measured as shown in infrared image in Figure 5.2 - 3.

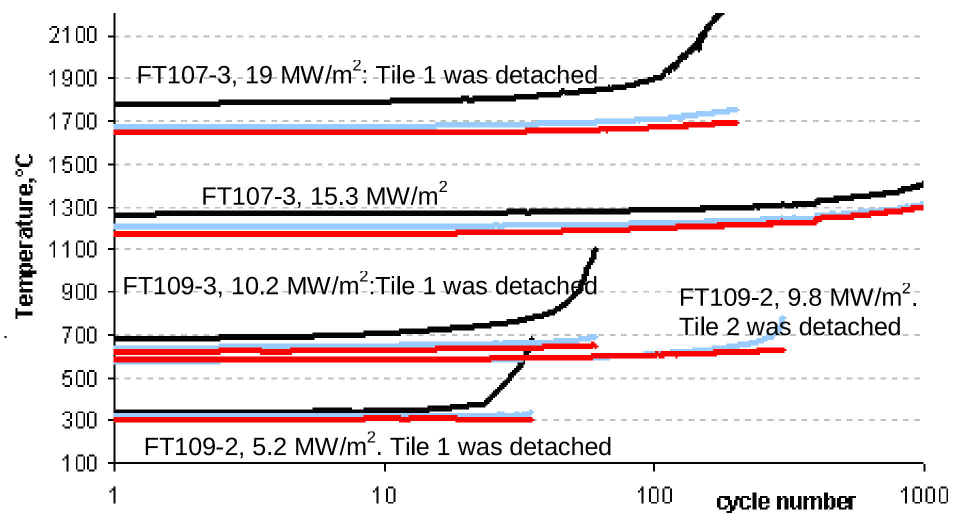

Figure 5.2 - 6. Surface temperature evolution during thermal fatigue testing: tile 1- black, tile 2 – blue, tile 3 –red

The curves of temperature variation vs. cycles include information of the damage process. The analysis was carried out on the module FT 107-3 at an absorbed power density of 19 MW/m^2. The curves are presented in Figure 5.2 - 7a.

As it may be seen in Figure 5.2 - 7 the temperature on tiles 2 and 3 increases with cycle number according to a linear law $T=\alpha N+T_o$, where T_o is a surface temperature of the tile after first cycle, α - the temperature increase rate, and N – the cycle number. After 200 cycles the temperature increment was ~80°C and ~50°C for the tiles 2 and 3, what corresponds to an increase of less than 5%. The surface temperature on the tile 1 was higher than on the tiles 2 and 3 already after the first cycle. The surface temperature of the tile 1 increased rapidly with cycle number. For example, during first 100 cycles the temperature increment was ~120°C with an almost constant temperature increase rate of 1.2 K/cycle. The change of the temperature increase rates occured after 100th cycle approximately, when the surface temperature of tile 1 reached 1900°C. Probably, catastrophic breakdown started at this moment in the module structure. It resulted in sharp temperature growth. The temperature increased by 400°C during the next 100 cycles (a temperature increase rate of 4 K/cycle) and finally it caused a detachment of the armour tile.

The curve of surface temperature on the tile 1 T=T(N) can be fitted with two linear curves. These 2 regimes are clearly to be seen on the diagram of the derivative of the surface temperature $\dot{T} = \dot{T}(N)$ (Figure 5.2 - 7b).

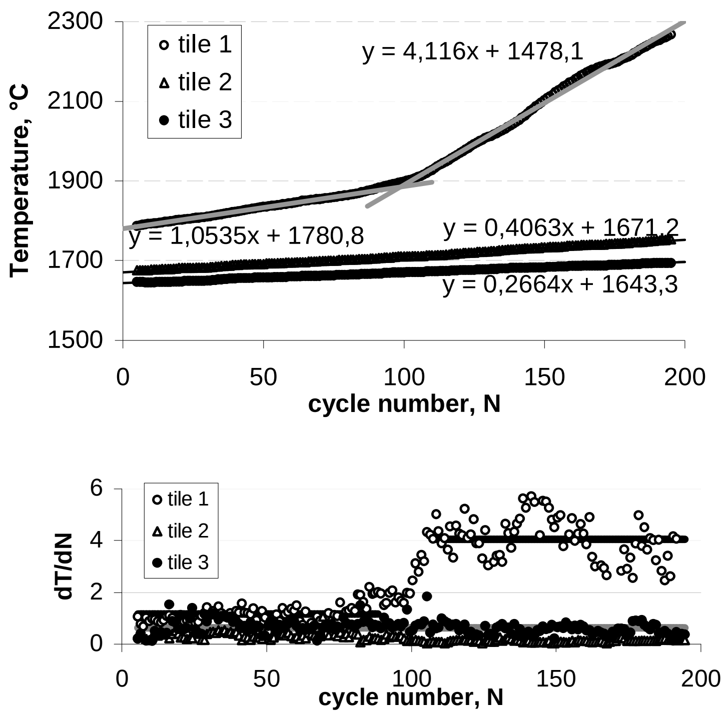

(a)

(b)

Figure 5.2 - 7. Analysis of temperature change curves of the module FT 107-3 during thermal fatigue loading at absorbed power density of 19 MW/m^2: (a) average surface temperature of the tiles, (b) derivative of surface temperatures

Figure 5.2 - 6 shows that the character of the temperature curves of all detached tiles was similar to the one described above. However the initial temperature T_o and slope α are different. Difference in T_o between two tiles of the same type might occur due to disturbances in the heat flow, namely cracks perpendicular to the heat flow direction in the joining layer, which are determined during manufacturing. If such cracks exist, they might grow during thermal fatigue loads and as a result degrade the macroscopic heat transfer properties. Thus, a fast crack growth is responsible for a high α -value.

Thus, the module produced by the same manufacturing technology roughly can be controlled by the coefficients T_o and α. If there are some manufacturing imperfections, what can strongly disturb heat transfer in a module, it will be already indicated during the first 200 cycles. As a result short time fatigue tests can indicate by T_o and α whether a module meets the quality requirements or not.

For a correct estimation of the coefficients T_o and α, it is necessary to evaluate the statistical data of thermal fatigue testing of the mock-ups in terms of manufacturing technology. But this fast control can give no information about evolution of imperfections in a module due to thermal fatigue.

Figure 5.2 - 8 shows the temperature fields on the surface of tile 1 in the module FT 107-3 during 200 cycles thermal fatigue test at 19 MW/m^2. It was accepted that the surface overheating occurs at temperatures higher than T_{over}=T_{av}+50% T_{av}. T_{av} is the average temperature of the module surface after first cycle, when the module does not yet show the failure. For the module FT 107-3 T_{av} =1750°C, then T_{over}≈2600°C. Red fields in Figure 5.2 - 8 correspond to the area above 2600°C. These areas are named „zone of significant overheating".

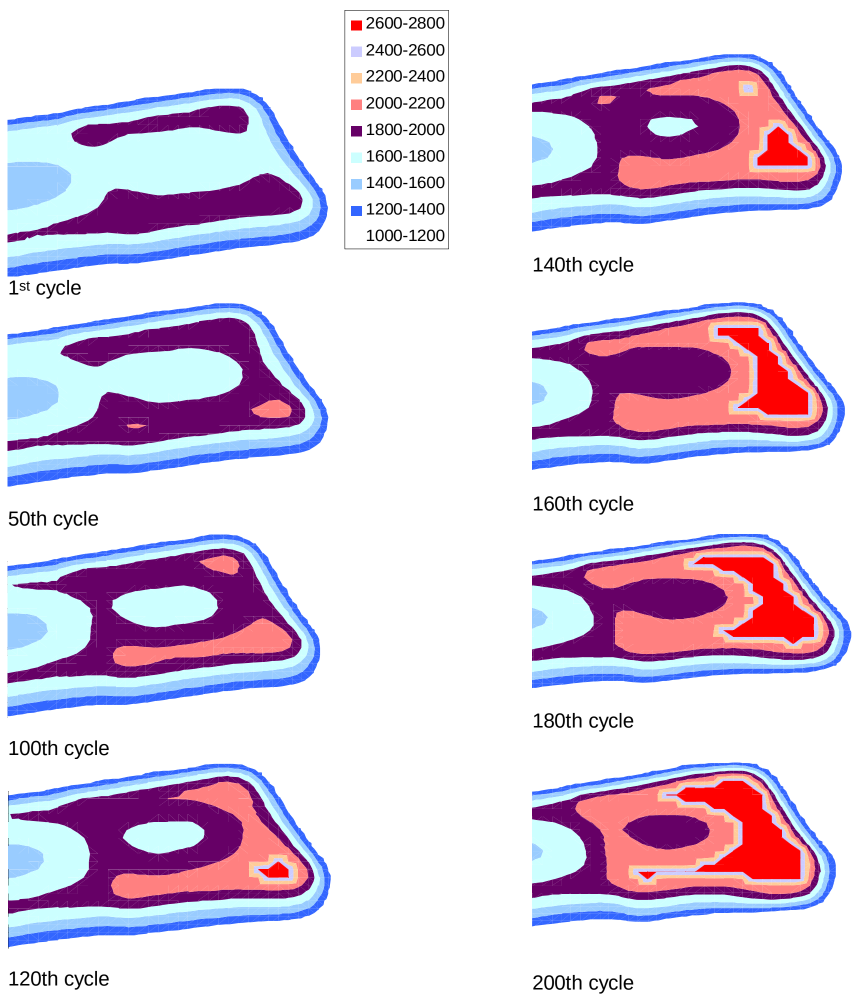

Figure 5.2 - 8. Evolution of an area with disturbed heat transfer during thermal fatigue loading of the module FT 107-3 at 19 MW/m^2

Other examples of temperature fields evolution are shown in Figures A5.2 –7 –A5.2 –9 in Appendix.

As mentioned above, the change in the slope of the temperature vs. cycle curve for tile 1 (Figure 5.2 - 7 a) took place after 100 cycles approximately. As shown in Figure 5.2 - 8, the temperature on the edges of the tile is higher than in center. This fact is connected with the position of the cooling tube (in center of the module), where the modules have the best cooling condition, and probably with the best quality of brazing in the center area.

All tested modules show that the zones of significant overheating are conceived in the edge areas. The zone of significant overheating enlarges along the exterior of the tile in this case. The overheated areas appear in the interior of the tile 1 contiguous to tile 2 only in the module FT 109-3 (Figures A5.2-9 in Appendix)

From the analysis of Figure 5.2 - 8 some important facts can be derived:

1. A zone of significant overheating developed in the right bottom corner of tile 1 after approximately 120 cycles. Then with increasing cycle number this zone extends to the opposite sideface of the module.
2. The overheated areas were observed not only on the top surface but also on the lateral area of the armour (Figure 5.2 - 8, cycle no. 200). It indicates the remarkable warming-up into the armour material. This fact is clearly observed by video observation of the sample at cool down at the end of thermal fatigue cycling (Figure 5.2 - 9).
3. Expansion of the overheated area on the module surface was apparently connected to the propagation of a joining defect between armour and joint interlayer, what finally caused the detachment of the tile.
4. The presence of the “colder” spot in the center of tile 1 indicates the good contact and a high heat transfer of this area.

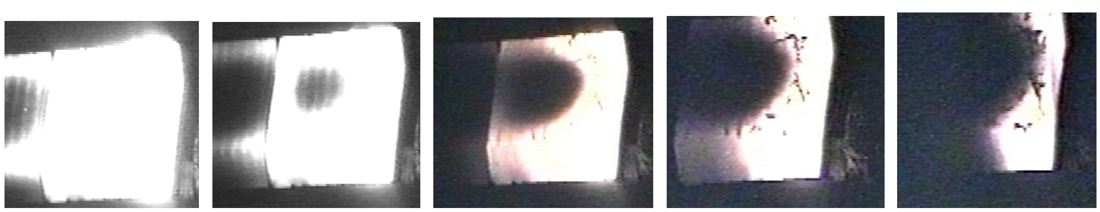

Figure 5.2 - 9. FT 107-3: Cooling down of the tile 1 after switching off the electron beam at 19 MW/m^2

5.2.4. Numerical modelling

The behavior of a flat tile CFC module as shown in Figure A5.2-1 (Appendix) under high heat flux loads was simulated by FEM with the program ANSYS. Surface heat flux on the top surface and convection of coolant in the cooling tube were applied as the heat load conditions. The temperature dependent physical properties of the materials CFC, OFHC Cu, CuCrZr were taken from the ITER database “ITER plasma facing component materials database in ANSYS format" [74]. The 3D geometry was modeled. For the calculation a heat flux at the power density of 19 MW/m^2 was assumed for a duration of 30 s.

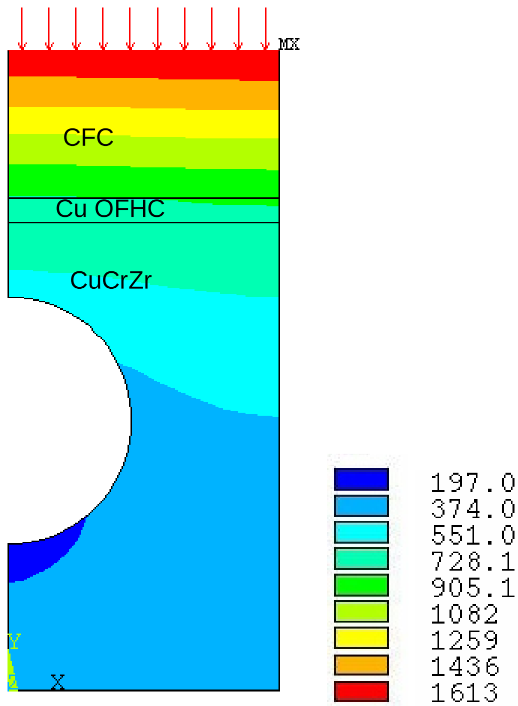

Figure 5.2 - 10. FEM calculated temperature distribution in the module FT 107-3 at 19 MW/m^2

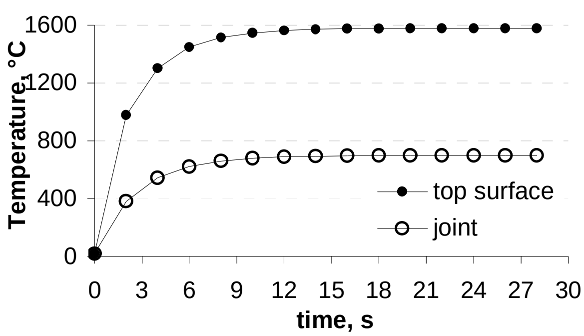

Figure 5.2 - 11. Temperature evolution in cross section: top surface and joint at absorbed power density of 19 MW/m^2

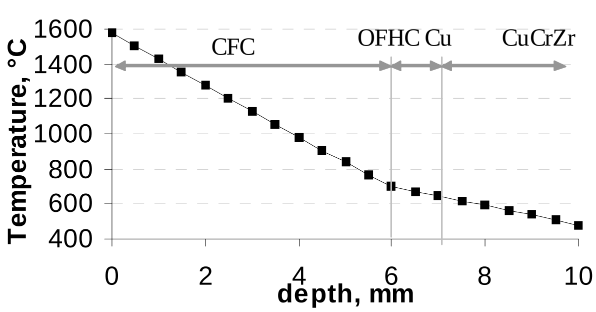

Figure 5.2 - 12. Temperature distribution in the direction of depth at absorbed power density of 19 MW/m^2

First step of calculation was to model a mock-up, in which the ideal case of the heat transfer would be realized and the model would not include faults. This model is labeled as "zero-defect module".

Figure 5.2 - 10 shows the temperature fields distribution in the cross section of the zero –defect module after the heating for 30 s at a power density of 19 MW/m^2. The module is found in steady state conditions at that time. It is obvious that in spite of the complicated module geometry the temperature front in the CFC is practically parallel to the surface. The temperature difference between center (above the cooling tube) and the module edges was calculated to be around 20 K.

Figure 5.2 - 11 shows the calculated results of temperature evolution on the CFC surface and at the interface between CFC and the joint material. The temperatures in these two planes increased synchronously. During the first 10 seconds of loading the CFC surface and the joint interlayer reach a stationary temperature of 1600°C and 700°C respectively. The calculated surface temperature of 1600°C is in good agreement with experimental data (Figure 5.2 - 3).

Figure 5.2 - 12 shows the

temperature profile along the axis of symmetry from surface to the upper rim of the cooling tube. The Figure 5.2 - 12 shows that within the CFC armour the temperature was reduced to less than 50%. But in spite of this at the interface between the CFC armour and the joint a temperature reaches high value of about 700°C.

Inspections of the modules after high heat flux testing (as shown in Figure 5.2 - 6 above) indicated that failure occurred in the joint interlayer zone. Significant heating of the module caused tensile stresses, fatigue crack nucleation and finally it led to detachment of the CFC armour that was associated with a sharp decrease on the heat transfer properties of the module.

A second step of calculation was to model the effect of reduced heat transfer properties for the module FT 107-3, that was heated by a surface load of 19 MW/m^2. In this calculation the reduction of heat transfer properties of the module (in particular, thermal conductivity) in joint area under tile 1 was considered.

In Figure 5.2 - 3 the experimental results of screening of the module FT 107-3 are presented. This picture shows the significantly higher temperature on tile 1 in comparison to tiles 2 and 3 during the first screening test at absorbed power density of 15.3 MW/m^2. At this load the surface temperature on tile 1 reached approximately 1200°C. At the same time the temperature at the interface between CFC armour and OFHC interlayer reached approximately 500°C according to the FEM temperature calculations. Thus, an abnormality of heat transfer appears in the region of tile 1 at surface loads of 15.3 MW/m^2 at the interface between CFC and joint interlayer heated up to about 500°C. Consequently, this was the starting point for the degradation of the joint which finally led to a detachment of the tile 1.

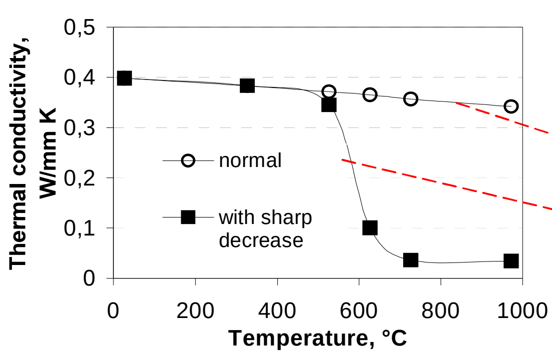

Figure 5.2 - 13. Degradation of thermal conductivity in OFHC

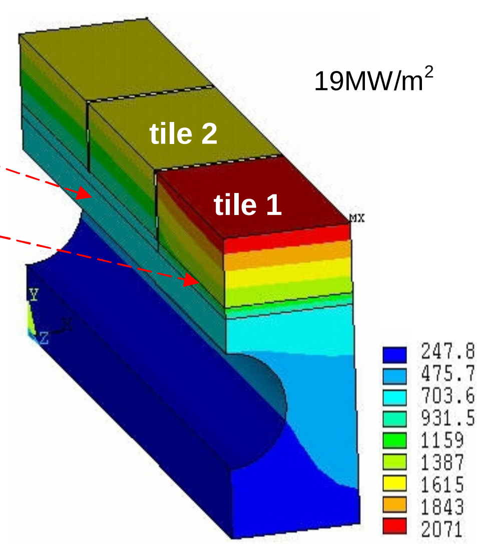

Figure 5.2 - 14. Numerical model: interlayer under tile 2 has the thermal conductivity of OFHC, thermal conductivity of interlayer under tile 1 is strongly reduced as shown in Figure 5.2 – 13

Apparently, the presence of defects in the joint results in a dramatical decrease of heat transfer properties. Modelling of this effect was carried out by means of an “artificial reduction” of the thermal conductivity of the OFHC interlayer material. The curve of the assumed decrease in thermal conductivity is shown in Figure 5.2 - 13. Reduction of thermal conductivity of OFHC started at 500°C and decreased sharply to 1/10. A possible mechanism of the reduction of the heat transfer properties is crack formation [75, 76] in the OFHC interlayer.

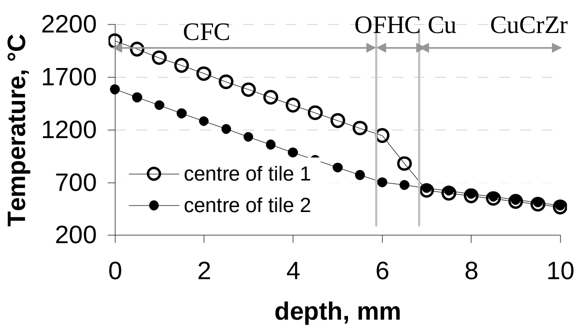

Figure 5.2 - 15. Temperature distribution in module FT 107-3 according to FEM calculation at 19 MW/m^2 in tile 1 and tile 2 at steady state conditions

The results of FEM calculation are presented in Figure 5.2 - 14 and Figure 5.2 - 15. Figure 5.2 - 14 shows the assumed temperature fields in the model in the direction of the depth at power density of 19 MW/m^2. Here the thermal conductivity of the joint interlayer at CFC tile 1 decreases sharply after temperatures above 500°C are reached in the joint interlayer (as shown in Figure 5.2 - 13). The joint interlayer below tile 2 and tile 3 was assumed to have thermal conductivity of OFHC material. As a result, the temperature on the tile 1 is much higher then on the others.

Figure 5.2 - 15 shows the temperature distribution from surface to the cooling tube in the center of the tile 1 and tile 2. Here a clear temperature jump in the joint region of tile 1 can be seen. The temperature is reduced from 1150°C to 650°C. This temperature drop is defined by thermal conductivity change. Moreover, the significant temperature rise was observed not only at the interface between joint interlayer and CFC but also in the CFC armour. Thus, as a consequence of numerical modeling of the process of heat transfer degradation in a CFC module, it was shown that on the CFC surface different temperatures occur during heat loading. This is caused by different qualities of the joint interlayer.

Figure 5.2 - 16 illustrates the comparison of the calculated temperatures and the experimental data. It shows the temperature profile along the line A-A and comprises it to the calculated temperature. The temperatures on the tile 1 and on tiles 2 and 3 in the experiment are around 2000°C and 1600°C, respectively. Temperatures calculated using FEM is in agreement with experimental data.

It confirms the presumption of the degradation of heat transfer properties in the joint interface.

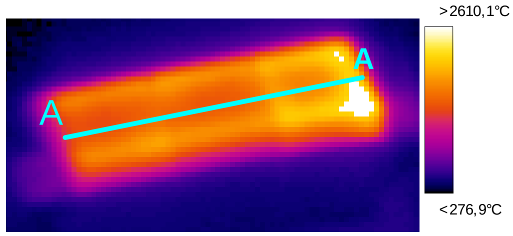

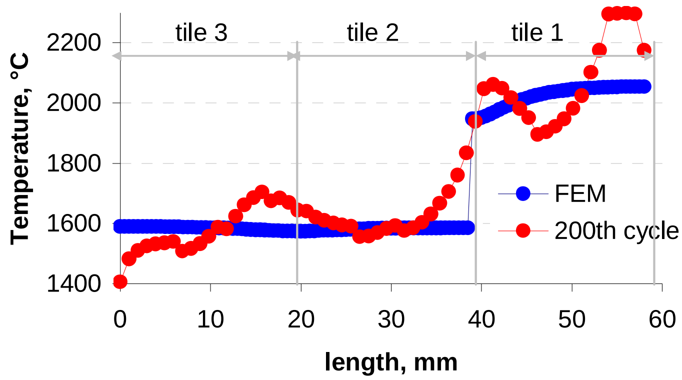

Figure 5.2 - 16. Comparison between calculated temperatures using FEM and the experimental temperature profile after 200th cycle at 19 MW/m^2

5.2.5. Conclusions

Major results of the electron beam inspection of plasma facing components with CFC armour were obtained:

1. The analysis of thermal fatigue behavior of five CFC flat tile modules was carried out. The best performance during thermal fatigue showed the brazed module compared to the HIPed components.
2. During the evolution of a tile failure the surface temperatures increase typically in two regimes with different temperature increase rates and the tiles detached after a certain number of cycles. It was found that slow temperature increase characterizes small structure imperfections growing with thermal fatigue. A strong surface temperature increase indicated catastrophic crack propagation leading to armour detachment.
3. The evolution of surface temperature fields for CFC modules represent the thermal response induced by the degradation of the joint interlayer and give comprehensive information on the detachment processes.
4. Heat loading of CFC modules was modelled by means of FEM. It is proposed to describe the process of the joint interface destruction by means of the reduction of the thermophysical characteristics.

5.3. Analysis of beryllium flat tile modules

5.3.1. Investigated modules and experiment-setting

In order to investigate the special features of the heat removal and the thermal fatigue behavior of plasma facing components with beryllium armour manufactured by different joining techniques, the high heat flux testing in the facility JUDITH was carried out. The modules FT 108, FT 99-1, -2, FT 119-FT 122 and FT 111 were analysed. The detailed information about the module structures and joining techniques is presented in Table A5.3-1 in Appendix.

The armours of the modules FT 108, FT 99-1 and FT 99-2 were designed as one flat tile. The armours of the modules FT 119-FT 122 consisted of 4 tiles of the same size. The drawings and geometrical sizes of the modules are shown in Figure A5.3-1 and A5.3-2 in Appendix.

The detailed description of the experimental loadings and testing results is summarized in Table A5.3-1 (Appendix).

The loads consisted of the combination between screening and thermal fatigue tests. First, the screening test at low heat load was applied (absorbed power density of around 0.5 MW/m^2). Then the load was stepwise increased up to 1.5 MW/m^2 and screening tests were carried out at each power density. The next step of investigation was to load a module under cyclic heat flux at the absorbed power density of 1.5 MW/m^2. This value of thermal loads is approximate loads that are expected to be on the first wall in ITER. 1000 cycles of thermal fatigue load were applied at the absorbed power density of 1.5 MW/m^2. If the thermal fatigue test at this condition was successful, the module was then loaded at higher power density.

Cooling condition was as follows: temperature of coolant water=19°C, the pressure=36 bar, water flow rate=60 l/min. During testing of the modules FT 108 and FT 111 the water velocity was 24 l/min at 7.2 bar.

The surface temperature was measured with an IR camera. The emissivity of the modules with beryllium armour was set to have the value of 0.7. The following facts were considered while choosing the emissivity value.

In [77] investigations on the beryllium surface emissivity were performed. It was shown that emissivity of Be strongly depends on the surface conditions (BeO level, roughness, etc.). Moreover, at low temperature (RT – 600°C) the emissivity of beryllium surface can vary from 0.1 up to 0.6 for the same grade in the same experiment. With the increase of surface temperature, the emissivity of the same sample can rise up to 0.9 [77]. Thus, the emissivity of beryllium can vary from 0.1 up to 0.9 during one experiment.

Taking into account the facts described above it is necessary to note that there are several reasons of non-uniform temperature distribution on the module surface during thermal fatigue testing. They are: the emissivity variation depending on the beryllium surface condition, the temperature dependence of emissivity, the cooling conditions and the evenness of heat transfer properties in the joining layer. But the correction of the surface emissivity coefficient for beryllium modules is not possible, because during electron beam loading the oxide layer redistributes and surface emissivity can be changed [77]. Moreover, the use of the procedure of surface emissivity correction described in Chapter 4.4 is not correct for beryllium modules due to significant variation of emissivity coefficient and temperature dependence of the emissivity coefficient.

Table 5.3 - 1 summarizes the results of high heat flux testing. As it is described in Table A5.3-2 (Appendix) five modules did not show any failure during 1000 cycles of thermal fatigue and the surface change indicating heat transfer degradation was not observed

Table 5.3 - 1. Overview of beryllium module failure history

Module	Failure	Test, absorbed power density, number of cycles
FT 99-1	Detachment of tile 1	ScT at 3.0 MW/m^2
FT 99-2	Detachment of tile 1	ScT at 3.1 MW/m^2
FT108	Failure of tile 1	TFT at 2.1 MW/m^2 during 2nd cycle
FT119	Failure of tile 1 and 4	ScT at 2.5 MW/m^2
FT120	Detachment of tile 1	TFT at 2.0 MW/m^2 during 17th cycle
FT121	Failure of tiles 1 and 2	ScT at 2.0 MW/m^2
FT122	Detachment of tile 1	TFT at 2.6 MW/m^2 during 1st cycles
FT111	Failure of tile 1 Failure of tile 4 Failure of tile 4	TFT at 1.5 MW/m2 during 65 cycles TFT at 1.5 MW/m2 during 1000 cycles ScT at 1.5 MW/m2

Investigated beryllium modules showed the different thermal fatigue behavior under high heat flux due to the heat transfer degradation. Two typical ways of failure were determined:

1. heat transfer degradation during screening test;
2. heat transfer degradation during thermal fatigue loading.

5.3.2. Armour failure during screening loads

Failure of several modules occurred at screening loading (Table 5.3-1). The beryllium tiles of the module FT 99-1 were HIPed to a heat sink made from CuAl25 (Figure A5.3-1 in Appendix). During the period of applying of the loads (Table A5.3-2, Appendix) the failure occurred at a screening load.

Figure 5.3 - 1a shows the mean surface temperature of the module FT 99-1 during screening test. In an infrared image at absorbed power density of 3 MW/m^2 (Figure 5.3 - 1b), inhomogeneous temperature fields were observed. This can be connected both with the presence of an oxide film resulting in different surface emissivities, or with surface

overheating due to the presence of defects in the joint at the edges and inhomogeneous heat transfer in the module.

Thermal expansion of areas with higher temperature (so-called “local overheated zones”) on the beryllium surface during loadings deserves special interest. The expansion of overheated zones corresponds to degradation of heat transfer through the module.

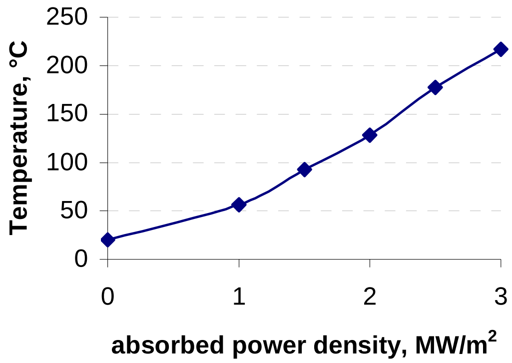

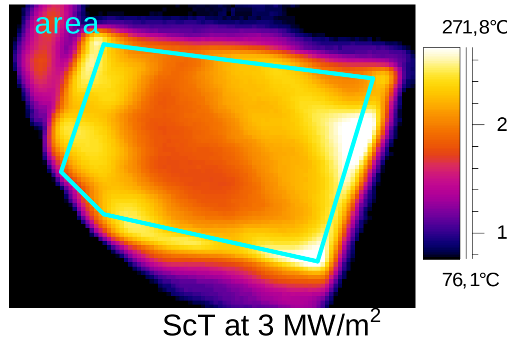

(a) (b)

Figure 5.3 - 1. Mean surface temperature during screening test of the module FT 99-1

The evolution of temperature field distribution is shown in Figure 5.3 - 2a. At low absorbed power density of 2 MW/m^2 the overheated area is clearly visible along the right edge of the armour tile. This area expanded with the increase of heat load up to 2.5 MW/m^2 and the temperature gradient from the central area to the right edge increased. The expansion of the overheated area propagated along the edge. Finally it expanded along the perimeter of the tile at an absorbed power density of 3 MW/m^2.

In Figure 5.3 - 2b the relative temperature T/T(30) along the line B-B (Figure 5.3 - 2a) at 2, 2.5 and 3 MW/m^2 is shown. Temperature T(30) is the temperature at a point with the coordinate 30 mm on the line B-B (Figure 5.3 - 1). The increase of the temperature gradient along this line with increasing heat load is clearly seen.

Failure of the beryllium armour of module FT 99-1 occurred during the heating up by screening test at an absorbed power density of 3 MW/m^2. Optical pictures of failure in different time moments taken with a CCD camera are shown in Figure 5.3 - 3. When the module reached the steady state under the electron beam loading at 3 MW/m^2, the overheating on the edges started to increase. The first optical image corresponds to the picture of surface temperature fields at 3 MW/m^2 (Figure 5.3 - 3). The overheated zone expanded from edges to the center of the tile and reached the maximum after about 2.5 s. Relatively cold spot was located only in center of tile, where the cooling conditions of the module were the best.

Several reasons may be responsible for the overheating of the edges:

1. The scanning modus of a surface with electron beam in JUDITH (edge areas are heated stronger due to electron beam trajectory pattern on a surface) [78];

2. Heat transfer and cooling condition in the edge areas are worse than that in the central area due to the module geometry;
3. Reduction of the heat transfer due to the degradation of the joint between beryllium armour and the Cu heat sink.

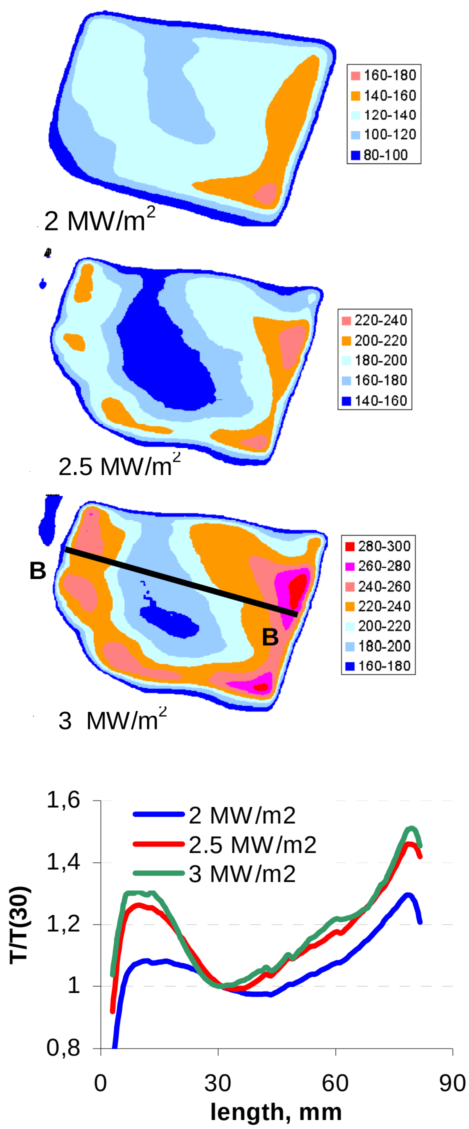

(a)

(b)

Figure 5.3 - 2. Screening tests of the module FT 99-1: (a) temperature fields, (b) temperature profiles along the line B-B

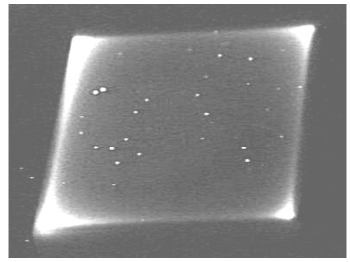

start of edges overheating

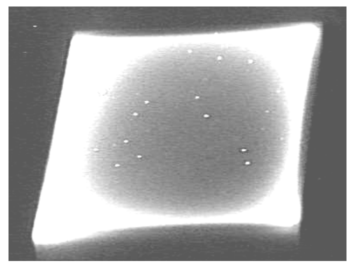

overheated zone is about 50% of tile square (about 1 s after overheating start)

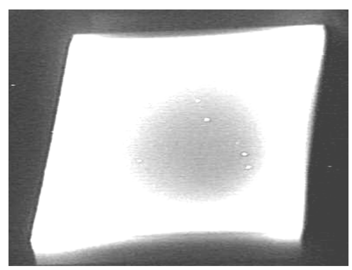

maximal overheated zone (about 2.5 s after overheating start)

Figure 5.3 - 3. Failure of the module FT 99-1 during heating up by screening at constant load of 3 MW/m^2 and inner cooling

The first screening tests at mean absorbed power density of 2 and 2.5 MW/m^2 result in overheating due to the reasons 1 and 2 mentioned above, accordingly in reduce of quality of joint layer between beryllium armour and Cu heat sink on the edges of a module (building of some microcracks or intermetallic phases resulting in degradation of heat transfer flow). Further loading at 3 MW/m^2 causes a growth of the defect zone and an overheating of the module´s edges. Thus, for this module the degradation of heat transfer on the edges was observed with the increase power density. Failure occurred during stationary loading at an absorbed power density of 3 MW/m^2. The zone with higher temperature expanded in a few seconds.

The module FT 108 consisting of CuAl25 heat sink with HIPed beryllium armour showed the failure during the first cycle of thermal fatigue test. This type of failure was assumed to be the damage during screening loading, because the degradation of heat transfer occurred at stationary loading with one separate cycle. From the beginning the module was tested by screening mode at absorbed power densities of 1, 1.5, 2.1 MW/m^2 (Table A5.3-1 in Appendix).

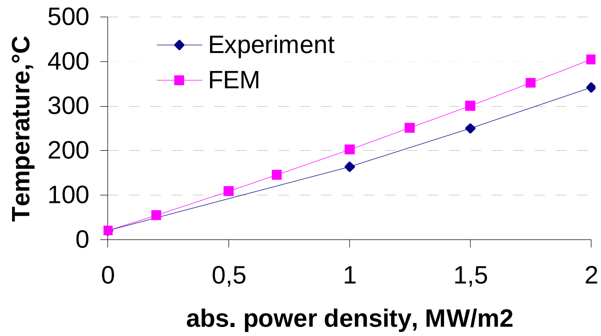

(a)

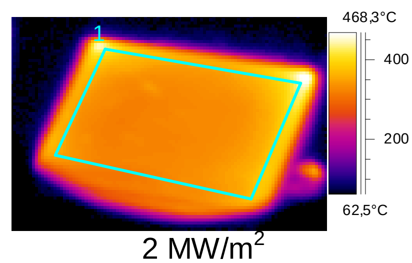

(b)

Figure 5.3 - 4. Screening tests of the module FT 108 (a) surface temperature as a function of the power density (b) infrared image

Figure 5.3 - 4a shows the correlation between the average surface temperature and the absorbed power density during screening test at different heat loads. The infrared image (Figure 5.3 - 4b) shows the averaged area. To determine the average temperature the temperatures at the edges were excluded.

Figure 5.3 - 4a presents also the temperature calculated with FEM, that should be set on the module surface at steady state. The experimental data lie slightly lower in comparison to the calculated temperature. The lower values of measured temperatures can be connected with the fact that the variation of emissivity on the module surface was not taken into account by experimental temperature determination. During measurement emissivity was constant (ε=0.7).

Figure 5.3 - 5a demonstrates the temperature fields on the armour surface of the module FT-108 during screening tests at different absorbed power densities. It is obvious, at minimal load of 1 MW/m^2 the upper corners show higher temperatures. The temperature differences between the upper corners and the center of the tile increased from 60°C up to 140°C at

absorbed power densities of 1 and 2 MW/m^2 respectively. Figure 5.3 - 5b shows the evolution of relative temperature T/T(30) along the line A-A at absorbed power densities of 1 to 2 MW/m^2. The curves T/T(30) at 1 and 1.5 MW/m^2 have the similar character. But the relative temperature increased along the right edge of the tile at 2 MW/m^2. The central area of the module kept good thermal contact to the heat sink and was the coldest part during the screening test.

(a)

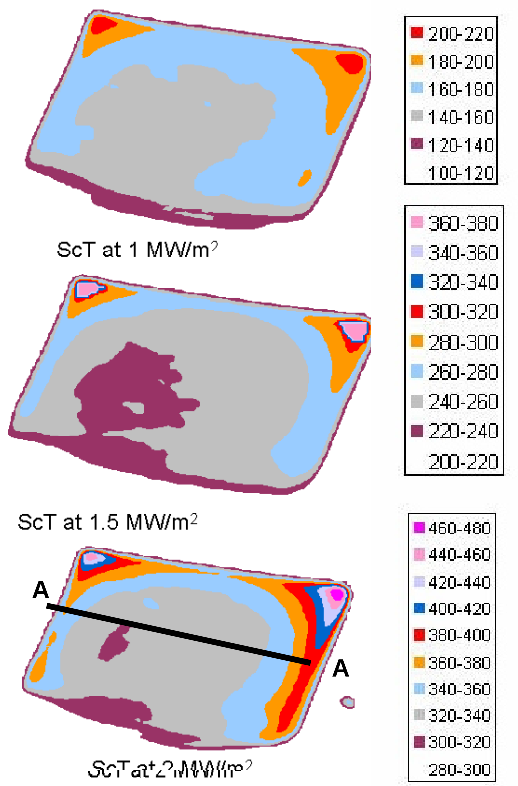

(b)

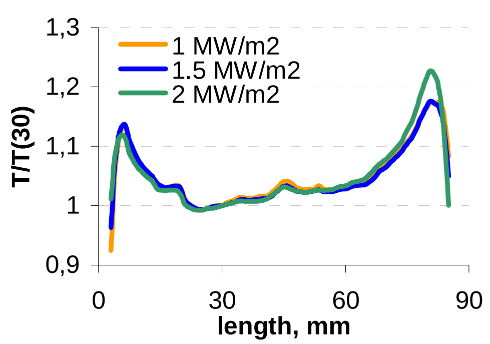

Figure 5.3 - 5. Screening tests of the beryllium module FT 108: (a) temperature fields, (b) temperature profiles along the line A-A

Thermal fatigue test at an absorbed power density of 2 MW/m^2 should have been carried out, but during the first cycle the beryllium armour detached. The detachment of the armour after changing from screening to thermal fatigue is observed quite often with beryllium modules. This following explanation for the effect can be offered. During the high heat flux loading structure defect accumulation occurs at the joint between beryllium and Cu heat sink (for example, intermetallic compounds of beryllium form or microcracks are created). If the loading condition is changed from screening to thermal fatigue test, the heating condition of a module is also changed. At screening test the power of electron beam is increased relatively slowly during about 15-20 seconds, and the module reaches the steady state condition over a long period of time. At thermal fatigue test however, the heat load increases from 0 to the present value in a short time of 0.5-1 seconds. This fast heating causes significant thermal stresses in the interface between the beryllium armour and the Cu heat sink, that result in a failure of the armour tiles (thermo shock loading).

The detailed descriptions of thermal fatigue behavior of other modules with beryllium armour during high heat flux loadings in the facility JUDITH is presented in Appendix .

5.3.3. Armour failure during several cycles of high heat loads

In contrast to the other modules described above, the heat transfer between the beryllium armour and the heat sink of the module FT 111 degraded continuously (during 65 cycles of the loading at 1.5 MW/m^2 on tile 1 and during 1000 cycles of the loading at 1.5 MW/m^2 on the tile 4)(Table 5.3 - 1).

The module consisted of a 60 mm thick 316L stainless steel back plate joined by HIPing onto a 20 mm thick CuAl25 alloy with 10/12 mm 316L stainless tubes embedded in-between. There are six beryllium tiles of different size with thicknesses of 10mm. The beryllium grade S-65C produced by Brush Wellman was used. A drawing of the module is presented in Figure A5.3-3 in Appendix. Figure 5.3 - 6 presents a picture of the module and the numbering scheme of the armour tiles. The module was tested at thermal fatigue loads. In Table A5.2-1 (Appendix) the loads are described in details. This module showed surface overheating, which progressed during thermal fatigue cycling.

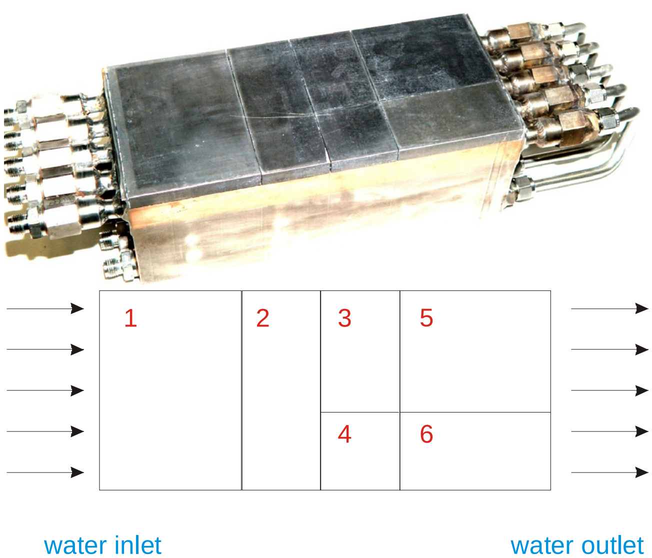

Figure 5.3 - 6. Appearance of the module FT 111 and experimental scheme

Using the example of module FT 111 the evolution of an overheated zone on the armour surface will be discussed in details. To illustrate the process, tile 1 was chosen, it showed heat transfer degradation resulting in surface overheating at thermal fatigue test during 65 cycles. The dimensions of the tile are 10 x 110 x 82 mm^3.

As mentioned above, the surface emissivity makes a significant impact on the interpretation of the surface temperatures of beryllium armours by infrared observation. For tile 1 the variation of surface temperature in steady state was between 65 and 104°C at the load of 0.4 MW/m^2. This corresponds to an emissivity variation from 0.55 to 0.75. This relatively small variation of the emissivity allows normalize surface emissivity in the way described in Chapter 4.4. An infrared image in the steady state at this load was taken as reference. Correction coefficient for each surface point was defined through formula (4-1) (Chapter 4.4).

Figure 5.3 - 7 presents temperature distributions on tile 1 during thermal fatigue test at an absorbed power density of 1.5 MW/m^2. Surface temperatures were re-counted taking into account an emissivity correction coefficient for each image pixel.

During the 1st load cycle two temperature zones with a temperature difference of 50°C are clearly observed on the surface (Figure 5.3 - 7, 1st cycle). After 20 cycles a steep gradient of the surface temperature appeared. The maximal temperature difference reached 250°C between the coldest zone (vinous color) and highest zone (rose color).

After 50 cycles the surface temperature started to increase sharply, and during the next 15 cycles tile 1 showed significant overheating.

The fact, that during thermal fatigue cycling tile 1 started to overheat and the overheated zone expanded with time, is probably due to degradation of the joining layer quality. This might be connected to several processes:

1. growth of pre-existing joint defects as a result of thermal fatigue loading;
2. thermal stresses causing crack formation within the joint;
3. formation of beryllium intermetallic phases at the interface during the high temperature regime of the edges.

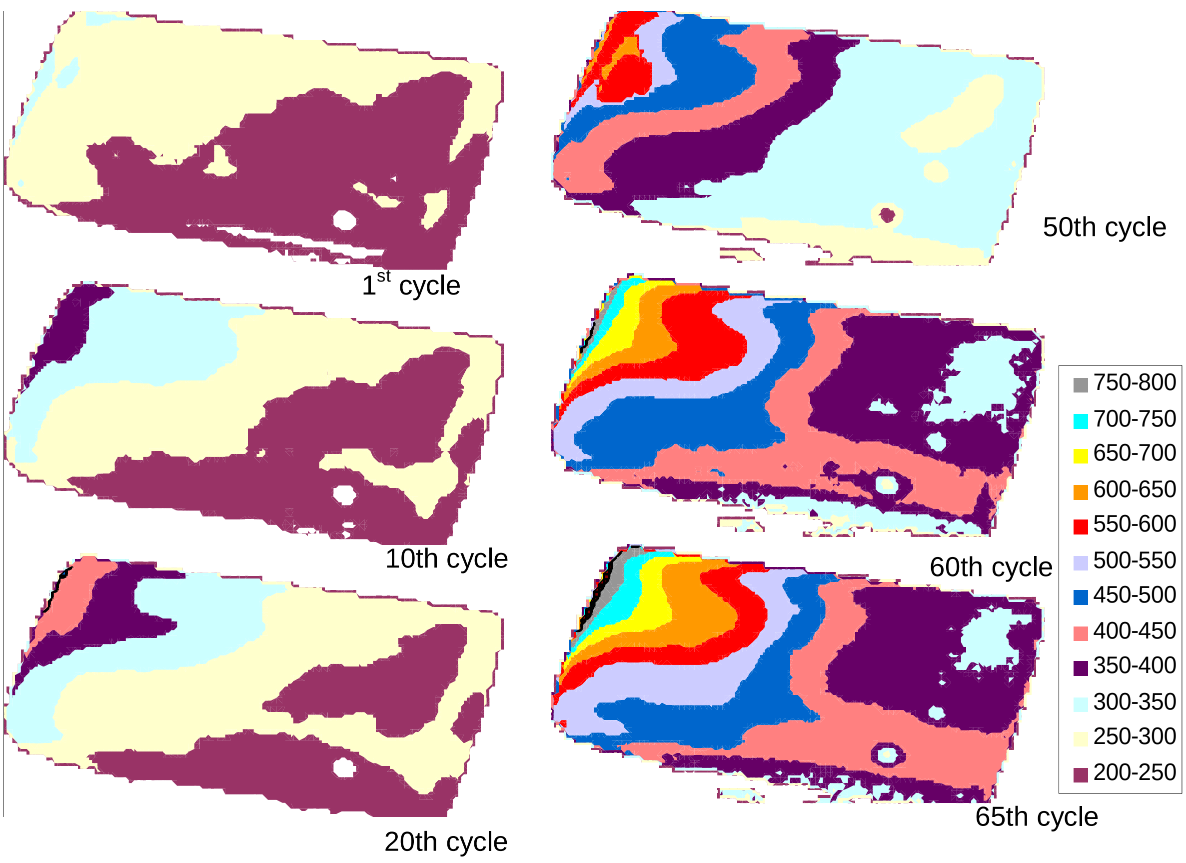

Figure 5.3 - 7. Temperature fields on the surface of tile 1 of the module FT 111 during 65 cycles of thermal fatigue loading at absorbed power density of 1.5 MW/m^2

The first two reasons depend on the quality of the manufacturing joint influencing the heat transfer efficiency from the surface to the cooling tube. Intermetallic phase formation depends on the temperature and chemical composition on the vicinity of the joint. The joining

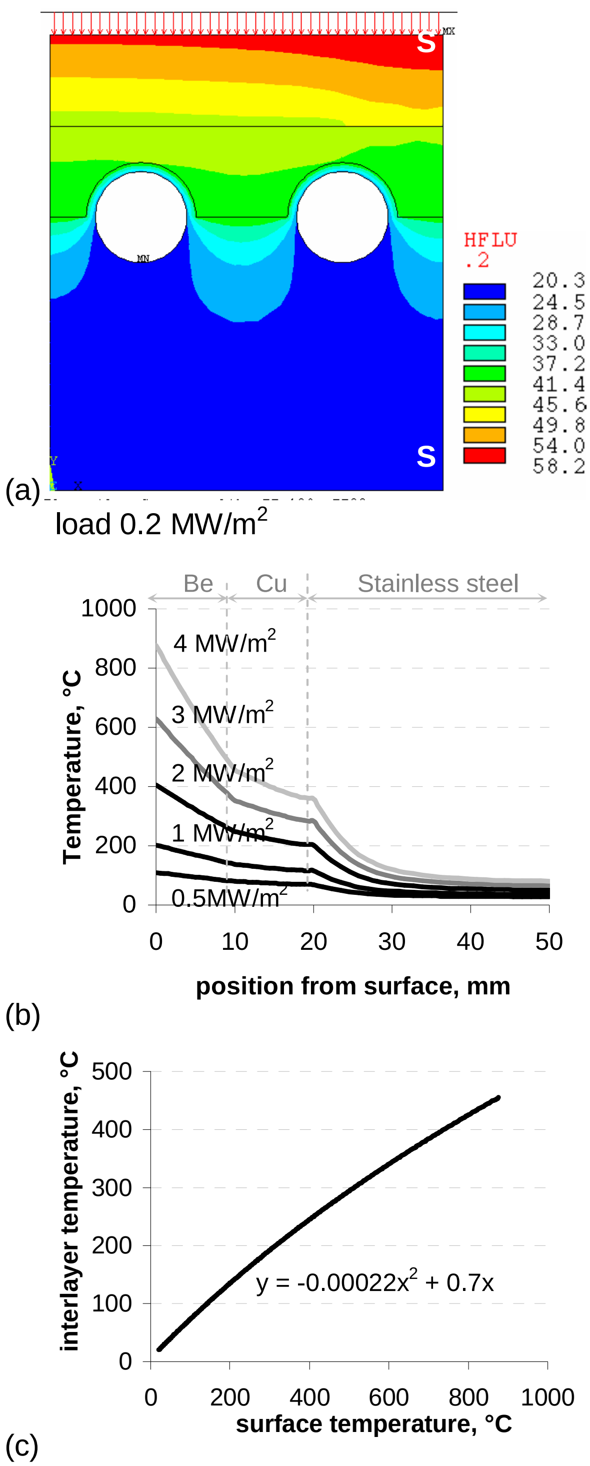

Figure 5.3 - 8. FEM calculation of (a) temperature fields in the cross section, (b) temperature profiles through the center of the module, (c) dependence of temperature at the joining layer on the surface temperature

of Be to copper alloys is complicated because beryllium forms brittle beryllides with most elements including copper (at temperatures as low as 350°C) [79]. The beryllium alloy S-65C itself contains up to 0.1 % Cu. The direct interaction of Be with Cu is very high in comparison with other metals. The reactivity of beryllium with an electrodeposited copper coating was studied by Odegard et al. [80] at temperatures of 350, 450 and 550°C using optical and electron microscopy, quantitative microprobe analysis, and mechanical testing. The reaction layer consisted of two phases (BeCu and Be_2Cu) and formed at all temperatures evaluated. The rate of interaction increases significantly with temperature increase. The Be_2Cu phase was not observed at very short reaction times at the lowest temperature of 350°C. One of the methods to protect Be/Cu joints is the use of interlayer materials such as Ti, Ni, Al, Si, Zn, Ge [81, 82].

In the experiment the surface temperatures of the beryllium armour are measured by IR camera or pyrometer. On the basis of these results the joint temperatures can be calculated. This was done by FEM calculation of temperature fields of a module with geometry similar to the module FT 111.

In Figure 5.3 - 8a temperature fields in the module cross section at power density of 0.2 MW/m^2 calculated by FEM are shown. Figure 5.3 - 8b demonstrates temperature profiles at different loads along the symmetry axis S-S (55 mm from left side) from the surface into the module. Three temperature zones could be clearly picked out. These zones corresponded to the different materials in the structure of the module: beryllium, Cu alloy and steel.

If the temperature distributions in the cross section of the module are known, the temperature on the interface between beryllium armour and copper heat sink can be predicted from the surface temperature. The correlation between the interface temperature and the surface temperature at loads of 0.5 up to 4 MW/m^2 in the steady state condition is presented in Figure 5.3 - 8c. The dependence of temperature at the interface between the beryllium armour and copper plate on the surface temperature is characterized by a polynomial $y = 0.00022x^2 + 0.7x$.

According to this dependence temperature fields in the joining layer were re-counted from surface temperature measured during thermal fatigue experiment (Figure 5.3 - 9). The distribution of temperature fields in joining layer replicates the temperature fields on the beryllium surface, but joint temperatures are much lower. For example, by 65th cycle temperature of the hottest part of the surface reached 800°C what corresponds to a temperature of 450°C at the joint.

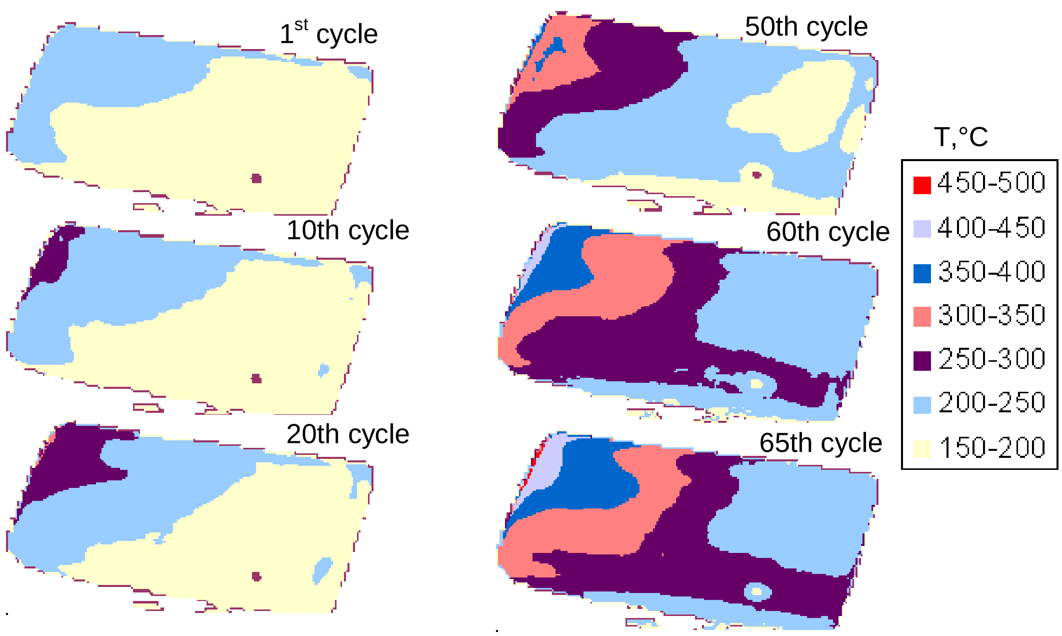

Figure 5.3 - 9. Temperature fields on the joining interface under tile 1 of the beryllium module FT 111 during 65 cycles of thermal fatigue loading at absorbed power density of 1.5 MW/m^2

The expansion of the overheated zone along the line 1-1 (infrared image in Figure 5.3 - 10) during 65 cycles of thermal fatigue loading at 1.5 MW/m^2 is shown in Figure 5.3 - 10c. Above it was pointed out that intermetallic phases can be formed at temperature above 350°C. Therefore, this value was defined as starting temperature of joint degradation. It is necessary to note that mechanism responsible for the accelerated degradation could not be inequivocally assigned, because all the above mentioned possible degradation processes (pre-existing defects; thermal stresses; brittle phases formation) do take place.

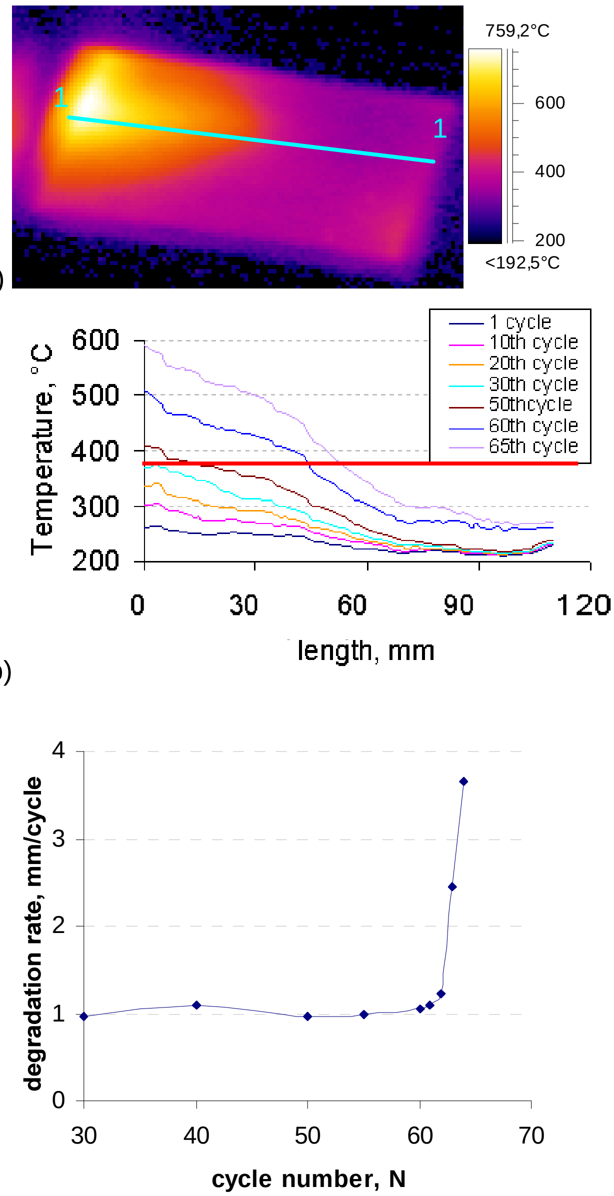

(a)

(b)

(c)

Figure 5.3 - 10. Thermal fatigue test at absorbed power density of 1.5 MW/m^2 during 65 cycles: (a) infrared image of the tile1, (b) temperature profile at Be-Cu interface, (c) expansion velocity of overheated zone

The temperature of joining interface reached 350°C (red line) after about 30 cycles of loading (Figure 5.3 - 10b). During the next 20 cycles (from 30th to 50th) the size of the zone with temperatures higher than 350°C expanded from 15 mm to 35 mm. This allows to estimate the velocity of zone expansion as (35-15) mm/(50-30)cycles=1 mm/cycle. In a similar way the expansion velocity of a zone with temperatures higher than 350°C was determined during the full thermal fatigue test. Figure 5.3 - 10c shows the diagram of expansion velocity for this zone. It is obvious that during the first 60 cycles the zone expanded with a constant velocity about 1 mm/cycle. After 60 cycles the expansion velocity of the zone sharply increased, what resulted in failure of the module. Thus, during electron beam loading, the zone of joint with temperatures higher than 350°C expanded from 0 (at the 1st cycle) up to about 60 mm (at the 65th cycle) along the line 1-1, what is around half of the tile length.

So, after 65 cycles of loading the conditions for joint degradation (interface temperature higher than 350°C) were developed in a large area and as a result the armour detached.

5.3.4. Conclusions:

The Chapter discussed the special features of the heat removal degradation during thermal fatigue loading of the modules with beryllium armour produced with different joining techniques in the electron beam facility JUDITH:

1. Two types of heat transfer degradation caused by high heat flux loading were discussed. The heat transfer degradation is in general associated with the catastrophic failure of the joint. This failure can occur
    a. during stationary loading
    b. during thermal cycling

2. Heat transfer degradation was not observed in loadings with an absorbed power density below 1.5 MW/m^2.

3. The correlation between temperature fields at the surface and in the joining interface was analyzed numerically. This method allows to calculate temperatures in the interface for analysis of overheating of the braze materials and to quantify the growth rate of overheated zone between armour and heat sink.

5.4. Analysis of neutron loaded modules

5.4.1. Irradiation campaign PARIDE 3 and PARIDE 4

This chapter discusses the impact of the neutron radiation on the thermo-physical properties of materials, used for plasma facing components of divertor in plasma vessel of ITER. It proved to be necessary to conduct this kind of investigation due to the fact, that in the real working conditions the materials will be irradiated by neutron up to 1 dpa [6].

In order to study the degradation effects of plasma facing components and materials caused by the fast neutrons, samples have been neutron-irradiated in the High Flux Reactor (HFR), Petten, the Netherlands (Figure 5.3 - 1a) in the framework of the so-called PARIDE program (**P**l**A**sma facing mate**RI**ials for ITER and **DE**MO).

The conditions of the first irradiation campaign were the following:

PARIDE 1 - 0.30 dpa for beryllium or carbon materials at temperature 330–390°C

PARIDE 2 - 0.35 dpa for beryllium or carbon materials at temperature 750–800°C.

In the framework of PARIDE 1 and PARIDE 2 actively cooled samples were made from CFC, or beryllium as plasma-facing materials and copper alloys as heat sink materials. Different designs (flat tile, monoblock) and joining techniques (brazing, welding) were used. CFC monoblock mock-ups produced by AMC and Ti brazing (see Chapter 2.7), show the best performance of all actively cooled mock-ups before and after neutron irradiation. A neutron-irradiated CFC flat tile mock-up produced by AMC and electron beam welding reached its heat flux limit at power densities of 10 MW/m^2 approximately. Brazed Be/Cu flat tile mock-ups fulfil the requirements of first wall applications [83].

The second irradiation campaign was performed at the target irradiation conditions for the next two irradiation programs:

PARIDE 3 - 0.2 dpa for low-Z materials and 0.1 dpa for tungsten at 200°C

PARIDE 4 - 1 dpa for low-Z materials and 0.6 dpa for tungsten at 200°C

The task of irradiation campaign PARIDE 3 and PARIDE 4 was to investigate the neutron influence on advanced armour materials W-alloys, CFC and the heat sink alloy CuCrZr. In the framework of this program non-irradiated reference samples and irradiated samples (Figure 5.3 - 1b) were tested (thermal shock testing, mechanical tests, thermal conductivity testing, metallography). Additionally, the thermal fatigue behaviour of CFC and tungsten actively cooled mock-ups produced in flat-tile and monoblock desing and beryllium mock-ups produced by flat tile techniques after irradiation were investigated. Non-irradiated modules, that were produced by the same technology, were taken as control samples. Comparison of the behavior of non-irradiated and irradiated modules under high heat loads was carried out in the electron beam facility JUDITH. Moreover, post mortem metallographic investigation of modules was done to define the possible reason of failure.

Due to the neutron flux gradient and to different nuclear heating in different areas of the rig in the reactor the irradiation conditions for the individual samples deviated more or less from the given target values [85].

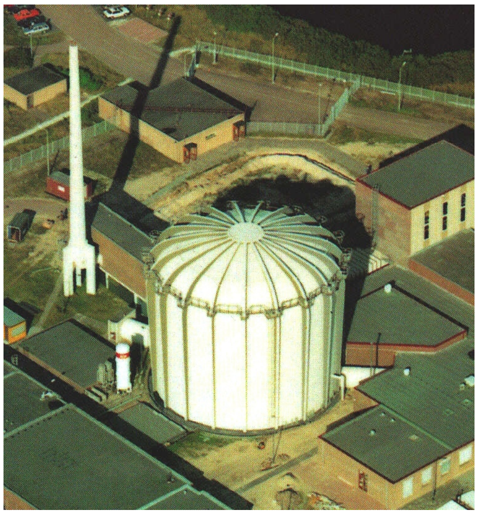

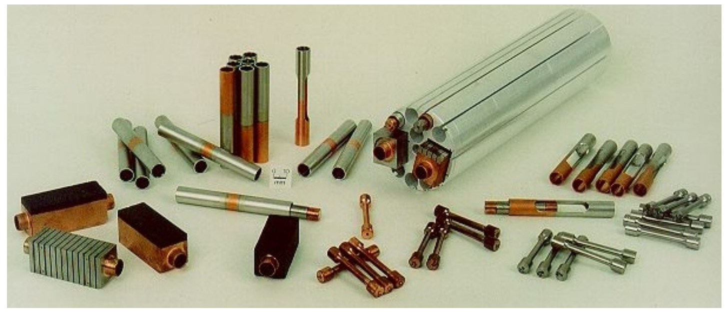

(a) (b)

Figure 5.3 - 1. (a) High Flux Reactor (HFR), Petten (the Netherlands) (b) samples irradiated in PARIDE 3 and PARIDE 4

For detailed description two types of mock-ups were choose: tungsten macrobrush and CFC flat tile module.

5.4.2. Thermal conductivity

Different thermophysical characteristics were determined for investigation of irradiation impact on the materials properties. The temperature dependences of thermal diffusivity $\alpha(T)$ [cm/s^2] and heat capacity Cp(T) [J/gK] were measured [84, 85]. Thermal diffusivities were measured with a laser flash apparatus [86]. During the measurement a small disc shaped sample was loaded by a short laser pulse, and the resulting temperature increase on the back side of the sample was measured. From the slope of the temperature vs. time curve, thermal diffusivity was calculated [85]. Heat capacities were measured by means of Netzsch differential scanning calorimeter DSC 404-C Pegasus. In this apparatus, a small sample is compared with a reference sample. From the heat flux and from the sample, thermo-physical parameters (transition enthalpies, transition temperature, heat capacities) can be deducted [85].

The thermal conductivity $\lambda(T)$ [W/cm K] of the investigated materials tungsten alloy W-1% La_2O_3 and silicon doped carbon fiber composite NS 31 was determined according to the method described by W. Schenk and D. Pitzer [86] from thermal diffusivity $\alpha(T)$, density $\rho(T)$ and heat capacity $c_p(T)$. Thermal conductivity was calculated by the formula:

$$\lambda(T) = \alpha(T) \bullet \rho(T) \bullet c_P(T) \qquad (5.3 - 1)$$

For this temperature dependent densities of tungsten alloy W-1% La_2O_3 were taken from the ITER Materials Data Base [87].

Figure 5.3 - 2 and Figure 5.3 - 3 show thermal conductivities of tungsten alloy W-1% La_2O_3 and Si-doped CFC NS 31 at different neutron doses: tungsten alloy W-1% La_2O_3 at dose 0.1 dpa at 200°C (PARIDE 3) and 0.6 dpa at 200°C (PARIDE 4) and NS31 at dose 0.2 dpa at 200°C (PARIDE 3) and 1 dpa at 200°C (PARIDE 4). Non-irradiated samples of the same materials have been tested as a reference.

In Figure 5.3 - 2 it is shown that the thermal conductivity for W-1% La_2O_3 alloy decreases monotonously with increasing temperature both for a reference non-irradiated sample and for irradiated samples. But after irradiation the thermal conductivity of the material decreases; moreover, the higher the irradiation dose, the lower the thermal conductivity value. At low temperatures (up to 800°C) the reduction of the thermal conductivity of W-1% La_2O_3 after irradiation is 22% (0.1 dpa) and 28% (0.6 dpa) respectively in comparison with non-irradiated samples. At temperatures ≥1000°C the thermal conductivity reaches the same level of about 1.1 W/cm K. Thus, on the whole the tendency of thermal conductivity of irradiated samples is similar to the reference sample.

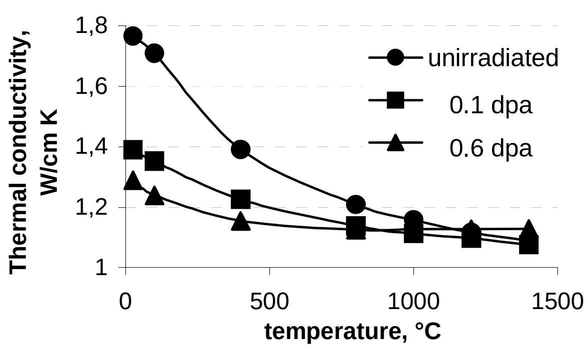

Figure 5.3 - 2.Thermal conductivity of W-1%La_2O_3 alloy for unirradiated and irradiated materials, W/ cm K

The effect of thermal conductivity decrease after neutron irradiation is caused by a reduction of the thermal diffusivity of W-1%La_2O_3 samples measured as described above. At high testing temperatures (above 800°C) this reduction depends neither on the irradiation dose nor on the irradiation temperatures. But at lower testing temperatures the effect of thermal diffusivity degradation increases with the neutron dose. The heat capacity of W-1%La_2O_3 alloy depends on the irradiation dose and irradiation temperature. It is slightly increased after irradiation. But for the high irradiation temperature this effect is reduced and the heat capacities are similar to the ones of the non-irradiated material [85].

Due to anisotropy of carbon fiber composites (see Chapter 2.4.1) thermal diffusivities of NS31 were defined in three directions. Results of thermal conductivity calculations are shown in Figure 5.3 - 3. In a module the CFC material is orientated in such a way that during the loading the heat is transferred in the direction with the highest heat transfer properties (pitch fiber direction).

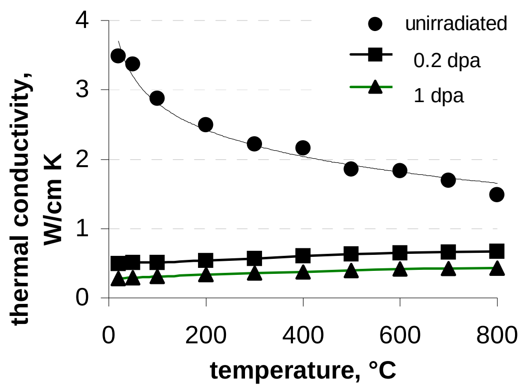

(a) pitch fiber direction

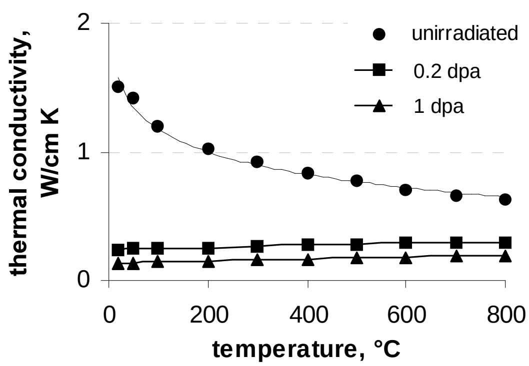

(b) PAN fiber direction

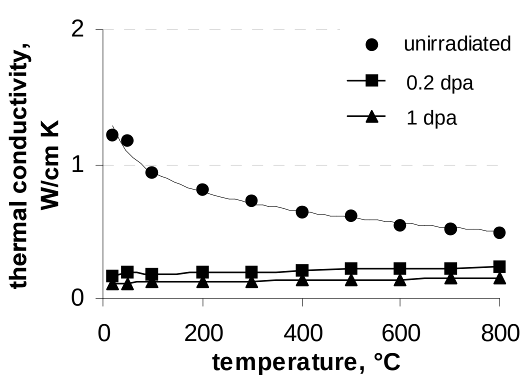

(c) needling direction

Figure 5.3 - 3. Thermal conductivity of NS31 before and after irradiation in different directions

Thermal conductivity of non-irradiated CFC NS31 decreases also monotonously with increasment of temperature.

In contrast to W-1%La_2O_3 samples the thermal conductivities of NS31 reduce greatly (by a factor of about 6-7). This reduction is mainly due to the degradation of the thermal diffusivity, and it increases with neutron dose [84]. Moreover, the character of the dependence of thermal conductivity on the temperature is changing. The thermal conductivity of irradiated samples increases with rise of temperature. Rise of the thermal conductivity was about 25 and 33% in direction y at doses 0.2 dpa and 1 dpa by temperature increasing from room temperature to 800°C, respectively. Comparison of sample orientations shows a lower thermal conductivity for PAN-fiber- and needling- compared to pitch-fiber-direction. The difference between samples orientated in PAN-fiber- and needling-directions is small in the non-irradiated stage, both for 0.2 and 1 dpa, respectively [84].

Thus, during measurements of thermo-physical properties it was shown that the tungsten alloy W-1%La_2O_3 and NS31 are characterized by a decrease of thermal conductivity after neutron irradiation.

It is well known, that the thermal conductivity of graphite is dominated by phonon transport and is therefore greatly affected by lattice defects. The extent of the thermal conductivity reduction is controlled by the efficiency of creating and annealing lattice defects and its, therefore, related to irradiation temperature. Several types of irradiation-induced defects have been identified in graphite. For irradiation temperatures lower than 650 °C, simple point defects in the form of vacancies or interstitials, along with small interstitial clusters, are the predominant defects. Moreover, at an irradiation temperature near 150°C the defect that dominates the thermal resistance is the lattice vacancy [88].

The irradiated campaign was carried out for W- and CFC-modules to investigate the neutron irradiation impact on the heat transfer degradation during thermal fatigue loadings of plasma facing components.

5.4.3. Heat transfer in tungsten macrobrush modules

Previous investigations with non-irradiated modules showed good performance of tungsten macrobrush components during thermal fatigue loadings at high power densities. For example, M. Rödig et al. reported that a tungsten macrobrush mock-up did not show any indication of failure up to the maximum test condition of 13.7 MW/m^2 (absorbed power density) [89]. A macrobrush was overheated and tile-detachment occurred during thermal fatigue tests after 500 cycles at 11 MW/m^2 plus 400 cycles at 15 MW/m^2 [90].

Peculiarities of heat removal and the thermal fatigue performance of macrobrush modules after neutron irradiation investigated in the framework of PARIDE campaign to be discussed here.

W macrobrush modules (see Figure A5.4 -1 in Appendix) were produced by industry. The chamfered 4 x 4 mm^2 W-1%La_2O_3 rods were coated with OFHC-Cu and were electron beam brazed to the CuCrZr heat sink (Figure 5.3 - 4.).

The tungsten module FT 83-3 was tested for reference before irradiation [91]. The module tungsten FT 83-8 was irradiated at a dose of 0.1 dpa at 200°C (PARIDE 3). The tungsten module FT 83-5 was irradiated at a dose of 0.6 dpa at 200°C (PARIDE 4).

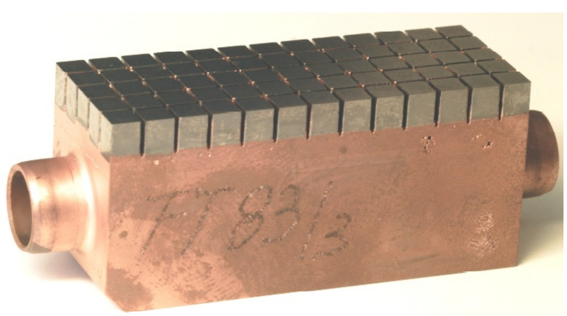

Figure 5.3 - 4. W macrobrush mock-up FT 83-3

In Table A5.4-1 (Appendix) the loading conditions and testing results of the modules FT 83-3, -5, -8 in electron beam facility are described. Screening tests at absorbed power densities of 1-15 MW/m^2 were successfully applied for all modules.

After screening, 1000 thermal fatigue cycles were carried out. The absorbed power density of the electron beam was varied in interval from 8 to 13 MW/m^2. The module

FT 83-8 (0.1 dpa) showed first failure during thermal fatigue test at absorbed power density of 10 MW/m^2. The modules FT 83-3 (non-irradiated) and FT 83-5 (0.6 dpa) were tested at higher heat loads of about 13 MW/m^2.

Moreover, numerical modelling of the heating process under high heat load was carried out. Neutron irradiation impact on thermo-physical properties of W-1%La_2O_3 and CuCrZr (thermal conductivity, temperature diffusivity, specific heat) and their temperature dependence were taken into account in a numerical model. A model with similar geometry to the module FT 83 (Figure 1 in Appendix 4.3) was calculated by FEM.

Figure 5.3 - 5a shows the results of these calculations. It is obvious, that after irradiation the modules are characterized by higher surface temperatures at steady state. The difference between surface temperatures of irradiated and non-irradiated modules increases with the increase of the neutron dose. But this difference is not high and achieves 60°C and 80°C for neutron doses of 0.1 dpa and 0.6 dpa, respectively, at a power density of 15 MW/m^2.

Figure 5.3 - 5b demonstrates the results of screening tests of the modules FT 83-3 (non-irradiated), FT 84-5 (0.6 dpa), FT 83-8 (0.1 dpa) in electron beam facility JUDITH. The temperature was measured in the center of the module as shown in the infrared image by a pyrometer (Figure 5.3 - 5). Experimental data clearly demonstrate that the difference of the surface temperature at the same absorbed power density is small for different modules. Slight scattering of experimental temperatures for different modules at the same load can be also explained by changes of the surface emissivity due to neutron irradiation, that modifies the surface of the materials. The curve of temperature change with increasing thermal loads was calculated using FE methods and is also shown in Figure 5.3 - 5b (dotted line). This numerical calculated dependences are in good agreement with experimental data. The comparison between calculated and measured temperatures for each module is presented in Figure A5.-2 (Appendix).

Thus, it is shown that the neutron irradiation of a W-macrobrush up to 0.6 dpa does not have strong impact on the heat transfer properties and thermal fatigue performance of the modules.

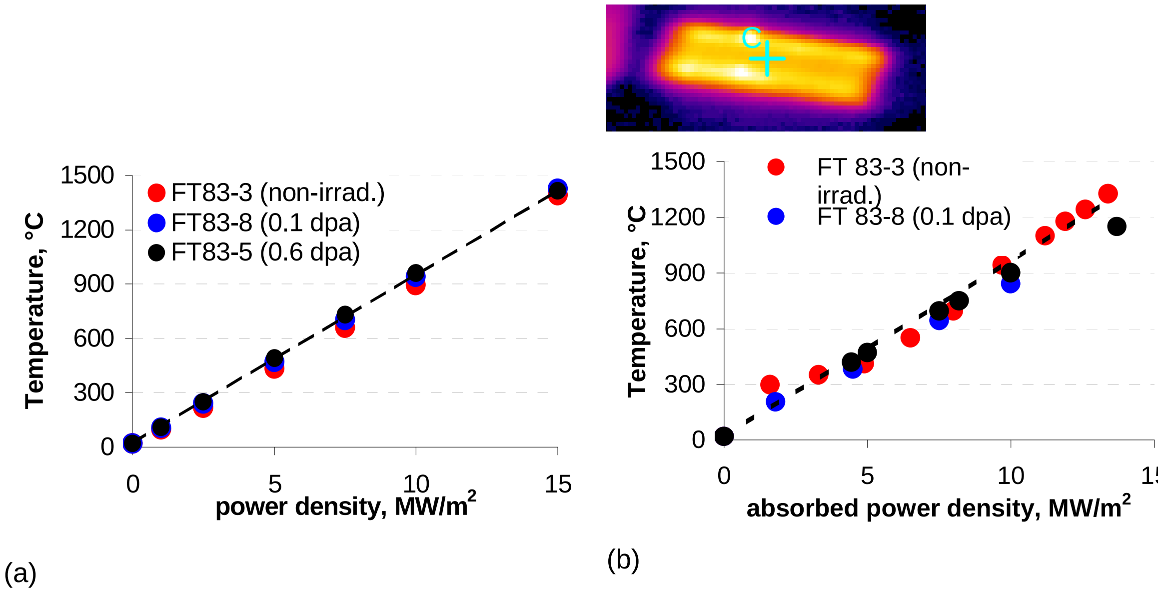

Figure 5.3 - 5. Surface temperature of the module FT 83-3 (non-irradiated), FT 84-5 (0.6 dpa), FT 83-8 (0.1 dpa) during screening tests according (a) FEM calculation and (b) experiments

The module FT 83-8 irradiated at 0.1 dpa during thermal fatigue cycling at 10 MW/m^2 showed degradation of heat transfer resulting in significant surface overheating. The temperature evolution on the surface to be discussed here.

Figure 5.3 - 1 shows the surface temperature in different points during 1000 cycles for the module FT 83-8. There is the clear tendency that the surface temperature increases during the thermal fatigue test. The temperature rise reached about 180°C during the cycling. This overheating was not high and was comparable with the temperature rise for another module

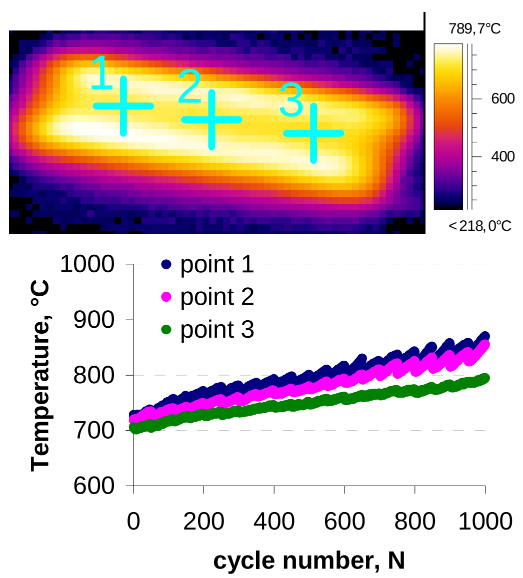

Figure 5.3 - 1. Thermal fatigue tests of the module FT 83-8 (0.1 dpa) at 10 MW/m^2

FT 83-5 (0.6 dpa) at 10 MW/m^2 (Figure A5.4-7 in Appendix) but simultaneously in infrared images significant overheating was observed in the edge areas.

In Figure 5.3 - 2 the temperature increase during 1000 cycles of the same thermal fatigue test along the lines A and B is presented. During the test, the module was overheated from both edge sides. The temperature increase on the edges reached about 400°C, but in the center of the module (where the cooling tube is located) temperature increased for only 100°C. Figure 5.3 - 2 shows the surface temperature fields during cycling. There is a slight increase of temperature towards the end of the experiment. This overheating can not be due to only the cooling condition (the heat transfer are worst at the edge in this geometry), because for the reference module FT 83-3 (Figure A5.4 - 5) the overheating of edge areas was not observed. Probably, in this case the reason of overheating is the reduction of the heat transfer properties of the joint due to neutron irradiation. The overheating of the edges was so significant that the module was damaged and thermal fatigue test had to be terminated.

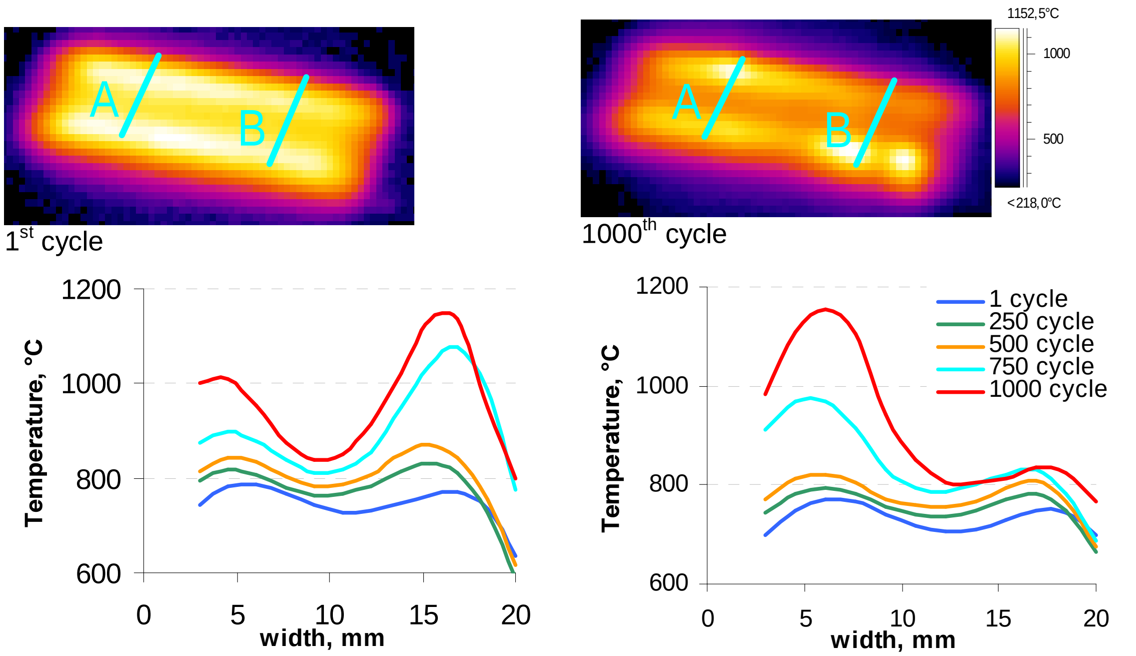

(a) (b)

Figure 5.3 - 2. Temperature evolution on the surface of the module FT 83-8 during thermal fatigue test at 10 MW/m^2 (a) along line A (b) along line B

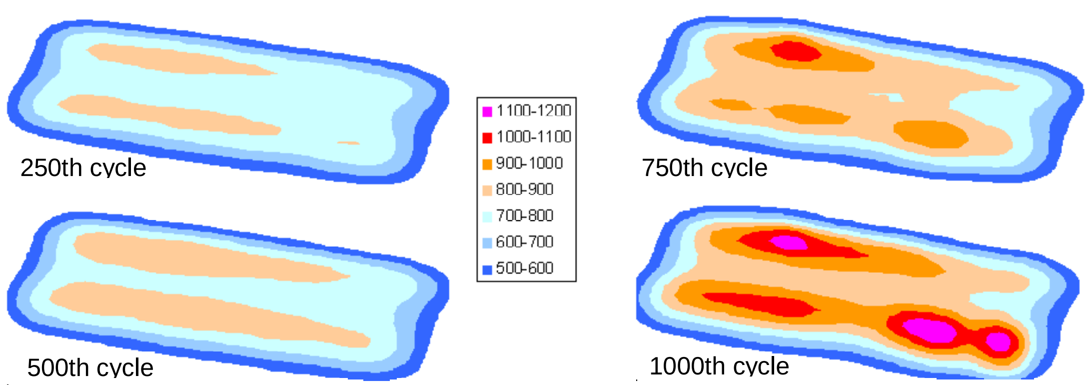

Figure 5.3 - 3. Temperature fields of the module FT 83-8 during thermal fatigue test at 10 MW/m^2

The degradation of heat removal and thermal fatigue performance of another W-1%La_2O_3 - modules of the FT 83 - type is in detailed described in Appendix (Figures A5.4- 4 – A5.4-9). Thus, in this chapter it was possible to prove that the irradiation of W-1%La_2O_3 modules at doses up to 0.6 dpa results in small surface temperature change during electron beam loading. But during thermal fatigue cycling areas with local overheating and surface temperature increase were observed.

5.4.4. Heat transfer in CFC flat tile modules

To study the special features of the heat transfer degradation under electron beam loads CFC flat tile mock-ups were investigated. Siliconized NS31 (~8% Si) was coated by Active Metal Casting (AMC) and electron beam welded to the CuCrZr heat sink. The geometry and size of these modules are similar to the modules FT 109 (Figure 1 in Appendix 5.1). The sample FT 85-9 was used for reference testing under electron beam in JUDITH to investigate the thermal behaviour of a non-irradiated component. The sample FT 85-11 was irradiated in the HFR Petten at 0.2 dpa at 200°C, FT 85-12 at 1 dpa at 200°C. The loading history and results are described in Table A5.4-2 (Appendix). The loadings were twofold: (1) screening tests at absorbed power densities of 1÷23.5 MW/m^2 and (2) thermal fatigue tests at 10 ÷ 20 MW/m^2.

Figure 5.3 - 14 shows the non-irradiated module FT 85-9 before and after loading in the electron beam facility. In the dark area D on the tile 1 that was formed during electron beam loading a clear erosion of the CFC armour was detected. Area D corresponds to the overheated area observed in an infrared image during heat loads (Figure A5.4-14 in Appendix).

Similar effects (oxidation of heat sink and joining interlayer, darkening and erosion of CFC surface) were observed for the neutron irradiated modules FT 85-11 (0.2 dpa) and FT 85-12 (1 dpa) (Figure A5.4-10 and Figure A5.4-11 in Appendix).

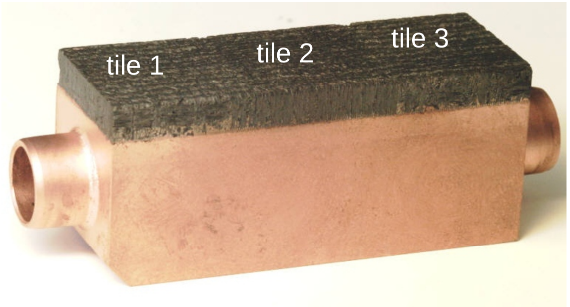

(a) before

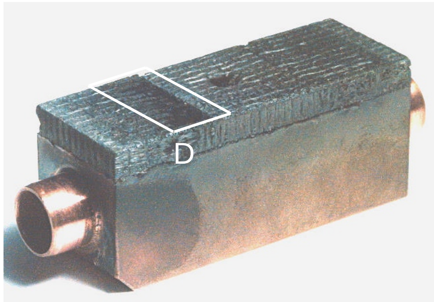

(b) after

Figure 5.3 - 14. Surface state of the module FT 85-9

The analysis of the heating conditions of a CFC surface was conducted with FEM. A numerical model has a similar geometry as the modules FT 85 (Figure A5.4-1 in Appendix). The calculations were applied for the modules with thermal-physical temperature dependent properties of the following armour materials: non-irradiated NS31, irradiated NS31 at 0.2 dpa and at 1 dpa. Additionally, the property changes of a heat sink alloy CuCrZr were included.

Figure 5.3 - 15 presents the calculated surface temperature at different power densities for the modules irradiated at 0.2 and 1 dpa and non-irradiated components. These theoretically calculated curves demonstrate that steady state temperatures on the surface for the modules with irradiated materials are much higher than those for a non-irradiated sample already at low power densities. For example, at 5 MW/m^2 surface temperature for a non-irradiated module reaches about 300°C, for a module irradiated at 0.2 dpa about 700°C and for 1 dpa about 950°C. At heat loads of 20 MW/m^2 these surface temperatures reach around 1500°C, 2300°C and 2800°C, accordingly. Thus, according to FEM calculations, a module irradiated at 1 dpa will be heated during electron beam loads up to a temperature two times higher than a non-irradiated module will.

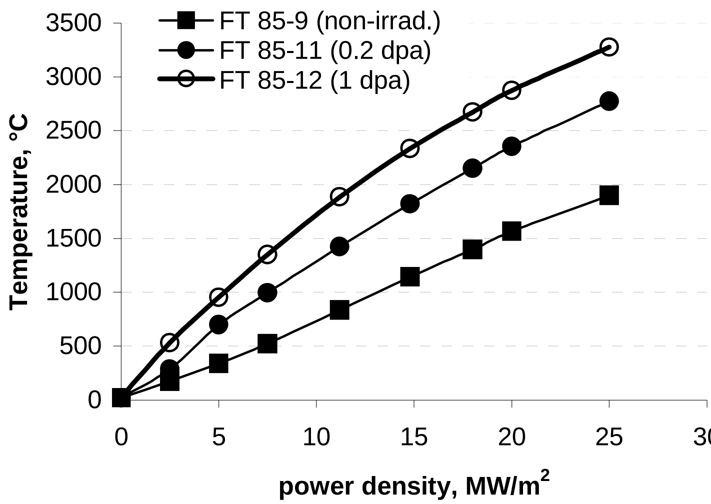

Figure 5.3 - 15. FEM calculated surface temperatures of the modules with CFC armour

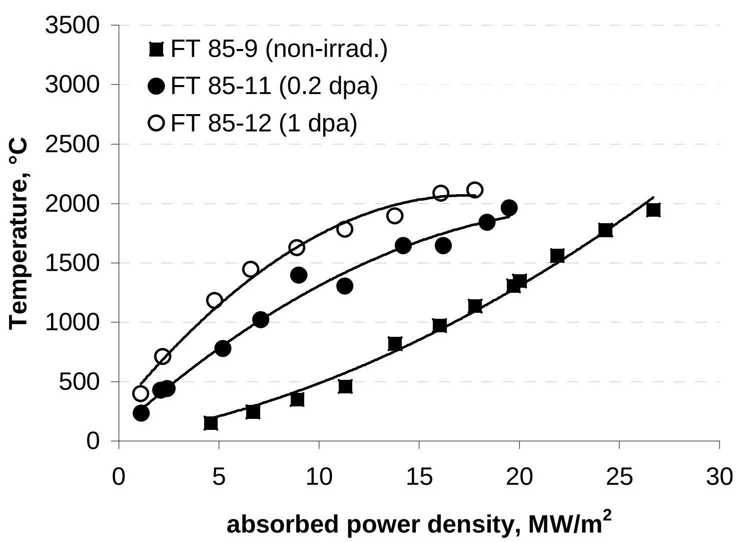

Figure 5.3 - 16. Experimental surface temperature of the modules with CFC armour during screening tests

Figure 5.3 - 16 shows the surface temperature increase for the modules FT 85-9, -11, -12 with increase absorbed power density during screening tests. Qualitative numerical calculations (Figure 5.3 - 15) strongly correspond to these experimental results in all cases. But the difference of experimentally measured temperatures is clearly observed at high heat loads, when the surface temperatures exceed 2000°C. It is known that at temperature higher than 2000°C CFC material starts to sublimate [92]. This effect was not included in the numerical model by FEM calculations. Moreover, annealing of the CFC materials influences significantly the change of the surface temperature under high heat loads. This impact results in an increase of the thermal conductivity of armour material and therefore, in an increase of the heat flux into the module. The applied FEM model does not take into account the change of thermal properties of CFC during loading. The comparison of calculated and measured temperatures for each module is presented in Figure A5.4-3 (Appendix).

The heat removal in an irradiated CFC mock-up during thermal fatigue loadings will be discussed below using as an example the module FT 85-11. It was irradiated at 0.2 dpa at 200°C. High heat flux testing was applied in electron beam facility JUDITH as described in Table A5.4-2 in Appendix. The module sustained successfully three thermal fatigue tests during each 1000 cycle: at 11.8, 15.4 and 19.5 MW/m^2, respectively. The temperature changes in the center of each tile during thermal fatigue cycling are shown in Figure 5.3 - 17. Important behavior feature of the modules after irradiation is the surface temperature decrease during cycling. This effect was clearly observed at thermal fatigue tests at 11.8 and 19.5 MW/m^2. The total temperature decrease during 1000 cycles reached 100°C in both cases.

This effect can be explained in the following way: In Chapter 5.4.2 it was shown that thermal conductivity of CFC had been reduced during neutron irradiation due to

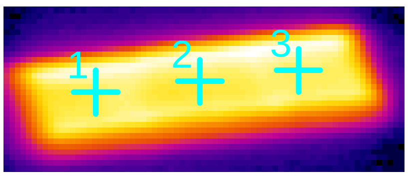

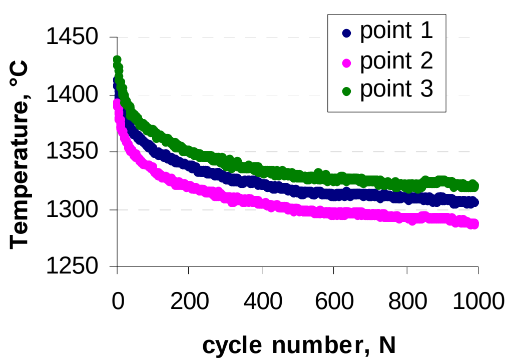

(a) load of 11.8 MW/m^2

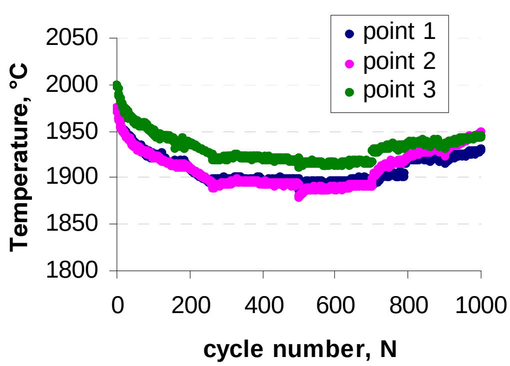

(b) load of 19.5 MW/m^2

Figure 5.3 - 17. Thermal fatigue tests at different absorbed power densities of the module FT 85-11 (0.2 dpa)

vacancy formation by neutron interaction with the lattice. Then during electron beam heating the CFC material is annealed and the vacancy number decreases. It results in an increase of thermal conductivity of CFC and therefore in a slight decrease of surface temperature.
At 19.5 MW/m^2 after about 700 cycles the temperature started to increase slightly. This is an indication for an overheating of the surface due to a reduction of the heat transfer from the surface to the cooling tube and a degradation of the heat transfer properties of the module.
Figure 5.3 - 18 demonstrates the evolution of the surface temperature of the module FT 85-11 during the thermal cycling at 19.5 MW/m^2. The temperature is the same on whole the surface area. Slight overheating (about 100°C) was detected in internal edges of the tiles. Most probably that the degradation of heat transfer properties of the module initially started and developed in these overheated areas.

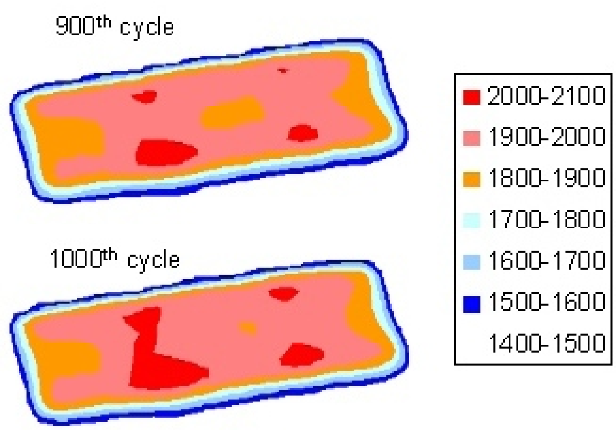

Figure 5.3 - 18. Temperature fields of the module FT 85-11 (0.2 dpa) during thermal fatigue test of the at 19.5 MW/m^2

The degradation of heat removal and thermal fatigue performance of another CFC -modules of the FT 85 – type is in detailed described in Appendix (Figures A5.4- 10 – A5.4-16).

5.4.5. Conclusion

The following conclusions can be drawn concerning the degradation of neutron irradiated components:

1. Neutron irradiation results in the reduction of thermophysical characteristics (thermal conductivity and thermal diffusivity) for both tungsten alloys (such as W-1%La_2O_3) and carbon fiber composites (e.g. NS31). Thermal conductivity of NS31 after irradiation at 1 dpa at room temperature was reduced by factor 6. Non-irradiated CFC-material shows a strong decrease in thermal conductivity with temperature increase; however, the thermal conductivity of irradiated samples increases slightly (25-33%) from RT to 800°C. For W-1% La_2O_3 the thermal conductivity at room temperatures has reduced after irradiation by 22% (0.1 dpa) and 28% (0.6 dpa), respectively in comparison with non-irradiated samples. At temperatures ≥1000°C thermal conductivities of non-irradiated and irradiated samples reach the same level.
2. A noticeable surface temperature decrease during heat loading was observed for irradiated CFC flat tile modules. It occurred due to the annealing of the carbon-based armour material. W-1%La_2O_3 modules irradiated at doses $\leq$ 0.6 dpa showed only insignificant surface temperature changes during electron beam loading compared to the non-irradiated module. Local overheated areas were determined for both tungsten macrobrush and CFC flat tile mock-ups.
3. Metallographic analyses showed different possible failure modes in the joint areas of the components. For CFC modules cracks typically developed at the interface between Ti/Cu coated CFC tiles and the CuCrZr heat sink. For W-1%La_2O_3 modules cracks were found in the OFHC interlayer close to CuCrZr heat sink. Both types of cracks are oriented perpendicular to the direction of the heat flux in the divertor modules; hence, they represent a thermal barrier, that results in increased surface temperature of the modules.

Chapter 6. Summary

On the conceptual and technological levels scientists are nowadays challenged with energy supply through controlled thermonuclear synthesis. This requires the development of specific materials and components able to sustain and remove extremely high heat loads. Therefore, the important task is to investigate the heat transfer in the developed components and materials and to study their behavior under the high heat fluxes and neutron loads. The task of great importance is also the quality control of the components. For this reason non-destructive control methods need to be adapted.

The presented research is focussed on the development of detection methods of the areas with degraded heat transfer in the first wall and divertor components designed for ITER or other next step fusion devices.

Infrared thermography was chosen as a relatively cheap and fast, easy to handle non-destructive method for the detection of defects resulting from manufacturing procedure. A special facility IRINA was configured. This facility is based on the principle of infrared thermography. It consists of a heating system, an IR camera and several control units. The water flow through the component to be tested is supplied by two water circuits with well defined and controlled temperatures (95°C and 20°C) and flow rates.

The electron beam facility JUDITH was applied to investigate the degradation of the heat transfer from the plasma facing surface to the heat sink under fusion specific thermal loads up to approximately 20 MW/m^2. This method also allows to study the evolution of structural imperfections caused by thermal fatigue. In addition, neutron induced degradations were analysed.

Finite elements were applied to simulate the heat transfers within the modules.

Investigation of heat transfer in the plasma facing components using infrared inspection methods (IRINA)

Several actively cooled plasma facing components were investigated in order to study the heat transfer peculiarities of different component configurations: monoblock and flat tile geometry; different combinations of armour and heat sink materials; geometric effects such as components size, and arrangement of the cooling tubes. It was found that the component configuration limits the application of infrared observation of heat transfer differences caused by structural defects.

Furthermore, the influence of the surface structure on the infrared image was investigated for different materials. A method was proposed to correct the local emissivity variations connected with the material morphology. Using this method to eliminate the impact of surface conditions on the temperature the differences in heat transfer caused by structural defects can be analysed.

The method of infrared heat transfer inspection was elaborated and criteria to judge the modules quality based on comparative analyses of temperature gradients on the modules surface during heating were worked out. Further, the optimal parameters for the detection of areas with lower heat transfer properties were defined.

The correlation between defect size and surface temperature deviation has been investigated in IRINA and a linear correlation between the variables was found.

On different plasma facing components the suggested methodology has the potential to define local defect areas which were in general located at the interface between the armour material and the heat sink. To verify the presence of the damaged zones in the structure, which disturb the heat flow, CFC monoblock modules were investigated additionally in the electron beam facility JUDITH. The investigations have unequivocally confirmed the existence of the defect areas.

However, infrared inspection method using the IRINA test facility is limited to the detection of pre-existing areas with reduced heat transfer in a plasma facing component.

Investigation of areas with degraded heat transfer using intense electron beams (JUDITH)

Different types of plasma facing components were subjected to fusion-specific heat fluxes in the electron beam facility JUDITH with the aim to detect local variations in the heat transfer due to pre-existing defects or due to thermal fatigue of the materials. The flat tile modules varied according to (1) armour materials – CFCs, beryllium, tungsten, and (2) joining techniques.

It has been demonstrated that the heat transfer degradation during thermal fatigue loading of different types of modules is directly correlated with the surface temperature behavior.

Intense cyclic thermal loads applied to CFC flat tile modules result in an irreversible thermal fatigue damage of the module; the resulting surface temperature of the components changed in two steps: firstly, the surface temperature increases gradually with cycle number. This process is associated with the accumulation of microcracks in the joint due to high thermal stresses caused by significant thermal gradients from the module surface to the cooling tube and due to the mismatch of the thermal expansion coefficient of the plasma facing material and the heat sink. Secondly, thermal cycling leads to a rapid temperature increase (during a few cycles). Cracks are formed at the interface between CFC armour and OFHC joining material which finally results in the catastrophic damage of the joint and the module failed (detachment of the armour).

Beryllium flat tile modules in general, did not shown the heat transfer reduction during thermal fatigue loading. The steady state temperature remained almost constant during the cyclic loading until complete failure occurred within one single additional cycle. Continuous surface temperature increase and expansion of the overheated zone (1 mm pro cycle) during thermal cycling was observed only for one module. It should be noted that failure of the beryllium armour tiles occurred at absorbed power densities above 1.5 MW/m^2. The reduction of the heat transfer in Be-Cu-joints indicates the evolution of different damage processes: growth of pre-existing defects as a result of thermal fatigue loading; thermal stresses causing crack formation within the joint; formation and growth of beryllium intermetallic phases at the interface during the high temperature regime.

Additionally, the influence of neutron irradiation on the heat transfer degradation has been investigated.

For tungsten macrobrush modules a remarkable neutron inducted heat transfer degradation during screening tests on irradiated components was not indicated. However, during a subsequent thermal fatigue exposure to 1000 cycles at an absorbed power density of 10-13 MW/m^2 degradation of the heat transfer was detected in macrobrush modules.

A significant surface temperature rise during screening tests was detected for neutron irradiated CFC flat tile modules. Temperature increase was caused by degradation of the thermophysical characteristics (thermal diffusivity) of the CFC armour material induced by neutron irradiation. The thermal conductivity of C-based material decreased by a factor 6 at room temperature, whereas the decrease of the thermal conductivity of tungsten material decreased was only 30% at the same temperature.

In contrast to the W-modules a remarkable temperature decrease during thermal fatigue loading was observed at high temperatures (i.e. for $T \geq 1000°C$) on the surface of neutron irradiated CFC flat tile modules. The heat transfer improved due to annealing effects of lattice vacancies in the CFC material.

The metallographic analysis demonstrated that in all cases the damage of a module occurred in the joint interface between heat sink and plasma facing material, however, the reasons and the nature of the damage depend on the specificity of the material. For instance, detachment of CFCs tiles occurred due to the high thermal stresses on the boundary layer of armour and heat sink. The detachment of beryllium tiles occurred due to cracks developing under thermal stresses and the formation of brittle intermetallic phases within the joints.

Using finite element methods it was shown that defect areas occurring on the joint between the plasma facing material and the heat sink material can be simulated in terms of areas with lower thermal conductivity of the joining material. Temperature distributions under IRINA relevant condition obtained from numerical simulations strongly correlate with the experimental data. Additionally, numerical simulations of tokamak specific thermal loads on modules with reduced thermo-physical characteristics of the joining material showed adequate agreement with experiment. The same applies to the analysis of non-irradiated and irradiated high heat flux components.

Bibliography

1. H.Muilerman, H.Blonk. Towards a sustainable use of natural resources. Stichting Natuur en Milieu, 2001.
2. G. Bugliarello.The Bridge. 32 (2002).
3. R.A. Gross. Fusion energy. New York: Wiley, 1984.
4. W. Stacey. Fusion: an introduction to the physics and technology of magnetic confinement fusion. New York: Wiley, 1984.
5. Encyclopedia of applied physics. VCH, 6, 1997.
6. www.iter.org
7. Summary of the ITER Final Design Report, IAEA. ITER EDA, Documentation series, 22 July 2001.
8. W. Daenner, M. Merola, P. Lorenzetto, A. Peacock, I. Bobin-Vastra, L. Briottet, P. Bucci, D. Conchon, A. Erskine, F. Escourbiac et al. Status of fabrication development for plasma facing components in the EU, Fusion Engineering and Design, 61-62 (2002) 61-70.
9. ITER Technical Basis. G A0 FDR 1 01-07-13 R1.0
10. M. Merola, G. Federici, I. Landman, A. Loarte (EFDA), A. Zhitlukhin. EU - RF Cooperation to study the effects of ELMs on material damage for EU reference armour materials. Vortrag. Juni, 2003.
11. A.R. Raffray, J. Schlosser, M. Akiba, M. Araki, S. Chiocchio, D. Driemeyer, F. Escourbiac, S. Grigoriev, M. Merola, R. Tivey et al. Critical heat flux analysis and R&D for the design of the ITER divertor. Fusion Engineering and Design, 45, 4 (1999) 377-407.
12. G. Vieider, M. Merola, F. Anselmi, J.P.Bonal, P. Chappuis, et al. European development of prototypes for ITER high heat flux components. Fusion Engineering and Design, 49-50 (2000) 135-143.
13. Material Assessment Report, 2001.
14. D. D. Edie The effect of processing on the structure and properties of carbon fibers. Carbon, 36, 4 (1998) 345-362.
15. C. H. Wu, C. Alessandrini, P. Bonal, H. Grote, R. Moormann, M. Rödig, J. Roth, H. Werle and G. Vieider. Overview of EU CFCs development for plasma facing materials. Journal of Nuclear Materials, 258-263 (1998) 833-838.
16. G. Vieider, M. Merola, J.P. Bonal, P. Chappuis, D. Duglue et al. European development of the ITER divertor target. Fusion Engineering and Design, 46 (1999) 221–228.

17. J.P.Bonal. Thermal properties of NB31 and NS31 carbon fiber composites. CEA, Direction des Reacteures Nucleares, Departement de Mecanique et de Technologie (DMT), Report DMN/SEMI/LM2E/RT/01-003, 2001.
18. V. Barabash, M. Akiba, J.P. Bonal, G. Federici et al. Carbon fiber composites application in ITER plasma facing components. Journal of Nuclear Materials, 258-263 (1998) 149-159.
19. H. Maier, S. Kötterl, K. Krieger, R. Neu, M. Balden. Performance of tungsten coatings as plasma facing components used in ASDEX Upgrade. Journal of Nuclear Materials, 258-263 (1998) 921-926.
20. R. Neu, R. Dux, A. Geier, H. Greuner, K. Krieger et al. New results from the tungsten programme at ASDEX Upgrade. Journal of Nuclear Materials, 313–316 (2003) 116–126.
21. P. Greenfield. Engineering Applications of Beryllium. London, 1971.
22. A. Khomutov, V. Barabash, V. Chakin, V. Chernov, D. Davydov et al. Beryllium for fusion application – recent results. Journal of Nuclear Materials, 307–311 (2002) 630–637.
23. E. B. Deksnis, A. T. Peacock, H. Altmann, C. Ibbot and H. D. Falter. Beryllium plasma-facing components: JET experience. Fusion Engineering and Design, 37, 4 (1997) 515-530.
24. G. Kalinin, R. Matera. Comparative analysis of copper alloys for the heat sink of plasma facing components for ITER. Journal of Nuclear Materials, 258-263 (1998) 345-350.
25. G. Kalinin, V. Barabash, A. Cardella, J. Dietz, K. Ioki, R. Matera, R.T. Santoro and R. Tivey. Assessment and selection of materials for ITER in-vessel components. Journal of Nuclear Materials, 283-287, 1 (2000) 10-19.
26. S. Chen, T. Bao, B. Chin. Braze joints of dispersion strengthened copper. Journal of Nuclear Materials, 233-237 (1996) 902-905.
27. H. Bolt, V. Barabash, G. Federici, J. Linke, A. Loarte, J. Roth and K. Sato. Plasma facing and high heat flux materials – needs for ITER and beyond. Journal of Nuclear Materials, 307-311, 1 (2002) 43-52.
28. G. Janeschitz, T. Ando, A. Antipenkov, V. Barabash, et al. Divertor development for ITER. Fusion Engineering and Design, 39-40 (1998) 173-187.
29. V. Barabash, M. Akiba, A. Cardella, I. Mazul, B.C. Odegard Jr, L. Plöchl, R. Tivey, G. Vieider. Armour and heat sink materials joining technologies development for ITER plasma facing components. Journal of Nuclear Materials, 283-287 (2000) 1248-1252.

30. B.C. Odegard Jr., C.H.Cadden, R.D. Watson, R. Nygren. A review of the US Joining Technologies for Plasma Facing Components in the ITER Fusion Reactor. 1998, IEEE.
31. A. F. Tavassoli. Overview of advanced techniques for fabrication and testing of ITER multilayer plasma facing walls. Fusion Engineering and Design, 39-40 (1998) 189-200.
32. C.M. Ibott, H.D. Falter, P. Meurer et al., Proceedings of the 18th Symposium on Fusion Technology, Karlsruhe, Aug. 1994, 431.
33. E. Frankoni, G.C. Ceccottiand, L. Magnoli. Development of beryllium bonds for plasma-facing components. Journal of Nuclear. Materials, 191–194 (1992) 493.
34. V. Barabash, M. Akiba, A. Cardella, I. Mazul, B. C. Odegard Jr, L. Plöchl, R. Tivey and G. Vieider. Armor and heat sink materials joining technologies development for ITER plasma facing components. Journal of Nuclear Materials, 283-287, 2 (2000) 1248-1252.
35. R. Tivey, T. Ando, A. Antipenkov, V. Barabash et al. ITER divertor, design issues and research and development. Fusion Engineering and Design, 46 (1999) 207-220.
36. M. Merola, M. Akiba, V. Barabash and I. Mazul. Overview on fabrication and joining of plasma facing and high heat flux materials for ITER. Journal of nuclear Materials, 307-311 (2002) 1524-1532.
37. P. Appendino, V. Casalegno, M. Ferraris. Joining of C/C composites to copper. Fusion Engineering and Design, 66-68 (2003) 225-229.
38. M. Merola, G. Vieider, M. Bet, I. Bobin Vastra, L. Briottet, P. Chappuis et al. European achievements for ITER high heat flux components. Fusion Engineering and Design, 56-57 (2001) 173-178.
39. M. Merola, I. Bobin-Vastra, A. Cardella, M. Febvre, L. Giancarli, L. Plöchl, J. F. Salavy, A. Salito, B. Schedler and G. Vieider. Manufacturing of a full scale baffle prototype for ITER with a CFC and W plasma spray armour. Fusion Engineering and Design, 49-50 (2000) 289-294.
40. Carbon Materials for Advanced Technologies. Edited by Timothy D. Burchell. 1999.
41. V. Barabash, G. Federici, M. Roedig, L. L. Snead and C. H. Wu. Neutron irradiation effects on plasma facing materials. Journal of Nuclear Materials, 283–287 (2000) 138–146.
42. G. Kalinin, V. Barabash, S. Fabritsiev, H. Kawamura, I. Mazul, M. Ulrickson, C. Wu and S. Zinkle. ITER R&D: Vacuum Vessel and In-vessel Components: Materials Development and Test. Fusion Engineering and Design, 55, 2-3 (2001) 231-246 .
43. V. Barabash, G. Federici, R. Matera, A.R. Rafflay. Armour materials for the ITER plasma facing components. Physica Scripta, 81 (1999) 74-83.

44. V. Barabash, G. Federici, J. Linke and C. H. Wu. Material/plasma surface interaction issues following neutron damage. Journal of Nuclear Materials, 313-316 (2003) 42-51.
45. M. Merola, W. Dänner, J. Palmer, G. Vielder, C. H. Wu et al. European contribution to the development of the ITER divertor. Fusion Engineering and Design, 66-68 (2003) 211-217.
46. R. Tivey, M. Akiba, D. Driemeyer, I. Mazul, M. Merola and M. Ulrickson. ITER R&D: Vacuum Vessel and In-Vessel Components: Divertor Cassette. Fusion Engineering and Design 55 (2001) 219–229.
47. J. Schlosser, P. Chappuis, M. Chatelier, A. Durocher, D. Guilheim, M. Lipa, R. Mitteau, L. Plochl, G. Tonon and E. Tsitrone. Design, fabrication and testing of an improved high heat flux element, experience feedback on steady state plasma facing components in Tore Supra. Fusion Engineering and Design 39–40 (1998) 235–240.
48. R. Mitteau, S. Berrebi, P. Chappuis, Ph. Darses, A. Dufayet, L. Garampon, D. Guilhem, M. Lipa, V. Martin, H. Roche, Non destructive testing of actively cooled plasma facing components by means of thermal transient excitation and infrared red imaging. Fusion Technology. Proceedings of the 19th SOFT, Lisbon, 1996, pp. 443–446.
49. K. Ezato, M. Dairaku, M. Taniguchi, K. Sato and M. Akiba. Non-destructive testing of CFC monoblock divertor mock-ups. Journal of Nuclear Materials 307–311 (2002) 144–148.
50. A. Durocher, P. Chappuis, R. Mitteau, L. Moncel, Infrared non destructive test of plasma facing components, Defect detection improvement, Proceedings of the Twentieth Symposium of Fusion Technology (SOFT), Marseille, France, 1998, 121-124.
51. J.J. Cordier. Preliminary results and lessons learned from upgrading the Tore Supra actively cooled plasma facing components (CIEL project). Fusion Engineering and Design 66-68 (2003) 59-67.
52. M. Merola, P. Chappuis, F. Escourbiac, M. Grattarola, H. Jeskanen, P. Kauppinen, L. Plöchl, B. Schedler, J. Schlosser, I. Smid et al. Non-destructive testing of divertor components. Fusion Engineering and Design 61-62 (2002) 141-146.
53. R. Mitteau et al., Proceedings of the 19th SOFT, 443 (1996).
54. A. Durocher, R. Mitteau, V. Paulus, J. Schlosser, "15th World Conference on Nondestructive Testing Roma " (2000).
55. A. Kapoustina, T. Hirai, J. Linke, M. Rödig. Analysis of heat transfer properties of CFC-plasma facing components by IR-observation and high heat flux testing. To be published.

56. Taschenbuch für Heizung und Klima-Technik. Oldenbourg Verlag GmbH; München, 1995.
57. Y. Koza. Performance of metallic and carbon-based materials under the influence of intense transient energy deposition. PhD thesis, RWTH Aachen, 2004.
58. R.Duwe, W.Kühnlein, G.Pott. High heat loading tests and temperature measurements in Hot Cells. European working group “Hot laboratories and remote handling” plenary meeting 21-23 Sep. 1998.
59. M. Rödig, R. Duwe, C. Ibbot, D. Jacobson et al. Thermal fatigue tests with actively cooled divertor mock-up for ITER. Fusion Engineering and Design, 39-40 (1998) 551-557.
60. M. Rödig, M. Akiba, P. Chappuis, R. Duwe, M. Ferbe et al. Comparison of electron beam test facilities for testing of high heat flux components. Fusion Engineering and Design, 51-52 (2000) 715-722.
61. W.H. Bowes. Stress analysis by the finite element method for practicing engineers, Berlin, 1975.
62. R.W.Lewis, K. Morgan, H.R. Thomas, K.N. Seetharamu. The finite element method in heat transfer analysis, 1996.
63. ANSYS Basic Analysis Procedures Guide. Release 5.5.
64. J. Smid, E. Kny, M. Scheerer, P. A. Hahn, G. Korb, J. Linke and G. Vieider. Non-destructive characterization of plasma-sprayed tungsten and braze-joints for fusion by ultra-sonic examination, Fusion Engineering and Design. 42 (1998) 511-517.
65. Elio D'Agata, S. Grigoriev, G. Federici, C. Ibbott, A. Makhankov, V. Tanchuk and R. Tivey. Behaviour of the PFC tiles on the ITER divertor under critical loading conditions. Fusion Engineering and Design, 66-68 (2003) 329-334.
66. P. A. Ageladarakis, A. Webster, N. P. O'Dowd and S. Papastergiou. Safety analyses of water cooled components inside the JET thermonuclear fusion tokamak. Fusion Engineering and Design, 45 (1999) 241-256.
67. Manufacturing of High Heat Flux Components. Plansee GmbH. Final Report. 2002
68. Handbuch UBSoft 1.9
69. S.E. Pestchanyi. Effective thermal conductivity of graphite materials with cracks. To be published.
70. B. Böttcher, E. Mundry. Zur Fehlererkennbarkeit bei Anwendung von Wärmeflußverfahren an verschiedenen Werkstoffen. Infrarot-Sondertagung, 17./18. 11.1975, MPA Dortmund. Deutsche Gesellschaft für Zerstörungsfreie Prüfung e.V.
71. G. Vieider, M. Merola, F. Anselmi, J. P. Bonal, P. Chappuis, G. Dell'Orco, D. Duglué, R. Duwe, S. Erskine, F. Escourbiac et al. European development of prototypes for

ITER high heat flux components. Fusion Engineering and Design, 49-50 (2000) 135-143.

72. Private communication M.Roedig with M.Merola.
73. M. Merola and G. Vieider On the use of flat tile armour in high heat flux components. Journal of Nuclear Materials, 258-263 (1998) 672-676.
74. ITER database “ITER plasma facing component materials database in ANSYS format”, 1999
75. I.S.Landmann . 10th Carbon Workshop, September 17-19, 2003, to be published
76. S.E. Pestchanyi, 10th Carbon Workshop, September 17-19, 2003, to be published[1]
77. Alessandra Lodato. Assessment of Beryllium as a plasma facing material for next step fusion devices. Dissertation. RWTH Aachen, 2001.
78. Duwe, R., Kühnlein, W., Pott, G., Plenary meeting of European working group “hot laboratories and remote handling” (1998).
79. G. Janeschitz, et al., ITER Divertor and Pumping and Fueling System Designs and Development of a Full Size Divertor Cassette Prototype for ITER, 16th IAEA Fusion Energy Conf., Montreal, Canada, 7–11 October, 1996
80. B.C. Odegard Jr., C.H. Cadden and N.Y.C. Yang. Beryllium–copper reactivity in an ITER joining environment. Fusion Engineering and Design, 39-40 (1998), 63.
81. P. Lorenzetto, A. Cardella, W. Daenner et al. ITER primary first wall mock-up fabrication and testing for Be/Cu alloy joining development. Fusion Engineering and Design, 61-62 (2002) 643-648.
82. F. Saint-Antonin, D. Barberi, G. Le Marois and A. Laillé. Development and characterisation of Be/Glidcop® joints obtained by hot isostatic pressing for high temperature working conditions. Journal of Nuclear Materials, 258-263 (1998) 1973-1978.
83. M. Rödig, R. Conrad, H. Derz, R. Duwe, J. Linke, A. Lodato, M. Merola, G. Pott, G. Vieider and B. Wiechers. Neutron-irradiation effects on high heat flux components – examination of plasma-facing materials and their joints. Journal of Nuclear Materials, 283-287 (2000) 1161-1165
84. M. Rödig, D. Pitzer. Thermal conductivities of CFC materials NB31 and NS31 after neutron irradiation in the experiments PARIDE 3 and PARIDE 4. Interim Report. 2003.
85. M. Rödig, D. Pitzer. Thermal conductivities of tungsten materials after neutron irradiation. Final Report. 2003.
86. W.Schenk, D. Pitzer. Messung der Temperaturleitfähigkeit an unbestrahlten CFC- and SiC-Proben for Bestrahlungsexperiment PARIDE 4. FZJ-report, 1999.

87. M. Merola, V. Barabash, R. Jakeman, I. Smid. ITER plasma facing components materials data base in ANSYS format – Version 1.2 – Jan. 1999. ITER Doc. G 17 MD 7196-11-19 W0.1
88. Carbon Materials for Advanced Technologies. Edited by Timothy D. Burchell. 1999.
89. M. Roedig, W. Kuehnlein, J. Linke, M. Merola, et al. Investigation of tungsten alloys as plasma facing materials for the ITER divertor. Fusion Engineering and Design, 61-62 (2002) 135-140.
90. Escourbiac, P. Chappuis, J. Schlosser, M. Merola, I. Vastra and M. Febvre High heat flux behaviour of damaged plasma facing components. Fusion Engineering and Design, 56-57 (2001) 285-290 .
91. High heat flux tests of primary wall mock-ups. Final report EFDA. 2003.
92. Vieider, M. Merola, F. Anselmi, J. P. Bonal, P. Chappuis, G. Dell'Orco, D. Duglué, R. Duwe, S. Erskine, F. Escourbiac et al. European development of prototypes for ITER high heat flux components. Fusion Engineering and Design, 49-50 (2000) 135-143.

Appendices

Appendix to Chapter 3

Table A3 - 1. Investigated plasma facing components

Number	ITER part	Module structure	Joining technique	Type of geometry	Year of experiment
FT107-1	Divertor	NB31/CuCrZr	Brazing/TiCuNi	Flat tile	2001
FT107-2	Divertor	NB31/CuCrZr	Brazing/TiCuNi	Flat tile	2002
FT107-3	Divertor	NB31/CuCrZr	Brazing/TiCuNi	Flat tile	2002
FT109-2	Divertor	NB31/CuCrZr	HIP at 550°C/ Au and Ni	Flat tile	2001
FT109-2	Divertor	NB31/CuCrZr	HIP at 450°C/ Au and Ni	Flat tile	2001
FT 108	First Wall	Be/CuAl25	HIPing at 825°C	Flat tile	2001
FT99-1	First Wall	Be/CuAl25	HIPing at 740°C	Flat tile	2001
FT99-2	First Wall	Be/CuAl25	Brazing at 780°C	Flat tile	2001
FT119	First Wall	Be/CuCrZr	Brazing at 780°C	Flat tile	2002
FT120	First Wall	Be/CuCrZr	HIPing at 780°C	Flat tile	2002
FT121	First Wall	Be/CuCrZr	HIPing at 730°C	Flat tile	2003
FT121	First Wall	Be/CuCrZr	HIPing at555°C	Flat tile	2003
FT111	First Wall	Be/CuCrZr/ AISI316	HIPing at 580°C	Flat tile	2002
FT 83-3	Divertor	W/CuCrZr	Electron beam brazing	Macrobrush	1999
FT83-5	Divertor	W/CuCrZr	Electron beam brazing	Macrobrush	2002
FT83-8	Divertor	W/CuCrZr	Electron beam brazing	Macrobrush	2003
FT85-9	Divertor	CFC NS31/ CuCrZr	AMC + electron beam brazing	Flat tile	1999
FT85-11	Divertor	CFC NS31/ CuCrZr	AMC + electron beam brazing	Flat tile	2003
FT85-12	Divertor	CFC NS31/ CuCrZr	AMC + electron beam brazing	Flat tile	2003
FT113-1	Divertor	CFC NB31	AMC/HIP	Monoblock	2003
FT113-2	Divertor	CFC NB31	AMC/HIP	Monoblock	2003

Appendix to Chapter 4

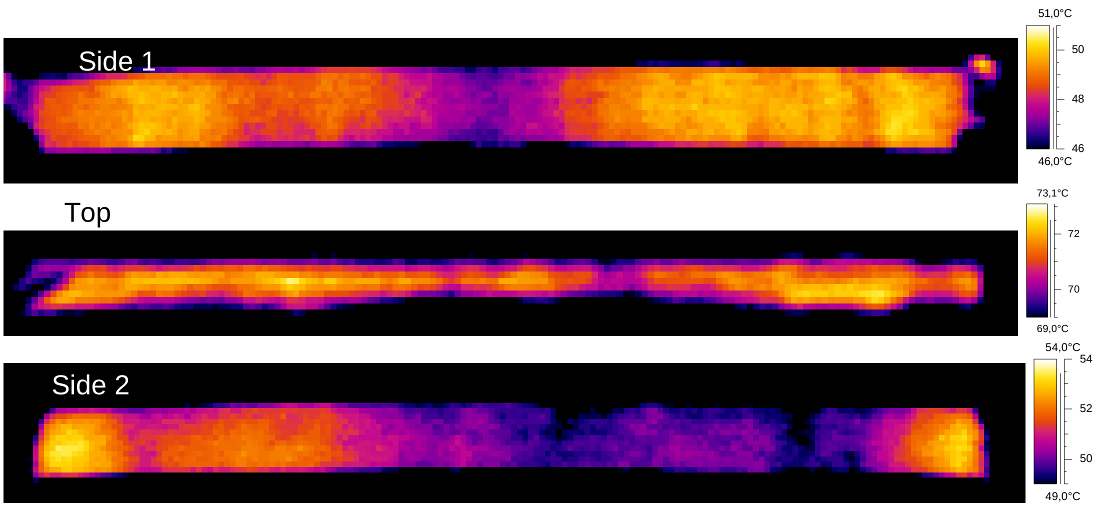

Figure A4 - 1. Infrared observation of the module FT 113-1 during water heating on IRINA after 3.02 s from begin

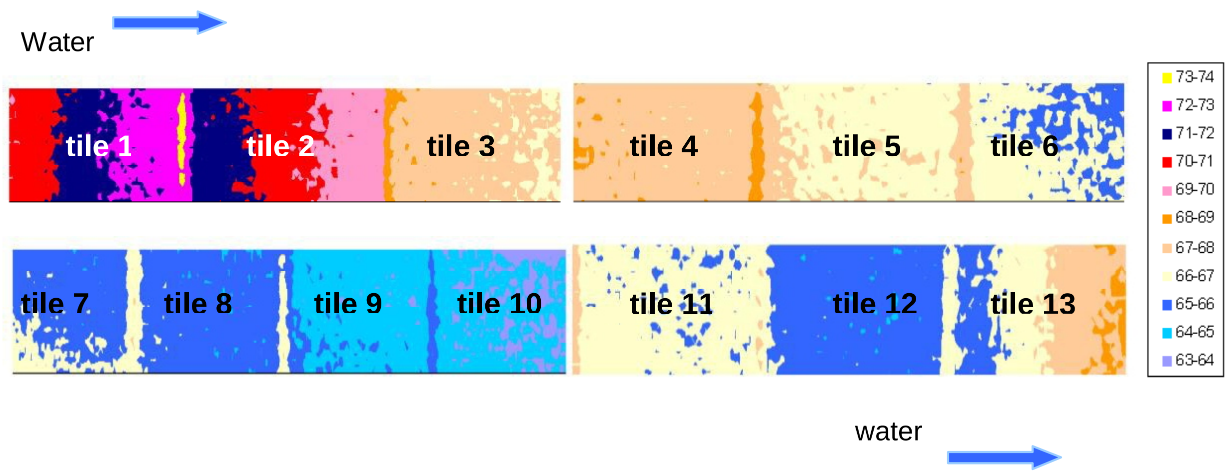

Figure A 4-2. Temperature distribution after 11 s heating up of a TMZ-module

The infrared inspection in facility IRINA of a TMZ-module have been done. The module was made up of a heat sink of the molybdenum –alloy TZM with a cooling tube of Mo41Re and armour tiles of 2D CFC brazed to the heat flux facing side [2]. The module's armour consisted of 13 tiles. The length of the module was 640 mm [2].

The module was firstly cooled down with the cold water (19 °C) flowing through cooling channel of the module. Water run from tile 1 to tile 13. After switching over of the water loop the module was heated with the hot water. CFC surface was observed by an IR camera. In Figure A4-2 the surface temperature is shown. The temperature was measured at the moment of maximum detection sensibility (MDS) (see Chapter 4.5). The moment of MDS occurred after 11 s hot water heating.

As it can be seen in Figure A4-2, there is a noticeable temperature gradient from tile 1 to tile 10. The temperature reduces from 71 °C on tile 1 to 64 °C on tile 10. The temperature drop of about 7 °C takes place on the module's length of ~500 mm (first ten tiles). This surface temperature gradient connects with the fact, that the hot water flowing through the module cools down due to heat consumption going to heating of the module. The tiles 11-13 are at higher temperature than the tile 10 in spite of the fact that the tiles 11-13 are located after tile 10 along the water flow direction. The higher temperature level on tiles 11-13 can be connected with the CFC surface state (differing emissivity) or with local heat transfer properties of the module structure in this area.

The reduction of temperature of hot water in cooling channel by infrared inspection of the lengthy modules impacts the sensitivity of this inspection method. If the impact of defects on surface temperature in investigated area is lower than the surface temperature gradient arising from temperature reduction of hot water due to heating of a module, the infrared inspection by hot water heating will be not possible.

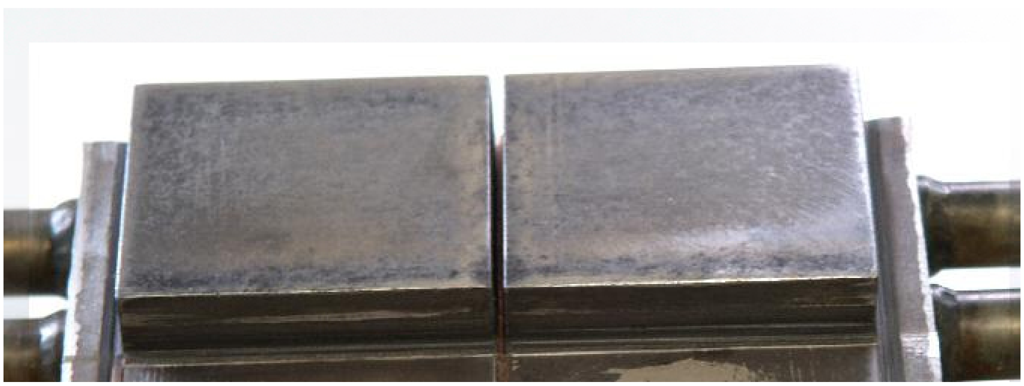
(A)

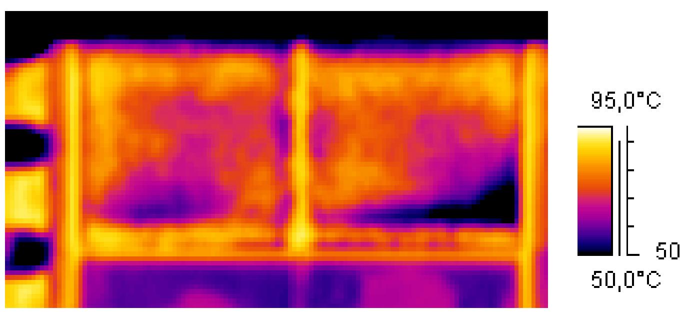

(B)

Figure A4-3. The module FT 121: (a) surface state (b) infrared image at steady state

The infrared inspection of a Be-flat tile module was carried out. The module FT 121 was investigated (see Table A5.3-1 and Table A5.3-2). The complication for investigation of a Be surface consists in the high emissivity variation of Be due to the surface state (see Chapter 5.3.1).

Figure A4-3 shows a Be armour of the module FT 121. The surface (Figure A4-3a) seems to be nonhomogeneous due to presence of oxide film and surface contamination. Figure A4-3b demonstrates the same surface at steady state during hot water heating in the facility IRINA in infrared spectrum. The surface temperature changes in the range of 50 °C up to 90 °C in spite of the fact that the module reached steady state at temperature about 90 °C. This temperature variation is explained by high emissivity variation of the Be surface.

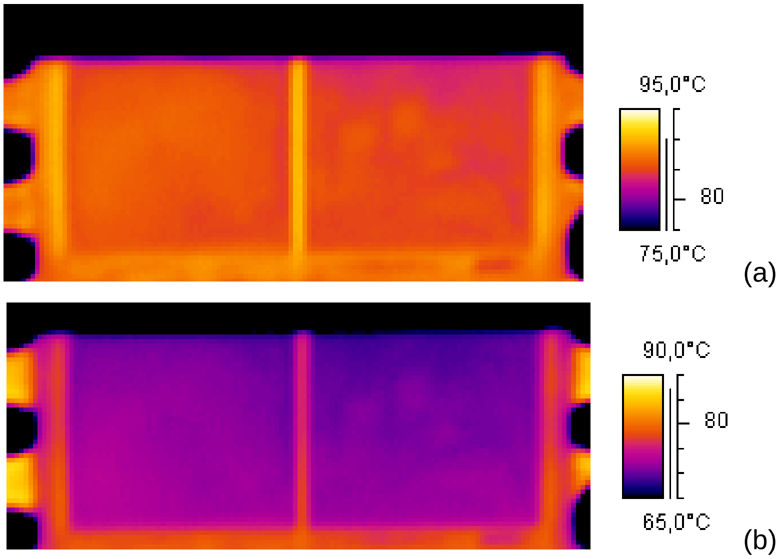

Figure A4-4. FT 121: graphite spray-coated armour at (a) steady state, (b) after 17 s heating up.

The module surface was coated with graphite spray for eliminating the impact of surface state on the temperature measurement. The results of infrared inspection of a coated Be-module FT 121 are shown in Figure A4-4. Figure A4-4a presents the surface at steady state. The surface temperature varies in the rage from about 85 °C up to 90 °C. So the graphite spraying changes the surface state and helps to correct the surface emissivity variation. Figure A4-4b demonstrates the Be-surface of the module FT 121 after 17 s heating up.

Appendix to Chapter 5.1

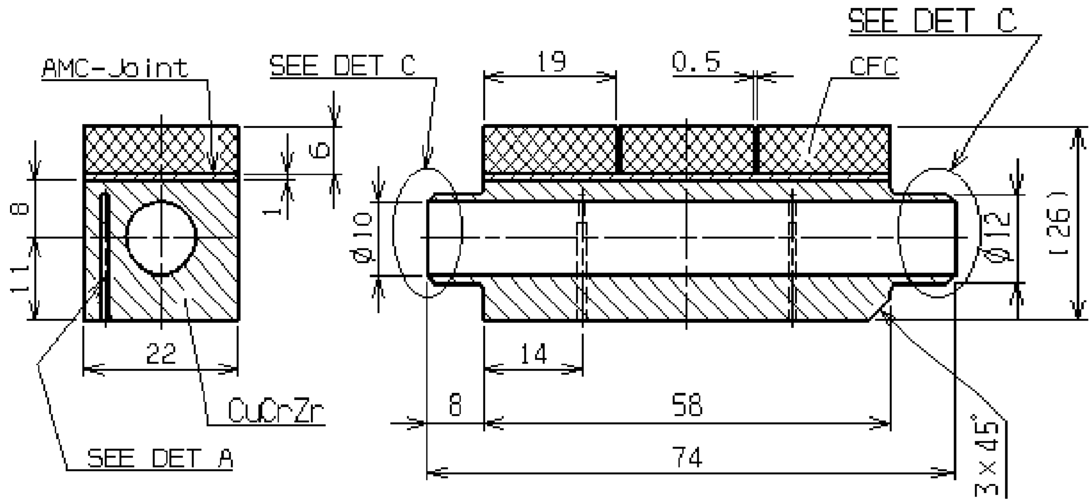

Figure A5.2 - 1. Design drawing of the CFC modules FT 107-1,2,3 and FT 109-2,3

Table A5.2-1. Loading procedures for the modules with CFC armour

Loading type	Incident power density	Absorbed power density, MW/m2	Loaded area	Result
FT 107-1				
Screening	2.5	2.3	Tiles 1-3	Successful
Screening	5.6	4.9	Tiles 1-3	Tile 2 overheated
Thermal fatigue, 10 cycles	5.6	4.9	Tiles 1-3	Tile 2 detached
FT107-2				
Screening	1.1-5.5	1-5.1	Tiles 1-3	Successful
Thermal fatigue, 100 cycles	5.5	5.1	Tiles 1-3	Successful
Screening	8.3-9.9	6.9-9.9	Tiles 1-3	Detachement of tile 1
Screening	10.9	10.1	Tile 2-3	Detachment of tile 2
Thermal fatigue, 15 cyles	11	10	Tile 3	Detachment of tile 3
FT107-3				
Thermal fatigue, 100 cycles	5.4	4.9	Tiles 1-3	Successful
Thermal fatigue, 1000 cycles	10.8	10.4	Tiles 1-3	Successful
Thermal fatigue, 100 cycles	13.2	12	Tiles 1-3	Successful
Thermal fatigue, 1000 cycles	16.5	15.3	Tiles 1-3	Slight temperature increase on all tiles
Thermal fatigue, 100 cycles	19	16.9	Tiles 1-3	Slight temperature increase on tile 1
Thermal fatigue, 200 cycles	21.6	19	Tiles 1-3	Detachment of tile 1
FT109-2				
Screening	2.1-5.4	1.7-5.2	Tiles 1-3	Successful
Thermal fatigue, 35 cycles	5.4	5.2	Tiles 1-3	detachment of tile no. 1 after ~ 20 cycles
Screening	5.4	5.2	Tiles 2-3	Successful
Thermal fatigue, 100 cycles	5.4	5.2	Tiles 2-3	Successful
Thermal fatigue, 300 cycles	10.5	9.8	Tiles 2-3	Increase of surface temperature, detachment of tile 2
FT109-3				
Screening	2.1-5.4	1.7-5.2	Tiles 1-3	Successful
Thermal fatigue, 100 cycles	5.4	5.0	Tiles 1-3	Successful
Screening	8.2-10.9	7.6-10.2	Tiles 1-3	Successful
Thermal fatigue, 60 cycles	10.9	10.2	Tiles 1-3	Increase of surface temperature, detachment of tile 2 and 3

CFC flat tile brazed module FT107-1

The module FT107-1 had a defect brazing interlayer between the CFC tile 2 and the heat sink. It caused the detachment of the tile 2 already in the first loading step under thermal fatigue conditions at an absorbed power density of 4.9 MW/m^2. Figure A5.2 - 2 shows the surface temperature distribution during the 1st, 5th and 10th heating cycles. The temperature on the tile 2 increased very sharply and surface overheating occured after 10 cycles.

A screening test was carried out on the module FT107-2 before thermal fatigue testing (Table A5.1-1, Appendices). The module survived high heat flux loads of up to 10 MW/m^2 (absorbed).

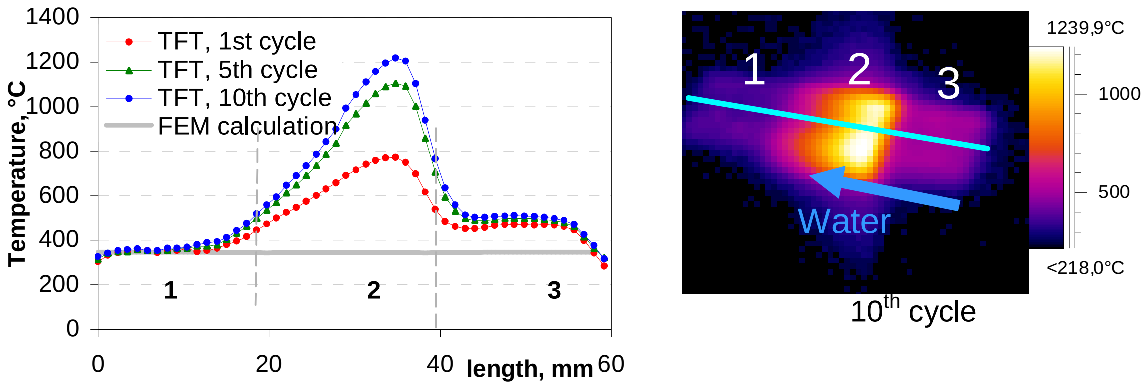

Figure A5.2 - 2. Temperature distribution and infrared picture during thermal fatigue testing of the module CFC FT107-1 at 4.9 MW/m^2

CFC flat tile HIPed module FT109-3

The modules FT109-2 and FT109-3 were manufactured to study the thermal fatigue behavior of an alternative joining technique, HIPed CFC flat tile mock-up.

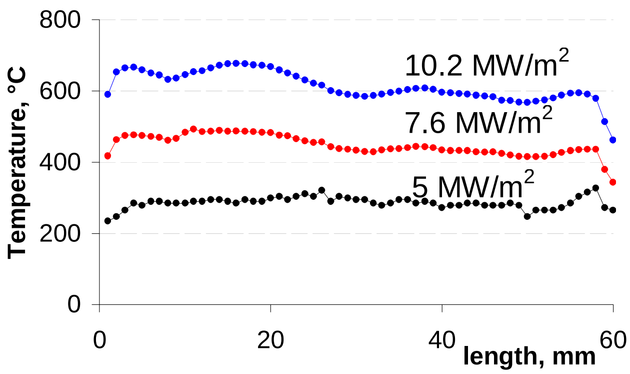

Figure A5.2 - 3. Temperature during the Screening test of the CFC module FT109-3

The mock-up FT109-3 had a pre-existing defect in the joint at tile 1. Therefore, overheating was observed in this area containing the defect during the experiment. Figure A5.2 - 3 and Figure A5.2 - 4 show the surface temperatures of the CFC-armor at three different absorbed power densities. The surface temperature profiles are the results of screening test at 5, 7.6 and 10.2 MW/m^2. The temperature of the left part, which corresponds to tile 1, is already higher at 7.6 MW/m^2. Figure A5.2 - 4 presents the results from the thermal fatigue tests. After 60 cycles at 10.2 MW/m^2 significant surface overheating at the armour tile 1 was observed, indicating a detachment. Both other tiles also showed a small temperature increase during thermal fatigue cycling. Tile 2 is also overheated from the left side.

CFC flat tile HIPed module FT109-2

Figure A5.2 - 5 and 9 demonstrate a similar behaviour for module FT109-2 under high heat loads. In this case, tile 1 detached during the thermal fatigue test at 5.2 MW/m^2 after 35 cycles only. Figure A5.2 - 5 demonstrates the temperature distribution along the module during screening tests. Figure A5.2 - 6a shows an infrared picture taken during thermal fatigue testing at 5.2 MW/m^2, when tile 1 was overheated. The surface temperature increased strongly at tile 1 and finally tile 1 detached. After a reduction of the heated area to tiles 2 and 3, tile 2 did not show any failure during 300 cycles at 9.8 MW/m^2 absorbed power density.

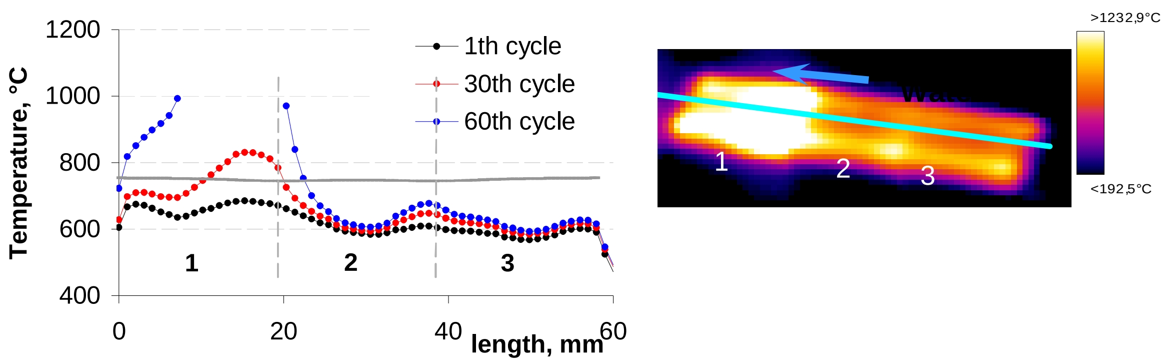

Figure A5.2 - 4. Surface temperature of the module FT109-3 during thermal fatigue test at 10.2 MW/m^2

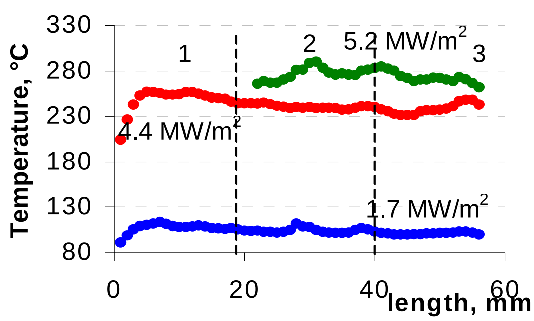

Figure A5.2 - 5. Surface temperature during screening test of the CFC module FT109-2

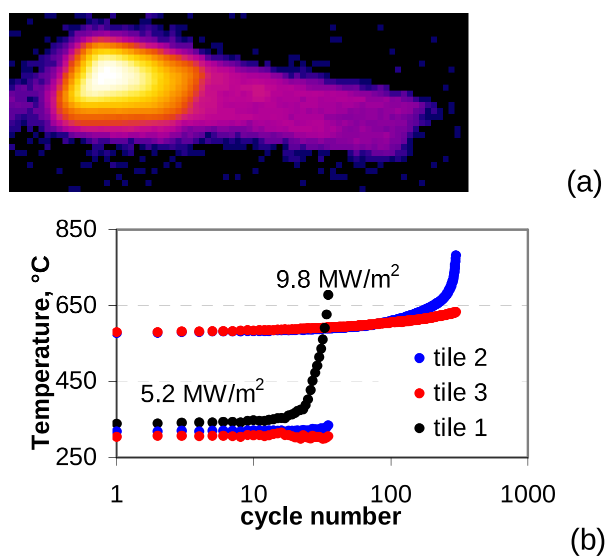

Figure A5.2 - 6. Infrared image and temperature increase during thermal fatigue test of the CFC module FT109-2

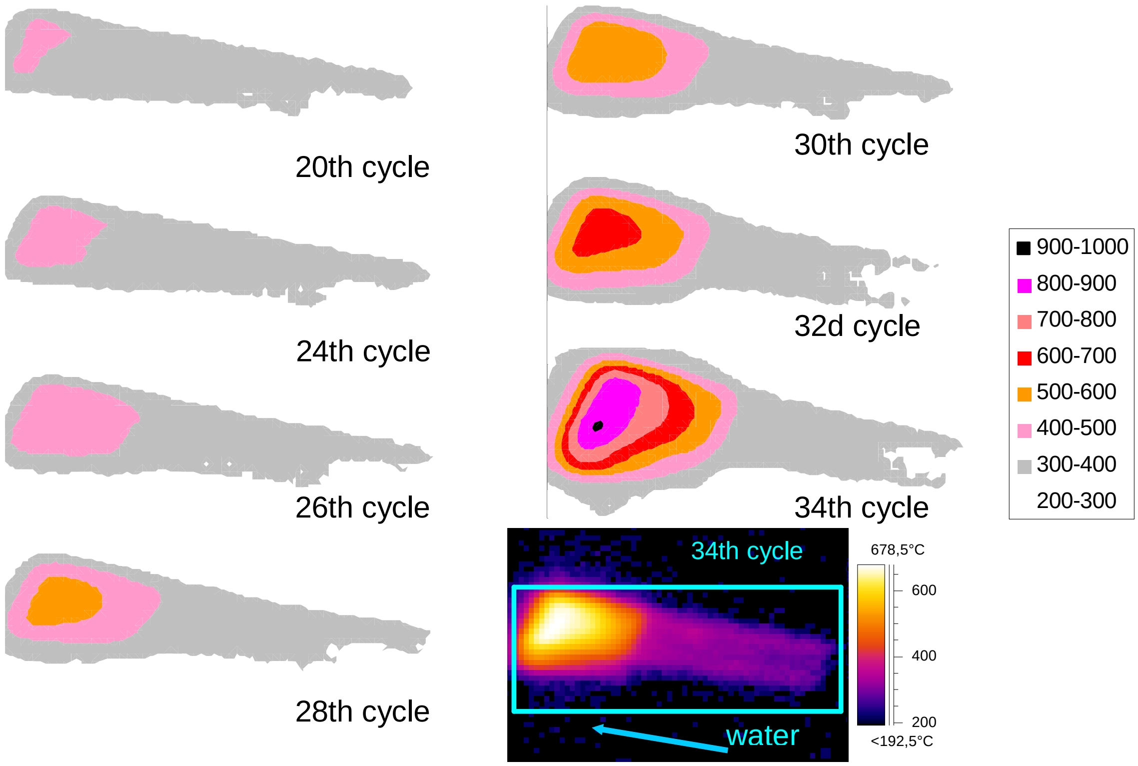

Figure A5.2 - 7. Evolution of the overheated zone on the surface of the CFC module FT 109- 2 at an absorbed power density of 5.2 MW/m^2

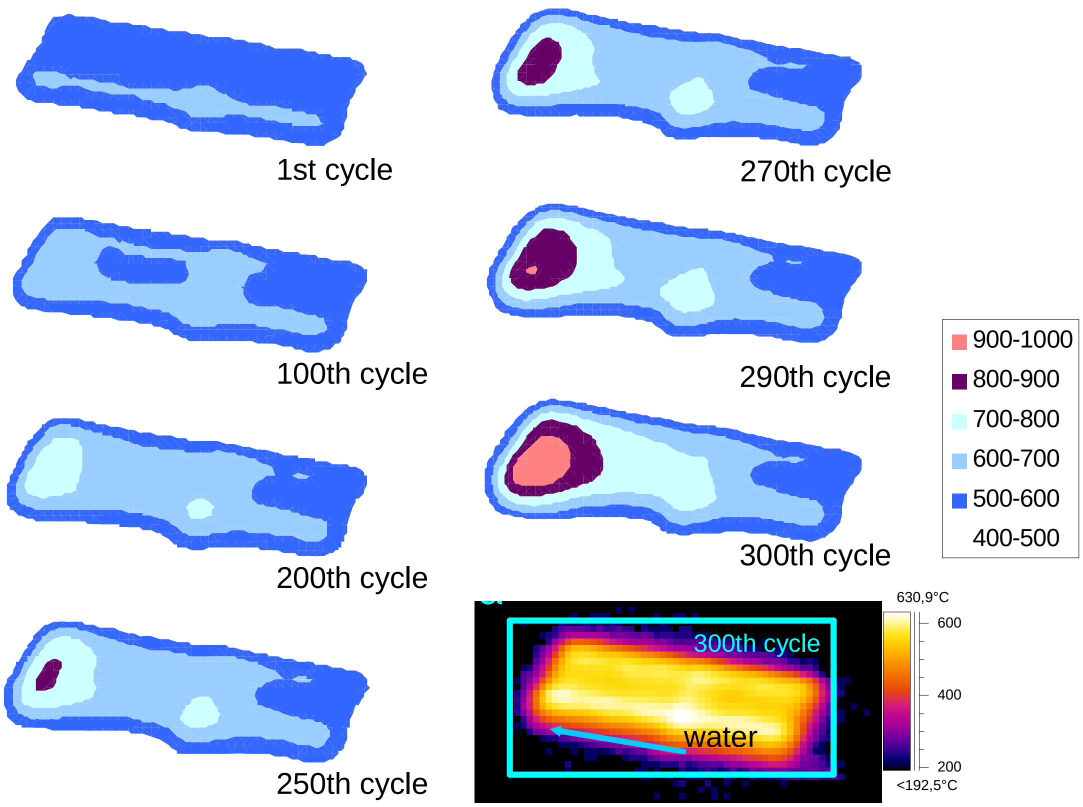

Figure A5.2 - 8. Evolution of the overheated zone on the tile 2 of the CFC module FT 109-2 at an absorbed power density of 9.8 MW/m^2.

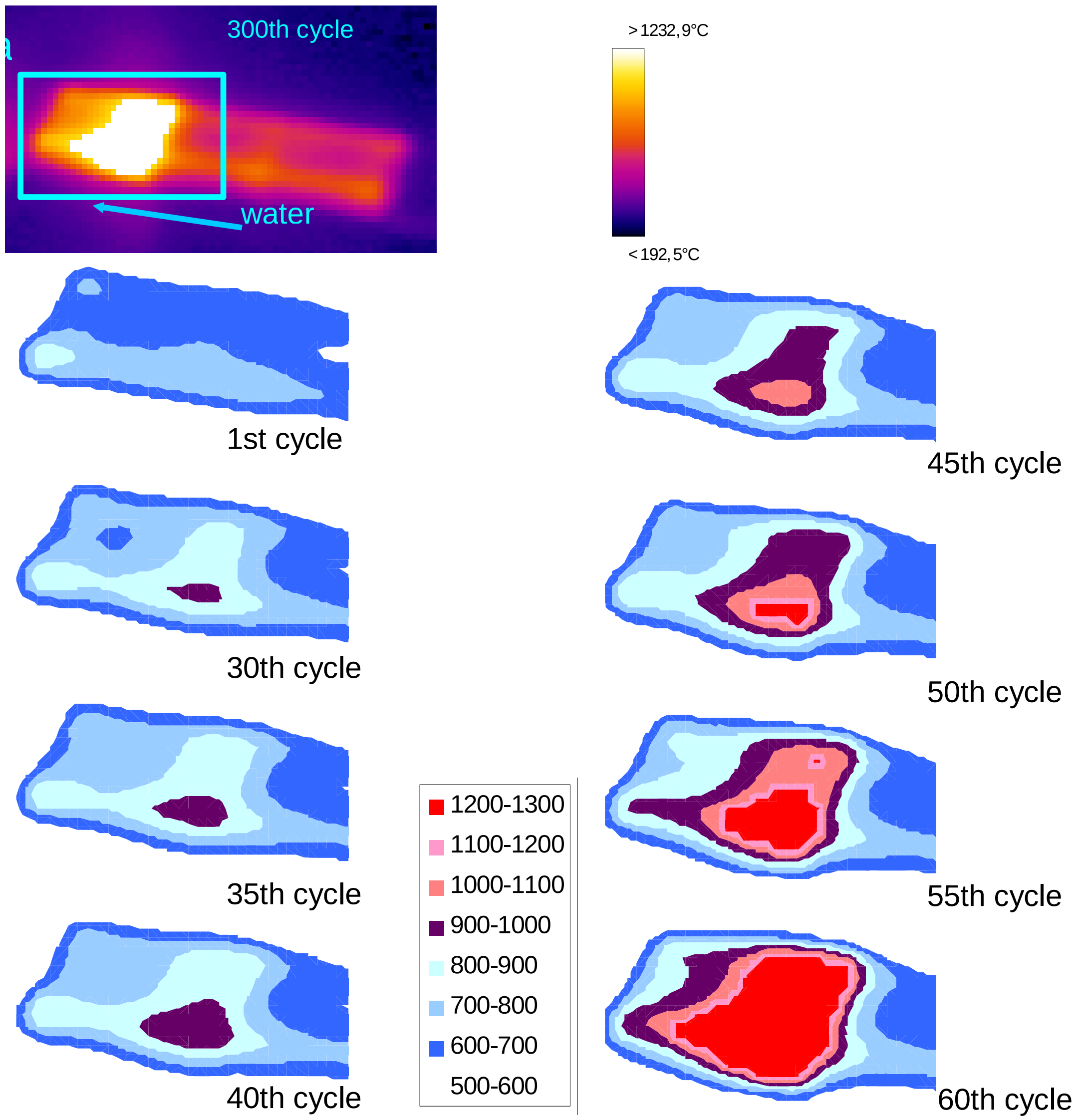

Figure A5.2 - 9. Evolution of the overheated zone on the surface of the CFC module FT 109-3 at an absorbed power density of 10.2 MW/m^2

Appendix to Chapter 5.3

Table A5.3 - 1. Materials and manufacturing technology of the Be-modules

Module	Armour	Heat sink	Joining technique	Number of tiles	EFDA number
FT108	Beryllium S65C	CuAl25	HIPing at 825°C	1	DS 16 J
FT 99-1	Beryllium S65C	CuAl25	HIPing at 740°C	1	DS-18J
FT99-2	Beryllium S65C	CuAl25	Brazing at 780°C	1	DS-19J
FT119	Beryllium S65C	CuCrZr	Brazing at 780°C	4	PHS-10J
FT120	Beryllium S65C	CuAl25	HIPing at 780°C	4	DS-17J
FT121	Beryllium S65C	CuAl25	HIPing at 730°C	4	DS-20Jb
FT122	Beryllium S65C	CuCrZr	HIPing at555°C	4	PH/S-7J
FT111	Beryllium S65C	CuAl25	HIPing at 580°C	6	DS-13I

Table A5.3-2. Loading procedures for the modules with beryllium armour

Loading type	Incident power density	Absorbed power density, MW/m2	Loaded area	Result
FT99-1				
Screening	1.2-3.1	1.0-2.5	Tile 1	Successful
Screening	3.75	3.0	Tile 1	Detachment
FT 99-2				
Screening	1.2	1.0	Tile 1	Successful
Thermal fatigue, 1000 cycles	2.0	1.6	Tile 1	Successful
Screening	3.8	3.1	Tile 1	Detachment
FT108				
Screening	1.2-1.8	1.0-1.5	Tile 1	Successful
Screening	2.4	2.1	Tile 1	Successful
Thermal fatigue	2.4	2.1	Tile 1	Failure of tile 1during 2nd cycle
FT119				
Screening	1.2-1.8	1.0-1.5	Tiles 1-4	Successful
Thermal fatigue, 1000 cycles	1.8	1.5	Tiles 1-4	Successful
Screening	1.9-2.4	1.6-2	Tiles 1-4	Successful
Thermal fatigue, 200 cycles	2.4	2.0	Tiles 1-4	Increase of surface temperature
Screening	3.0	2.5	Tiles 1-4	Failure of tile 4
Screening	3.0	2.5	Tiles 1-2	Failure of tile 1 during cooling down
FT120				
Screening	1.2-1.7	1.1-1.5	Tiles 1-4	Successful
Thermal fatigue, 1000 cycles	1.7	1.5	Tiles 1-4	Successful

Screening	1.9-2.3	1.7-2.0	Tiles 1-4	Successful
Thermal fatigue, 17 cycles	2.3	2.0	Tiles 1-4	Failure of tiles 1 and 2 during 17th cycle
FT121				
Screening	0.6-1.8	0.5-1.5	Tiles 1-2	Successful
Thermal fatigue, 1000 cycles	1.85	1.45	Tiles 1-2	Surface temperatures on both tiles constant
Screening	2.5	2	Tiles 1-2	Successful
Thermal fatigue, 200 cyles	2.5	2	Tile 1-2	Detachment of tile 2 during 1st cycle
Screening	2.5	2	Tile 1	Detachment of tile 1
FT 122				
Screening	0.65-1.85	0.5-1.45	Tiles 1-4	Successful
Thermal fatigue, 1000 cycles	1.85	1.45	Tiles 1-4	Successful
Screening	2.4	2	Tiles 1-4	Successful
Thermal fatigue, 200 cycles	2.3	1.9	Tiles 1-4	Successful
Screening	3.05	2.6	Tiles 1-4	Successful
Thermal fatigue	3.05	2.6	Tiles 1-4	failure of tile 1 during 1st cycle
FT 111				
Screening	0.6-1.8	0.4-1.5	Tile 1	Successful
Thermal fatigue, 66 cycles	1.8	1.5	Tile 1	Overheating of tile no.1
Screening	0.55-1.8	0.4-1.5	Tiles 2, 3, 4	Successful
Thermal fatigue, 1000 cycles	1.8	1.5	Tiles 2, 3, 4	Overheating of tile no.4
Screening	0.6-1.7	0.4-1.4	Tiles 5, 6	Successful
Screening	1.8	1.5	Tiles 5,6	Overheating of tile no.6
Screening	0.5-1.8	0.4-1.5	Tile 5	Successful
Thermal fatigue, 1000 cycles	1.8	1.5	Tile 5	Successful

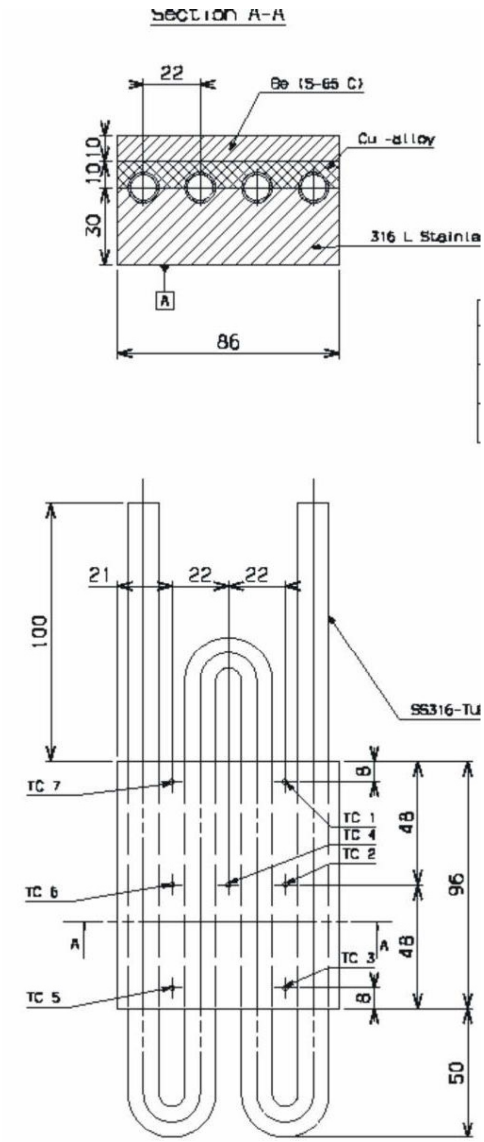

Figure A5.3 -1. Drawing of the beryllium modules FT 108, FT99-1,-2

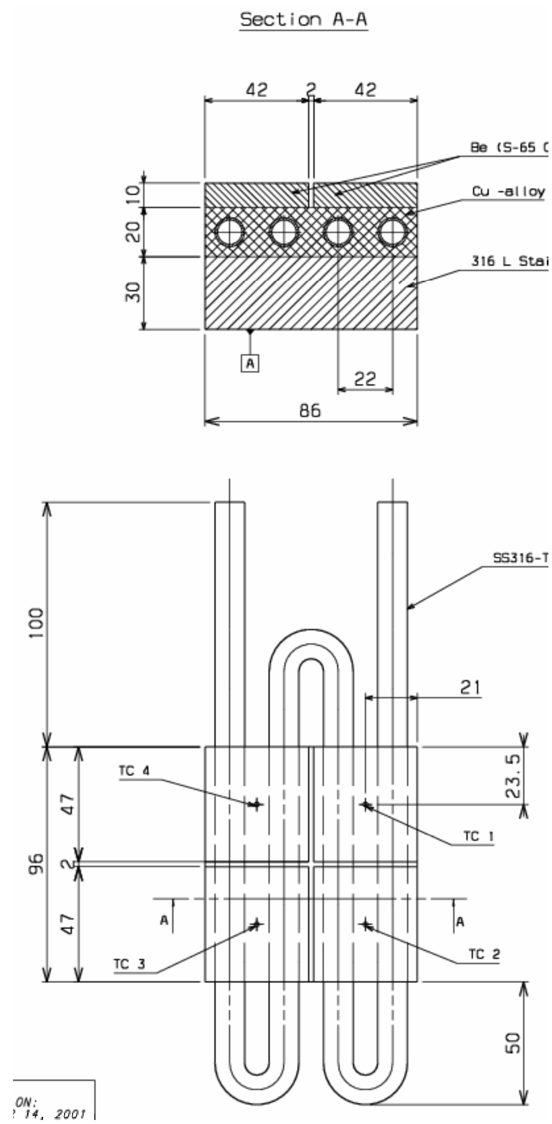

Figure A5.3 - 2. Drawing of the beryllium modules FT 119-122

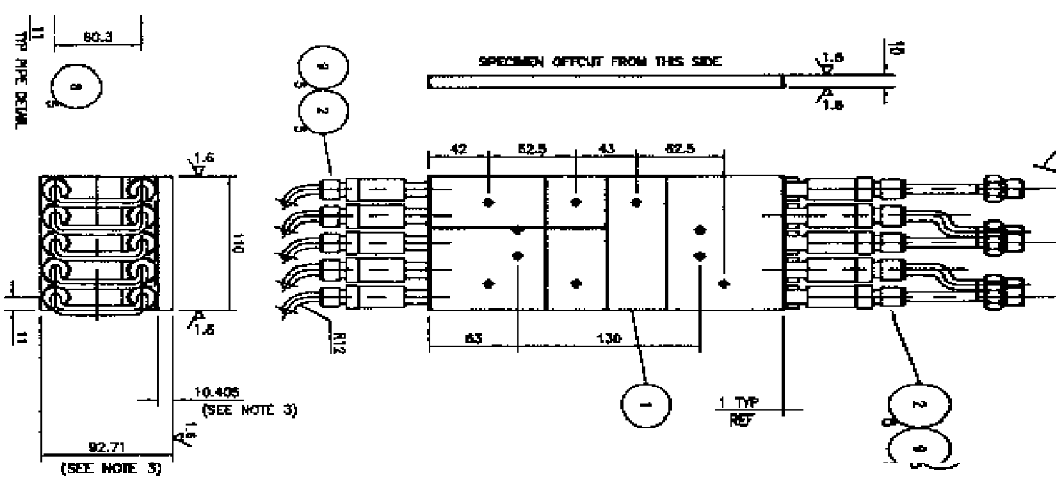

Figure A5.3-3. Drawing of the beryllium module FT 111

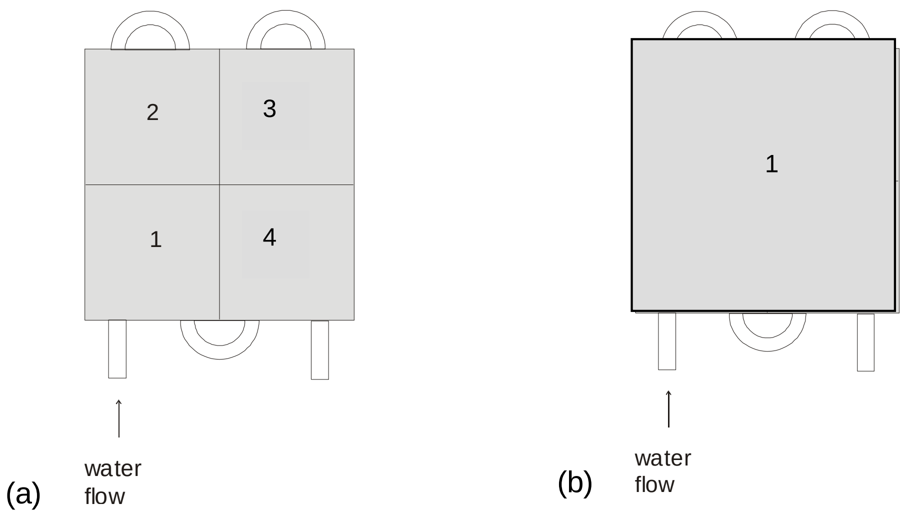

Figure A5.3 - 4. Schema of tile numbering and water flow direction during electron beam loading (a) the Be modules FT119-122 (b) FT 108, FT 99-1,-2

Thermal fatigue behavior of the beryllium module FT 99 - 2

Module FT 99-2 was produced according to the drawing in Figure A5.3-1. The beryllium tiles were joined to a heat sink made from CuAl25. The joining technique of the module FT 99 -2 was brazing.

The behavior of the module FT 99-2 during electron beam loading is demonstrated in Figure A5.3 - 5 and in Figure A5.3 - 6.

Figure A5.3 - 5a shows an infrared image of the surface temperature distribution during a screening test at 3 MW/m^2. In Figure A5.3 - 5b the average surface temperature of the framed area (see Figure A5.3 - 5a) at different loads is presented.

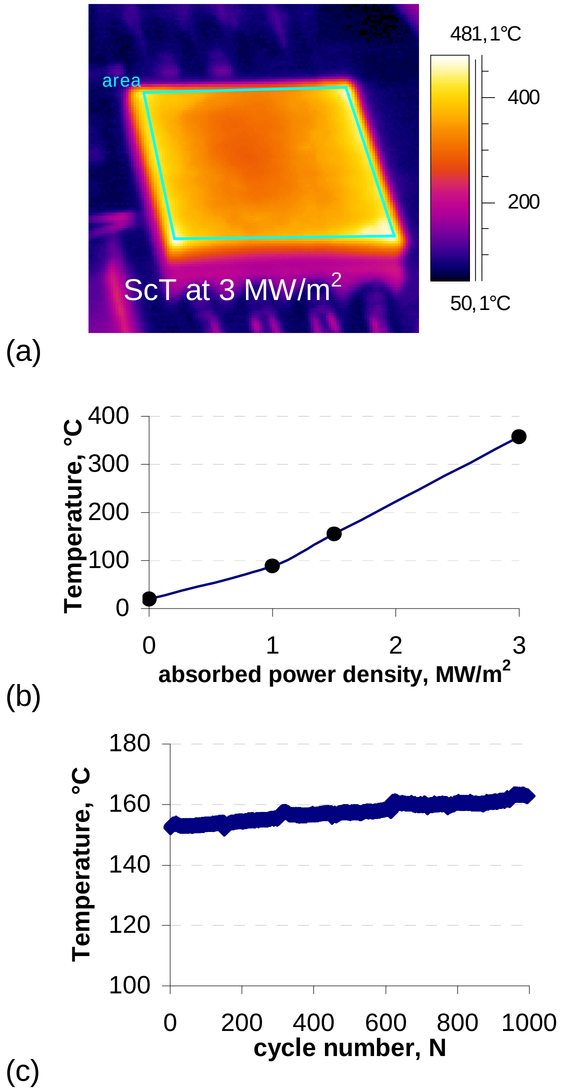

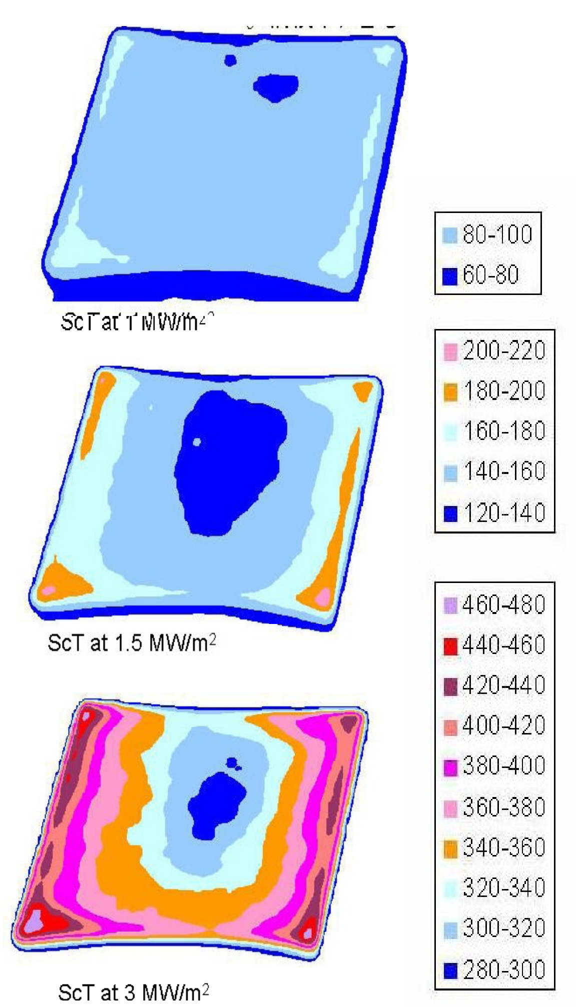

Figure A5.3 - 5. Electron beam loading of the beryllium module FT 99-2 (a) an infrared image during ScT at 3 MW/m^2, (b) temperature increase during different screening loads, (c) thermal fatigue test of FT 99-2 at absorbed power density of 1.6 MW/m^2

Figure A5.3 - 6. Temperature fields during screening tests of the beryllium module FT 99-2

For this module a thermal fatigue test with 1000 cycles at the absorbed power density of 1.6 MW/m^2 was applied. The increase of the average temperature on the tile during cycling is shown in Figure A5.3 - 5c. Temperature increase during the 1000 cycles was not significant and achieved only about 20°C. It is concluded that integrity of the module and its reliable thermal fatigue performance is limited up to 1.6 MW/m^2.

Figure A5.3 - 6 demonstrates the temperature fields during screening tests of the module FT 99-2 at different power densities. Overheating occurred on the edge areas for the first time at 1.5 MW/m^2. Surface temperature in the center is lower than on the edges by about 40-60°C.

During screening at 3 MW/m^2 the temperature difference between the central area and the edges reached 140-160°C, and finally detachment of the beryllium armour was observed.

Thermal fatigue behavior of the beryllium module FT 119

Armour of these four modules was designed as 4 separated tiles. The appearance of these modules is shown in Figure A5.3 - 7 by the example of module FT 119.

The module FT 119 (PHS-10J) consisted of a 30 mm thick 316L stainless steel back plate joined by HIPing onto a 10 mm thick CuCrZr alloy with 10/12 mm 316L stainless steel tubes imbedded in-between. There are four beryllium tiles of the dimensions 10 x 42 x 47 mm^3 joined onto the CuCrZr alloy by HIPing at 530°C for 2 hours [1].

Tile 1 of the module FT 119 was completely detached after high heat flux loading at 2.5 MW/m^2 (Figure A5.3 - 7b). Moreover, Figure A5.3 - 7b shows that the surface of beryllium tiles are appeared to be optically nonuniform, which indicates different emissivity on the surface during the infrared observation.

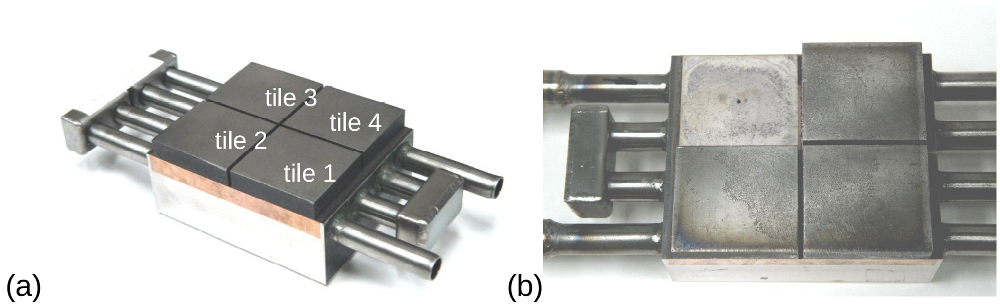

Figure A5.3 - 7. Be module FT 119 (a) before and (b) after high heat flux testing (tile 1 detached)

Figure A5.3 - 8a shows the temperature in the center of each tile at increasing of the electron beam power density during screening tests. Temperatures at the center of each tile (Figure A5.3 - 8b) increased linearly with increase of absorbed power density up to 2.5 MW/m^2. Temperature measured with a pyrometer were slightly higher.

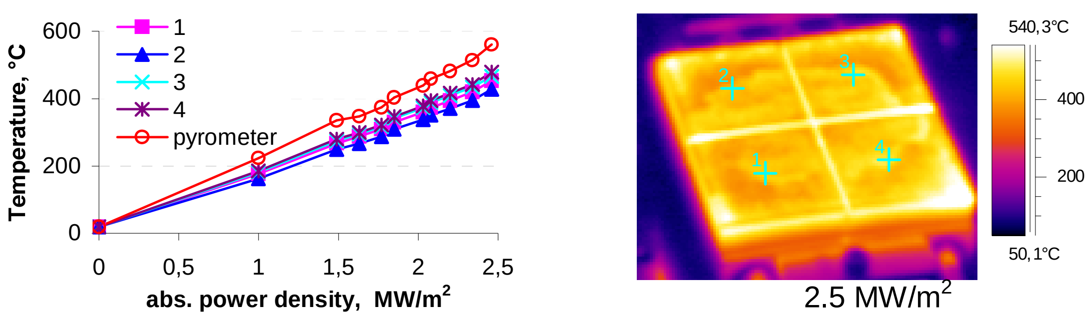

Figure A5.3 - 8. Screening tests of the Be module FT 119

At the absorbed power density of 2 MW/m^2 a thermal fatigue test was carried out. The average temperature of each tile was measured as shown in Figure A5.3 - 9a. Figure A5.3 - 9b shows a slight linear increase of the surface temperatures during 200 cycles. The largest increase was obtained from the tile 4, which failed first during the next load step.

Temperature differences between the tiles do not exceed 30°C. This temperature difference may be due to choice of area for the temperature measurement and the emissivity variation on the surface of beryllium armour.

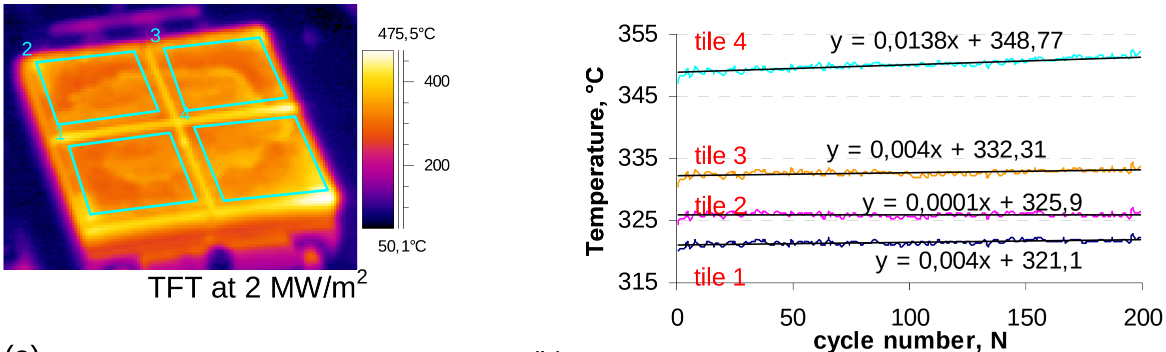

(a) (b)

Figure A5.3 - 9. Thermal fatigue test of the Be module FT 119 at absorbed power density of 2 MW/m^2

Failure of the module FT 119 happened in the following way: during screening at 2.5 MW/m^2 tile 4 failed; during repeated screening tests at the same power density tile 1 detached. Figure A5.3 - 10 shows the optical images of the failure process of tiles 4 and 1.

The testing of tile 4 was stopped because during video observation the dispersion of brightly shining metal drops was fixed (white spots in area A in Figure A5.3 - 10a). Probably, it is the joining material. Apparently, at this power density the brazing interlayer heated up to high temperature and then melted and evaporated.

Figure A5.3 - 10b shows overheating of join of tile1, resulting in fully detachment of beryllium armour. First optical image demonstrates significant overheating of upper right corner of tile 1. Apparently, overheating occurred due to melting of joint under tile 1. In second optical image in Figure A5.3 - 10b a moment is presented, where tile 1 detached from the module surface, and joint heated up and evaporated.

(a) 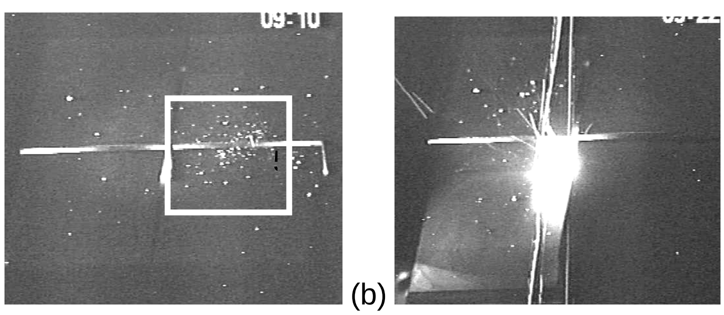 (b)

tile 4 tile 1

Figure A5.3 - 10. Failure of (a) tile 4 and (b) tile 1 of the Be module FT 119 during screening test at 2.5 MW/m^2

Thermal fatigue behavior of the beryllium module FT 120

The module FT 120 (DS-17J) (Figure A5.3 - 11) differs from the module FT 119 by the heat sink material. In this case dispersion strengthened CuAl25 was used. Four beryllium tiles of dimensions 10 x 42 x 47 mm^3 are joined onto the CuAl25 alloy by furnace brazing at 780°C for about 2 minutes [1].

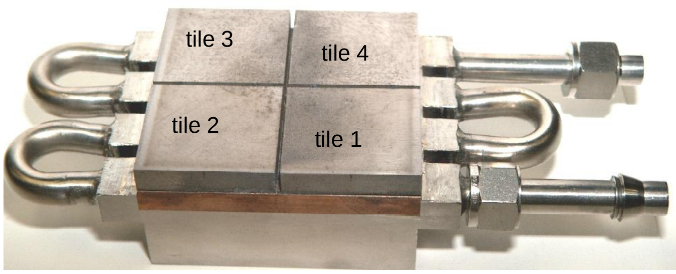

Figure A5.3 - 11. Be module FT 120 before testing

The module FT 120 survived successful loads from 1.1 up to 2 MW/m^2 and 1000 cycles of loading at an absorbed power density of 1.5 MW/m^2. Results are presented in Figure A5.3 - 12 and Figure A5.3 - 13. During screening test the temperature in the center of each tile increases similarly (Figure A5.3 - 12a).

In Figure A5.3 - 13a thermal fatigue behavior of the module FT 120 during 1000 cycles at 1.5 MW/m^2 is presented. Average temperatures for each tile were determined (as shown in Figure A5.3 - 13b). Average temperature on the tile 1 increased slightly during 1000 cycles (temperature increment was estimated to be about 10°C). Significant increase of temperatures on the other tiles was not observed.

As a result of thermal fatigue cycling at 2 MW/m^2 tiles 1 and 2 failed during 17th cycle (Figure A5.3 - 14). Video images of the breakdown process are shown in Figure A5.3 - 15. Overheating of tiles 1 and 2 started from the edges (like for the previously described modules FT 108 and FT 99-1) and expanded to the center of the module surface with a high velocity.

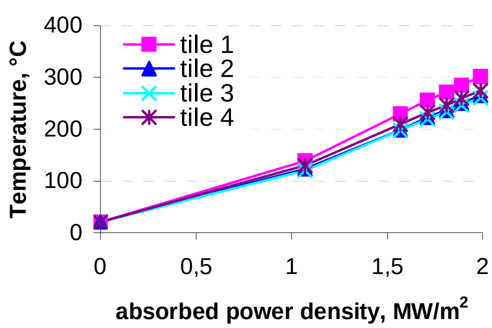

(a)

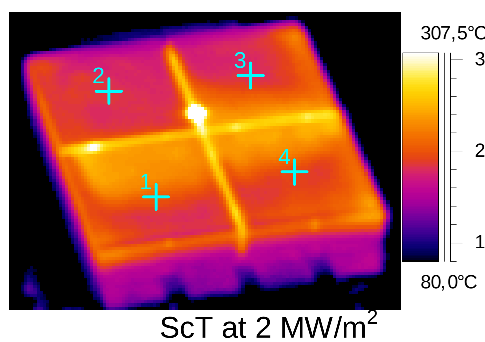

(b)

Figure A5.3 - 12. Screening test of the Be module FT 120

For the estimation of expansion velocity of the overheating front, a diagonal from external corner to internal corner of tile 1 was chosen (line D-D in Figure A5.3 - 15). The velocity of front expansion was calculated by expansion of the front of overheated zone along the line D-D. Average velocity of overheating front expansion according the video file during 17th cycle of thermal fatigue test amounted about few mm per second. As a result of overheating zone expansion the temperature goes sharply up and tile 1 and 2 were detached.

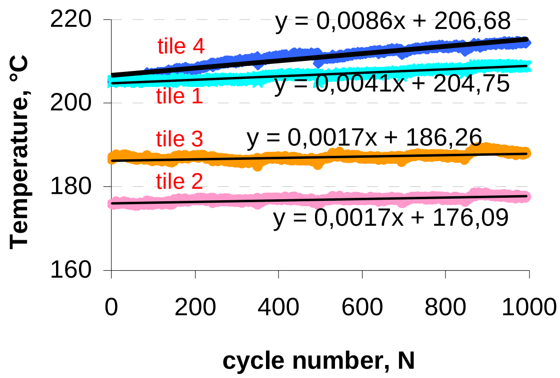

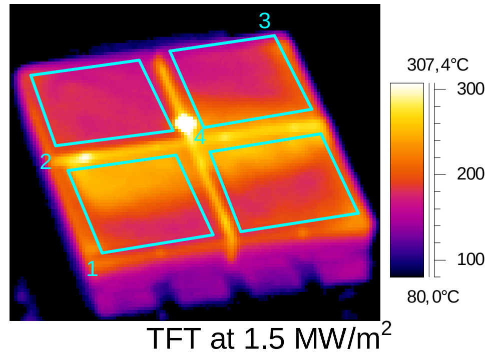

(a) (b)

Figure A5.3 - 13. Thermal fatigue test of the Be module FT 120 at absorbed power density of 1.5 MW/m^2

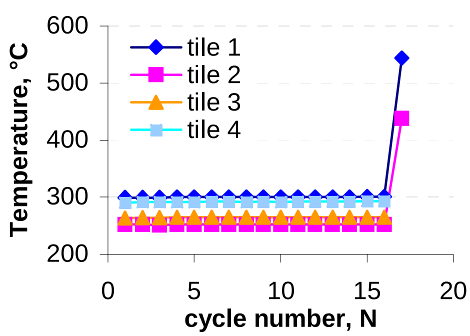

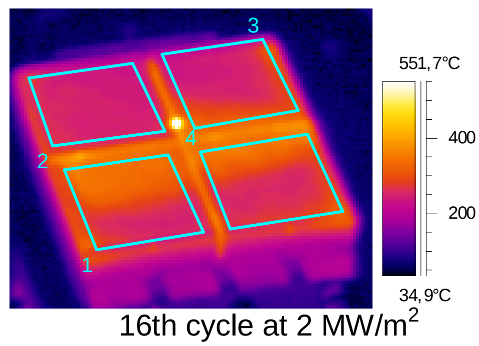

(a) (b)

Figure A5.3 - 14. Thermal fatigue test of the Be module FT 120 at absorbed power density of 2 MW/m^2

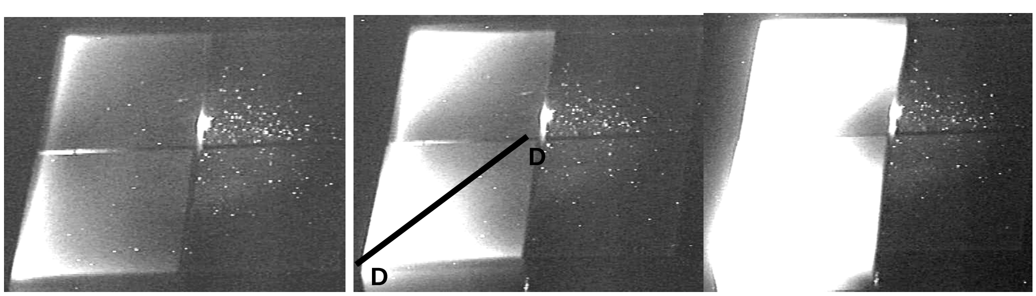

Figure A5.3 - 15. Failure of tiles 1 and 2 of the Be module FT 120 during 17th cycle of thermal fatigue test at absorbed power density of 2 MW/m^2

Thermal fatigue behavior of module FT 121

Module FT 121 (DS-20Jb) consisted of a 30 mm thick 316L stainless steel back plate joined by HIPing onto a 10 mm thick CuAl25 alloy (Grade IG1) with 10/12 mm 316L stainless steel tubes imbedded in-between. There are four beryllium tiles of dimensions 10 x 42 x 47 mm^3 joined onto the CuAl25 alloy by HIPing at 730°C for 1 hour [1]. Two tiles of the module failed during final machining and were not tested.

Results of heat load tests of the module FT 121 are presented in Figure A5.3 - 16 and Figure A5.3 - 17.

The module did not show any failure during 1000 cycles at absorbed power density of 1.45 MW/m^2. Failure of tile 2 happened during the 1st cycle of thermal fatigue test at 2 MW/m^2. Then tile 1 detached during screening at the same power density. The evolution of temperature fields at different screening loads is presented in Figure A5.3 - 17. A wide zone of high temperature was observed on the left side, but overheating of this zone was not significant and it was estimated to be 20-40°C at all absorbed power densities.

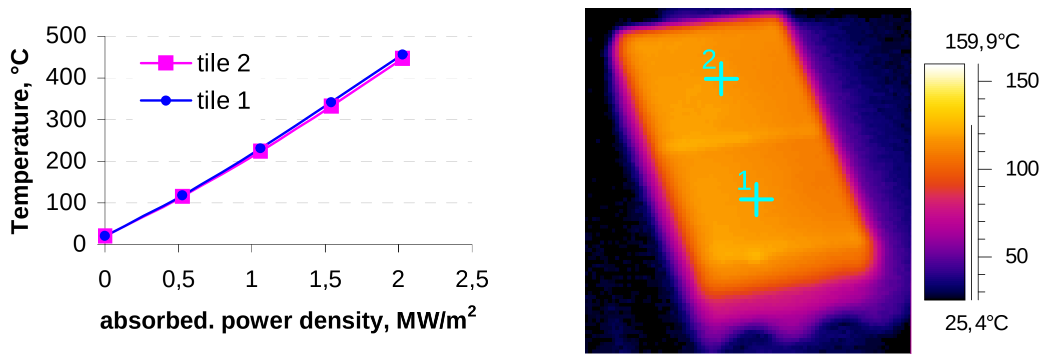

(a) (b)

Figure A5.3 - 16. Screening test of the Be module FT 121

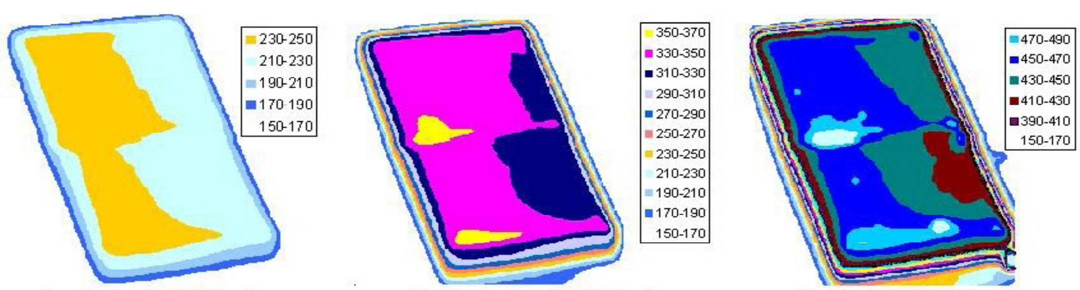

ScT at 1 MW/m^2 ScT at 1.5 MW/m^2 ScT at 2 MW/m^2

Figure A5.3 - 17. Temperature fields during screening test of the Be module FT 121

Thermal fatigue behavior of the module FT 122

The module FT 122 (PHS-7J) consists of a 30 mm thick 316L stainless steel back plate joined by HIPing onto a 10 mm thick CuCrZr alloy with 10/12 mm 316L stainless steel tubes embedded in-between. Four beryllium tiles of dimensions 10 x 42 x 47 mm^3 were joined onto the CuCrZr alloy by HIPing at 555°C for 2 hours [91]. One of the tiles was lost during final machining.

Results of electron beam loading of the module FT 122 are presented in Figure A5.3 - 18 and Figure A5.3 - 19.

The module survived successful by 1000 cycles of loading at an absorbed power density of 1.45 MW/m^2 and 200 cycles at 1.9 MW/m^2. Figure A5.3 - 18 shows the surface temperature increase in the center of each tile with increasing of loads. The behaviour of average temperatures of each tile are presented in Figure A5.3 - 19. During 200 cycles the temperature were constant. Failure of the tile 1 occurred during the 1st cycle of thermal fatigue test at absorbed power density of 2.6 MW/m^2.

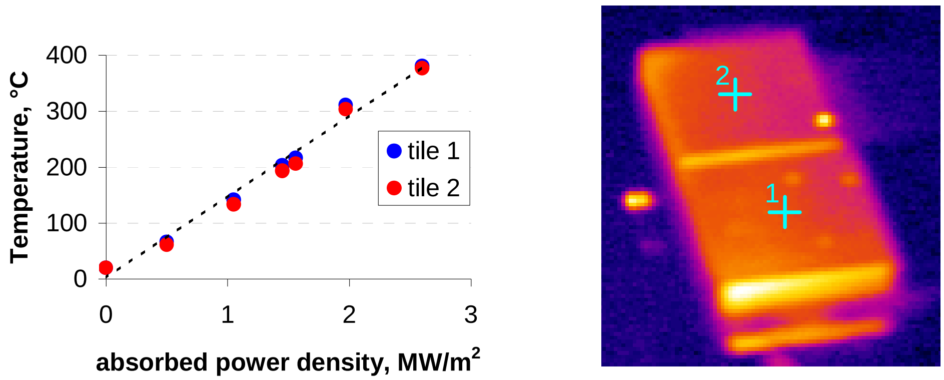

Figure A5.3 - 18. Screening test of the Be module FT 122

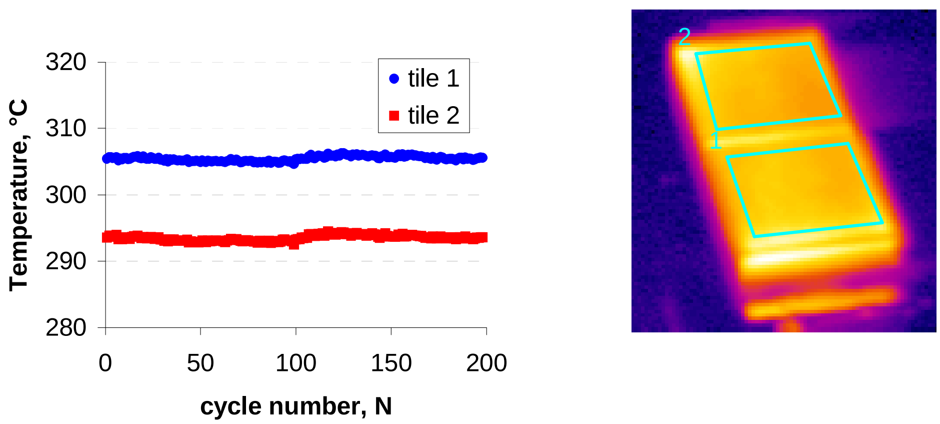

Figure A5.3 - 19. Thermal fatigue test of the Be module 122 at absorbed power density of 1.9 MW/m^2

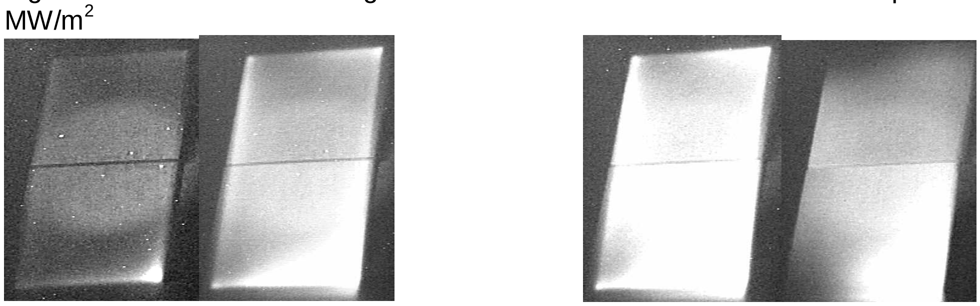

Figure A5.3 - 20. Failure of the Be module FT 122 during 1st cycle of thermal fatigue test at absorbed power density of 2.6 MW/m^2

Appendix to Chapter 5.4

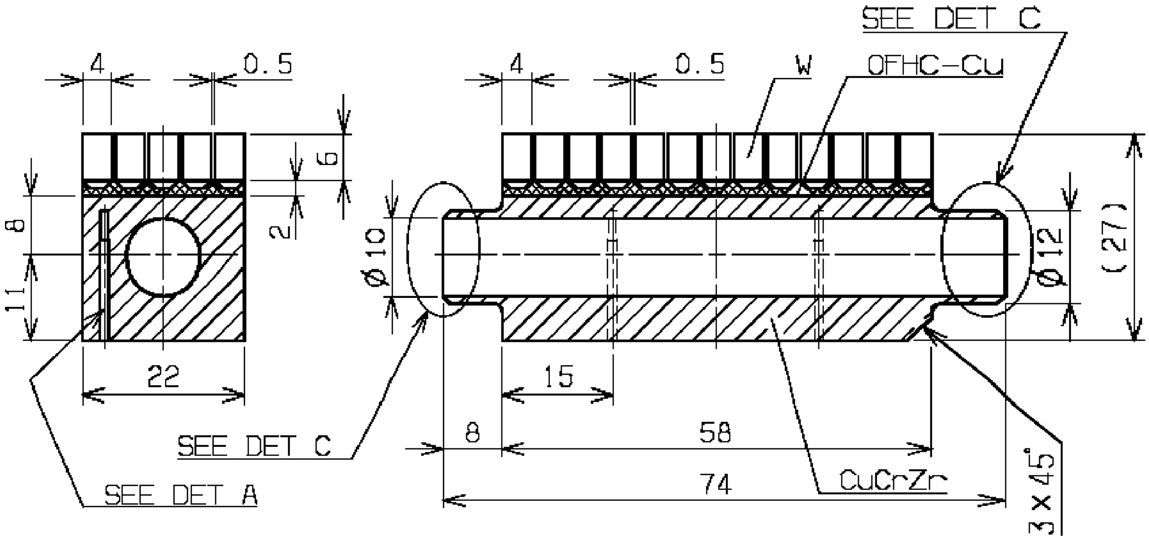

Figure A5.4-1. Drawing of W-macrobrush FT 83

Table A5.4-1. Scheme and results of testing of the modules FT 83-3, -5, -8

Loading type	Incident power density, MW/m^2	Absorbed power density, MW/m^2	Loaded area, mm^2	Result
FT 83-3 non-irradiated				
Screening	3-14.7	1.6-8.2	22x58	Successful
Thermal fatigue, 1000 cycles	14.7	8.2	22x58	Successful
Screening	15-24.5	13.4	22x58	Successful
Thermal fatigue, 1000 cycles	24.6	13.5	22x58	Successful
FT83-8 PARIDE 3				
Screening	1-18.2	0.6-10	22x58	Successful
Thermal fatigue, 1000 cycles	18.2	10	22x58	Overheating on water inlet side
FT83-5 PARIDE 4				
Screening	1.8-18.2	1-10	22x58	Successful
Thermal fatigue, 1000 cycles	18.2	10	22x58	Overheating on water inlet side
Screening	24.9	13.7	22x58	Successful
Thermal fatigue, 1000 cycles	24.9	13.7	22x58	Re-arrangement of temperature distribution
Screening	27.2	15	22x58	Successful

Table A5.4 - 2. Scheme and results of testing of the CFC modules FT 85-9, -11, -12

Loading type	Incident power density, MW/m^2	Absorbed power density, MW/m^2	Loaded area, mm^2	Result
FT 85-9 non-irradiated				
Screening	1-11		22x58	
Thermal fatigue, 1(cycles	11.3	10.6	22x58	No failure
Screening	11-20		22x58	
Thermal fatigue, 1(cycles	20	19.4	22x58	No failure
Thermal fatigue, 4(cycles	24.4	23.5	22x58	Continuous increase of temperature
FT 85-11 PARIDE 3				
Screening	1.2-13.4	1.1-11.8	22x58	
Thermal fatigue, 1000 cycles	13.4	11.8	22x58	Decrease of surface temperatures due to annealing effect
Screening	1.2-19.2	11.3-14.2	22x58	
Thermal fatigue, 1000 cycles	17.87	15.1	22x58	Decrease of surface temperatures due to annealing effect
Screening	19.2-23.5	16.2-19.5	22x58	Beginning of surface erosion
Thermal fatigue, 1000 cycles	23.5	19.5	22x58	At the beginning decrease of surface temperatures due to annealing effect; after 200 cycles increase of surface temperature due to progressive failure
FT 85-12 PARIDE 4				
Screening	1.2-13.4	1.1-11.2	22x58	
Thermal fatigue, 1000 cycles	13.4	11.5	22x58	Decrease of surface temperatures due to annealing effect
Screening	1.2-19.2	1.1-16.1	22x58	
Thermal fatigue, 1000 cycles	17.5	14.8	22x58	Decrease of surface temperatures due to annealing effect
Screening	21.5	18.0	22x58	Beginning of surface erosion

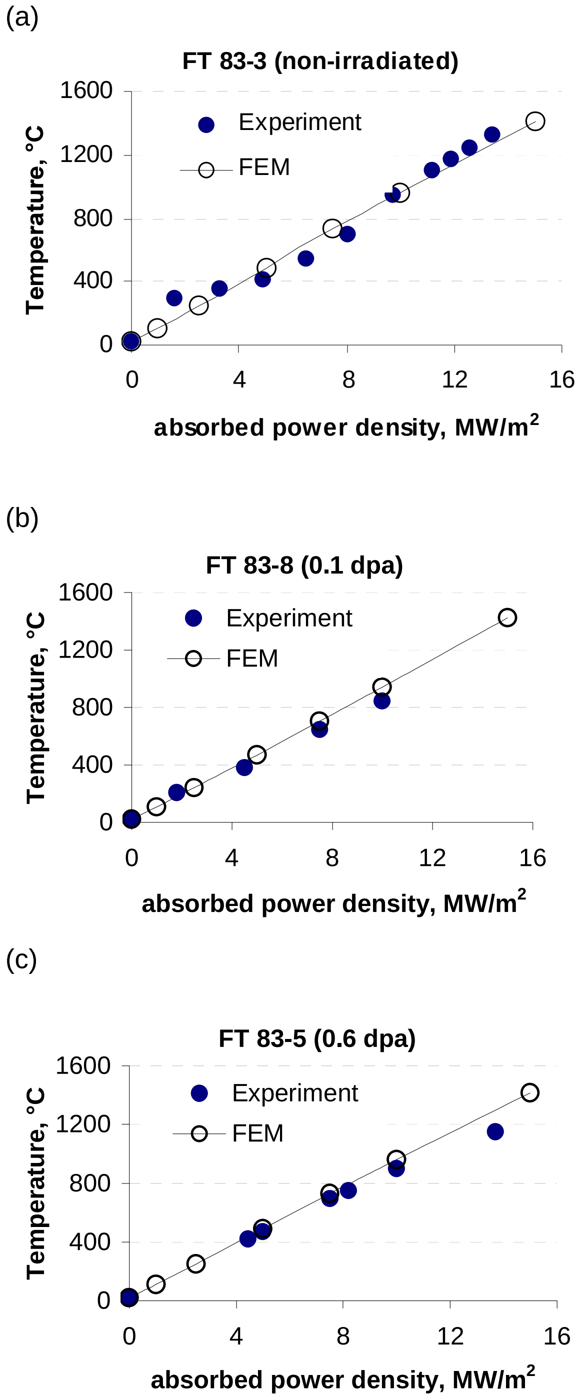

Figure A5.4 - 2. FEM calculations and experimental temperature during screening test of the modules FT 83-3 (non-irrad.), -8 (0.1 dpa), -5 (0.6 dpa)

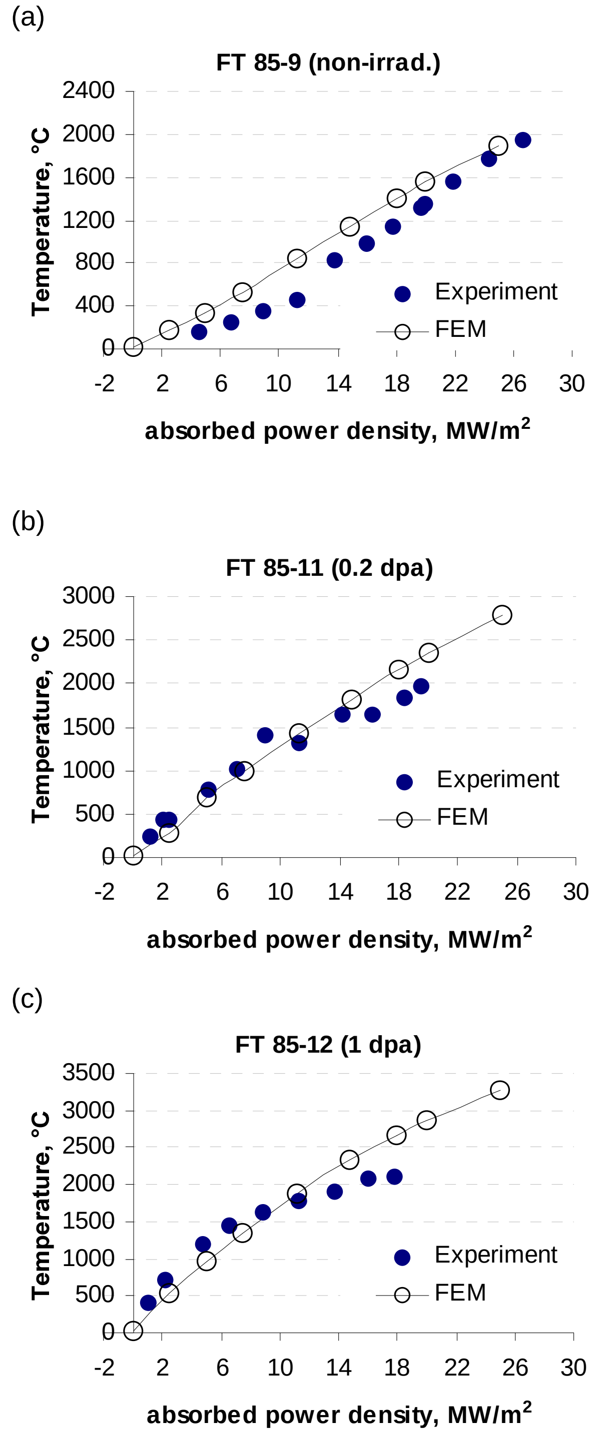

Figure A5.4 - 3. FEM calculations and experimental temperature during screening test of the modules FT 85-9 (non-irrad.), -11 (0.2 dpa), -12 (1 dpa)

Thermal fatigue performance of the non-irradiated W-1%La_2O_3 module FT 83-3

Several thermal fatigue tests were carried out with the non-irradiated module FT 83-3 and irradiated modules FT 83-8 (0.1 dpa) and FT 83-5 (0.6 dpa).

In Figure A5.4 - 4 - Figure A5.4 - 6 the results of thermal cycling of the non-irradiated module FT 83-3 are presented. Surface temperature stays at the same level during 1000 cycles at absorbed power density of 8.2 MW/m2 (Figure A5.4 - 4). The deviation of temperature along the line 1-1 (infrared image in Figure A5.4 - 4) connects with castellated armour (4 x 4 mm2) joined to heat sink. The areas with higher temperature were not observed.

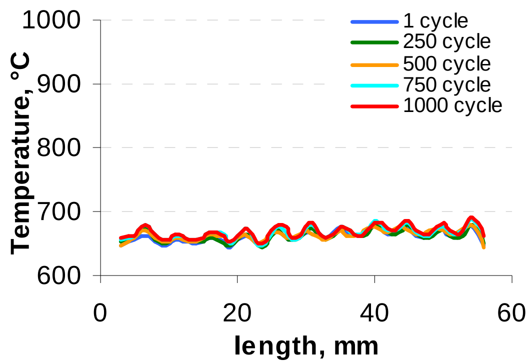

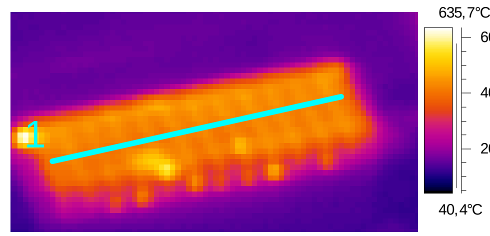

Figure A5.4 - 4. Thermal fatigue test of the module FT 83-3 at absorbed power density of 8.2 MW/m^2

Thermal fatigue of the module FT 83-3 at absorbed power density of 13.5 MW/m^2 was carried out. At beginning of cycling loading (first 200 cycles) slight temperature increase on the surface was observed. This effect can be connected with changing of surface emissivity (Figure A5.4 - 5a). In Figure A5.4 - 5b temperature fields on the module surface during the same thermal fatigue test are presented. Significant overheating appeared in the area near water inlet and outlet, which connects with scanning mode of electron beam in the facility JUDITH.

Thus, the analysis of date during infrared observation showed that the module FT83-3 by thermal cycling at 13.5 MW/m^2 heated up uniform on all of surface with the exception of edge areas. This characterizes good thermal heat properties around the module surface.

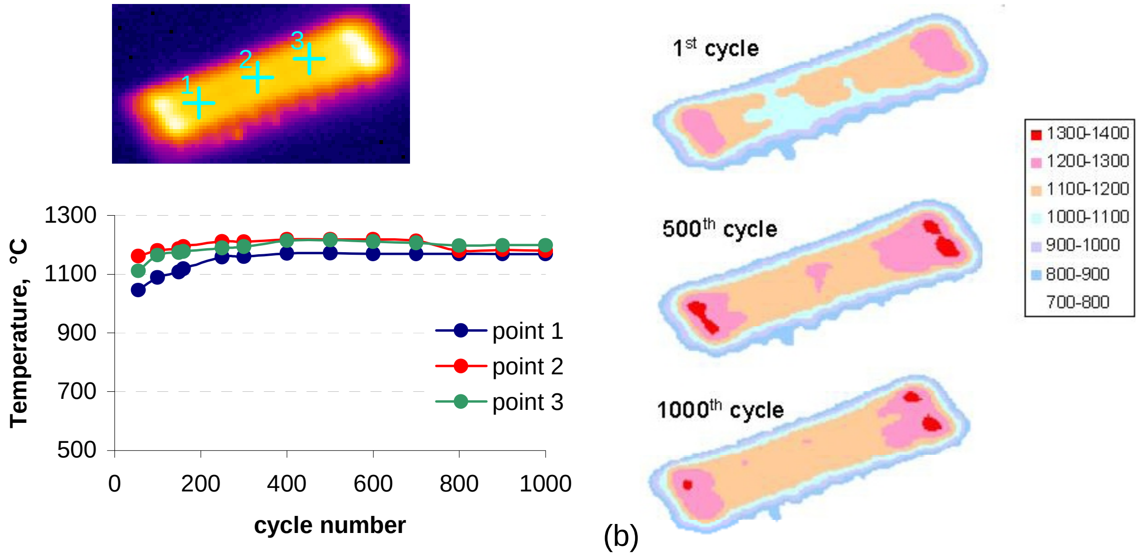

(a) (b)

Figure A5.4 - 5. Thermal fatigue test of the non-irradiated module FT 83-3 at absorbed power density of 13.5MW/m2: (a) surface temperature and (b) temperature fields

By metallographic analysis of the module FT 83-3 after thermal fatigue loading the cracks at the border of OFHC interlayer and CuCrZr heat sink were found (Figure A5.4 - 6). Probably cracks formed and expanded during thermal fatigue test. Moreover, Figure A5.4 - 6b demonstrates pores in structure of material OFHC, which are evidently the structure defects formed during manufacturing process. In W-1%La_2O_3 alloy no defects or cracks in structure were found.

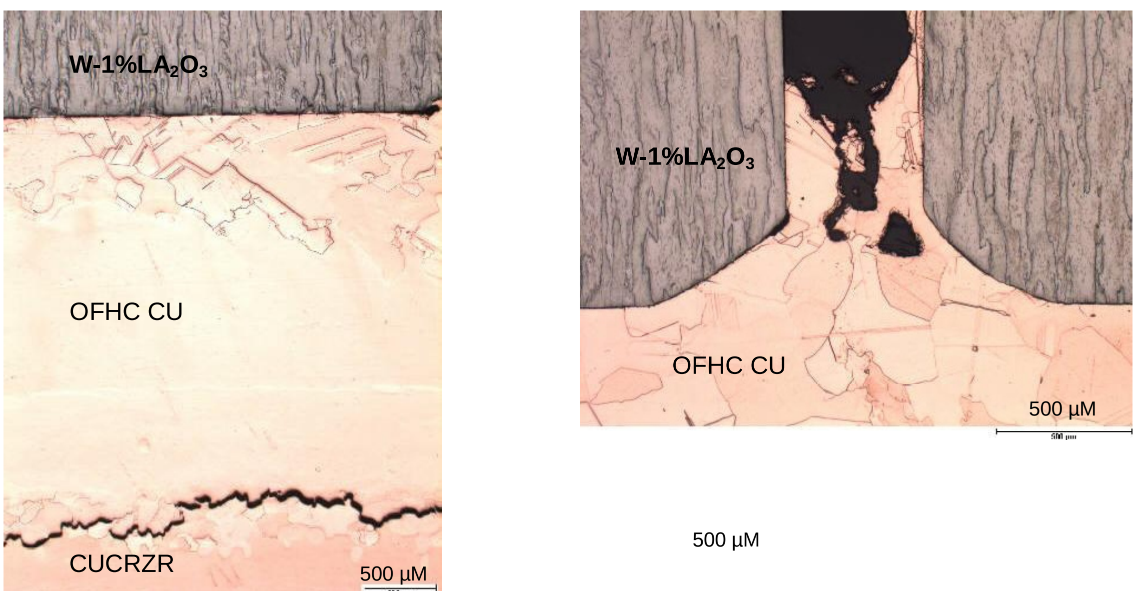

Figure A5.4 - 6. Metallographic analysis of the non-irradiated module FT 83-3 after thermal fatigue tests

Thermal fatigue performance of the W-1%La_2O_3 module FT 83-5 (0.6 dpa)

Irradiated at 0.6 dpa module FT 83-5 was tested at absorbed power densities of 10 and 13.7 MW/m^2 during 1000 cycles each.

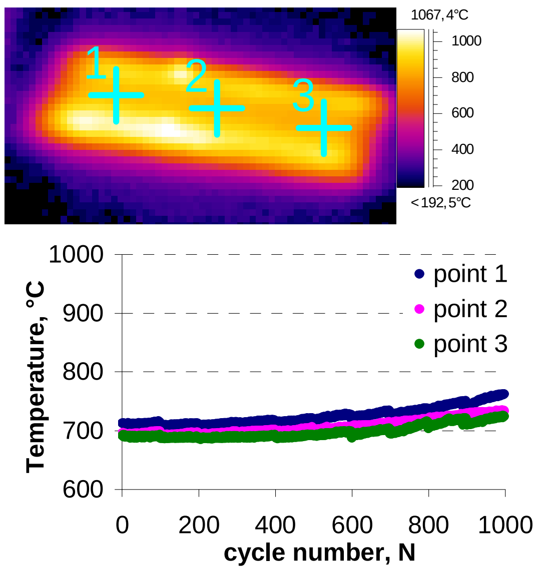

Figure A5.4 - 7. Thermal fatigue tests of the module FT 83-5 (0.6 dpa) at 10MW/m^2

Figure A5.4 - 7 demonstrates surface temperature increase in different points during 1000 cycles at 10 MW/m^2. Temperature raise achieved about 80°C in the area over cooling tube during cycling. In edge areas the temperature increase is more significant as shown in the infrared image (Figure A5.4 - 7)

By next loading during 1000 cycles at absorbed power density of 13.7 MW/m2 surface temperature of the module FT83-5 were fixed in points 1, 2 and 3 (Figure A5.4 - 8). Obviously, the surface temperature of point 1 increased significantly (in about 200°C), whereas, the temperatures in points 2 and 3 stayed at the similar levels.

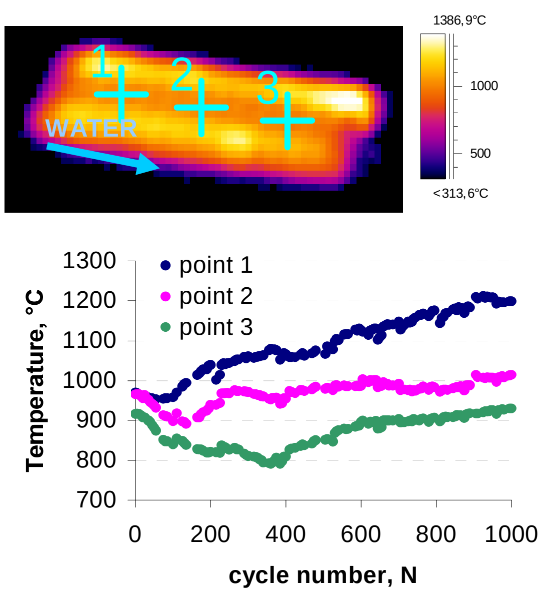

Figure A5.4 - 8. Thermal fatigue tests of the module FT 83-5 (0.6 dpa) at 13.7 MW/m2

Evolution of temperature fields on the surface of the module FT 83-5 during the last thermal cycling at 13.7 MW/m2 is presented in Figure A5.4 - 9. It is clearly seen that surface overheating and progressive temperature rise evolves in the area neat water inlet. The position of the cooling tube was clearly seen in temperature fields picture only after the first 100 cycles. At the same time surface overheating was observed in right upper corner of the module (area A). Then process of decrease of heat transfer starts in area B (Figure A5.4 - 9). Overheating in area B increased and reached 400°C after 1000 cycles of loading. At that evolution and expansion of overheated area impacts slightly on temperature increase of areas with good heat transfer (right half of the module). Overheating of area A, which was observed early, became low. It means that in the area the temperature decreased during thermal cycling. It can be either an effect of surface emissivity change and of an heat transfer improvement inside of a module due to recovering of the same structure imperfections during high heat loads.

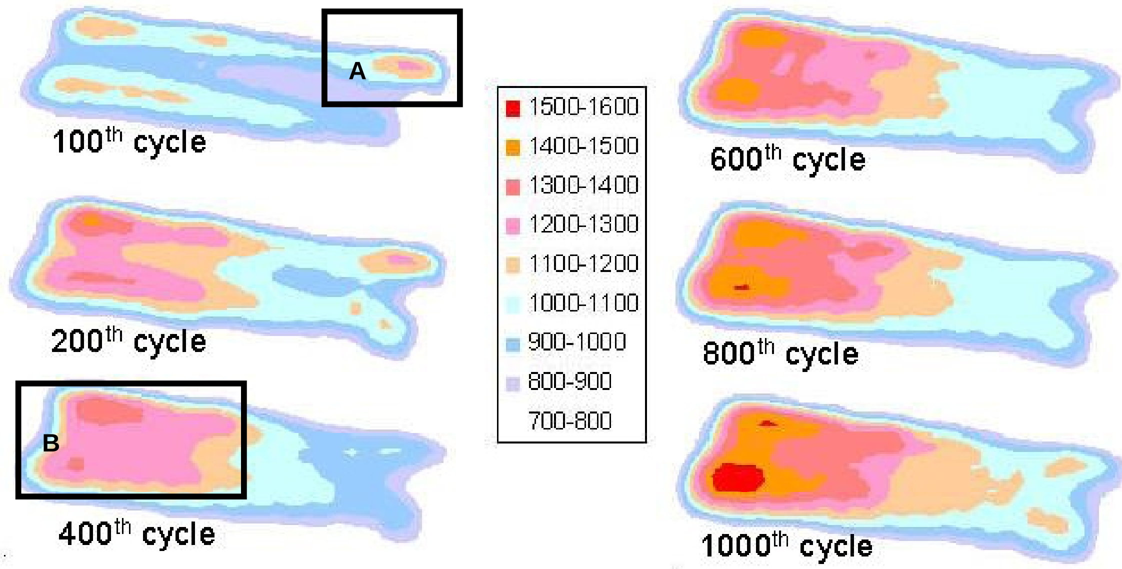

Figure A5.4 - 9. Temperature fields of the module FT 83-5 (0.6 dpa) during thermal fatigue test at absorbed power density of 13.7 MW/m^2

CFC flat tile mock-ups FT 85

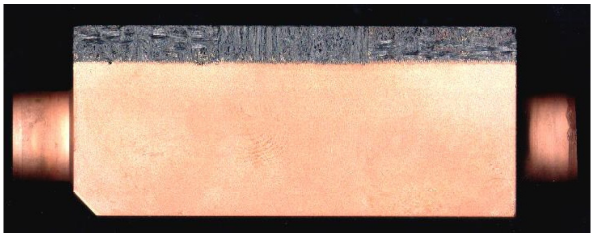

(a) before testing

(b) after irradiation and testing

Figure A5.4 - 10. module FT 85-11

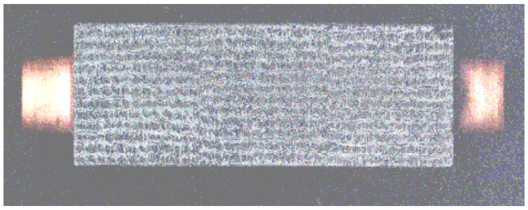

(a) before testing

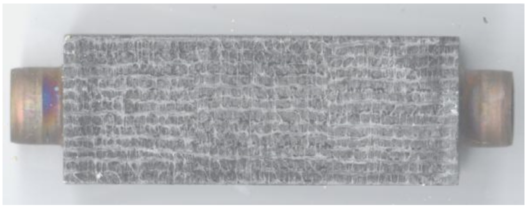

(b) after irradiation and testing

Figure A5.4 - 11. module FT 85-12

Thermal fatigue performance of the non-irradiated CFC module FT 85-9

The thermal behaviour of the non-irradiated module FT85-9 during the screening is presented in Figure A5.4 - 12. At low HHF load of absorbed power density of 10.6 MW/m^2 the temperature distribution along the module (line 1-1) is even. At the power density of 19.4 MW/m^2 the temperature on the left part of the tile 3 goes slightly up, but by next step at 23.5 MW/m^2 the temperature is increasing on the tile 1 from the right side (Figure A5.4 - 12, infrared images). On the that spot the surface suffered such an overheating that made it necessary to terminate the experiment.

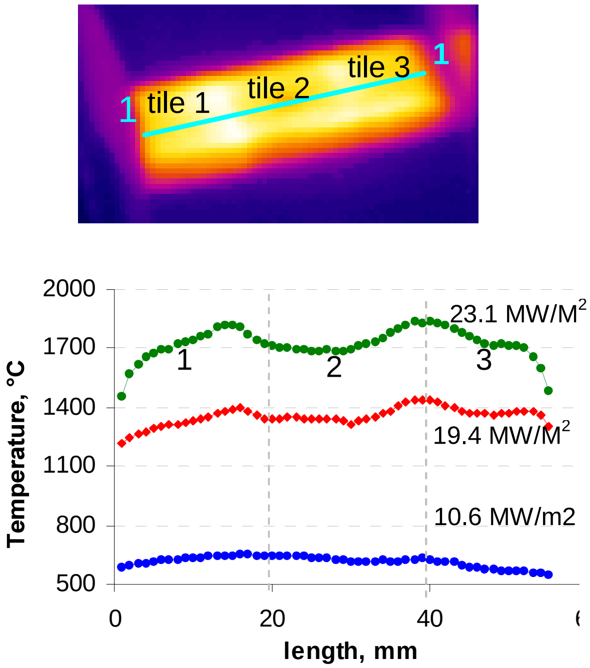

Figure A5.4 - 12. Temperature distribution at screening tests for the module FT 85-9

At these loads thermal fatigue cycling was also carried out (Table A5.4-2). At 10.6 and 19.4 MW/m^2 of HHF load the module sustained 1000 cycles. At 23.5 MW/m^2 400 cycles were applied until the significant overheating was detected on the tile 1 (temperature in area A exceeded 2000°C) and sublimation of armour material.

Figure A5.4 - 13 presents a metallographic image of zone, where CFC sublimation occurred. The sublimation was a result of local surface overheating (sublimation zone corresponds to black area A of the surface of the module FT 85-9 after electron beam loading presented in Figure 12). The depth of sublimating zone is about 1-2 mm.

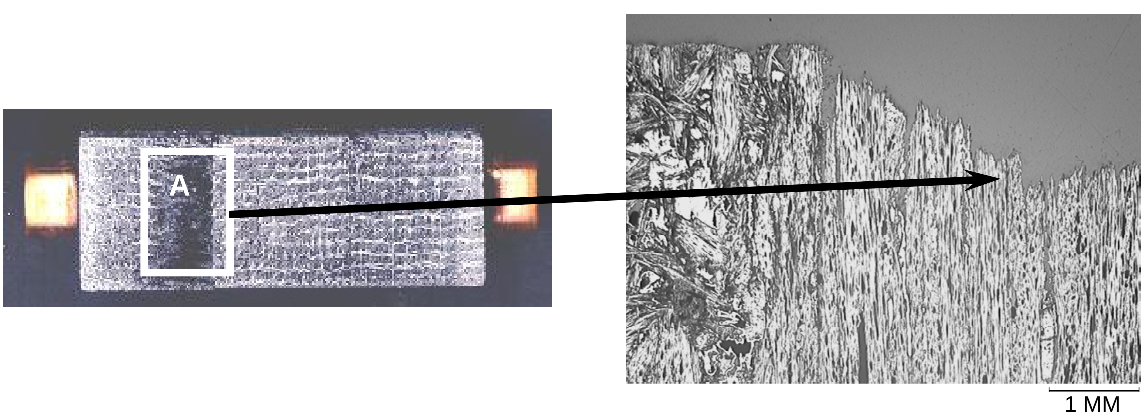

Figure A5.4 - 13. Sublimation of CFC armour of the module FT 85-9 during heat loading at 23. MW/m^2

Figure A5.4 - 14a demonstrates the temperature fields evolution during 400 cycles of this loading. Overheated zone on the tile 1 becomes visible after 200 cycles and expands along the internal edge of tile. The overheating is about 200°C. By 400 cycle overheated zone expanded well and occupied more than half of the tile. The overheating occurred at about 400°C. Figure A5.4 - 14b shows the temperature increase in center of each tile during 400 cycles at the same thermal fatigue test. Clear and significant temperature increase was observed on the tile 1.

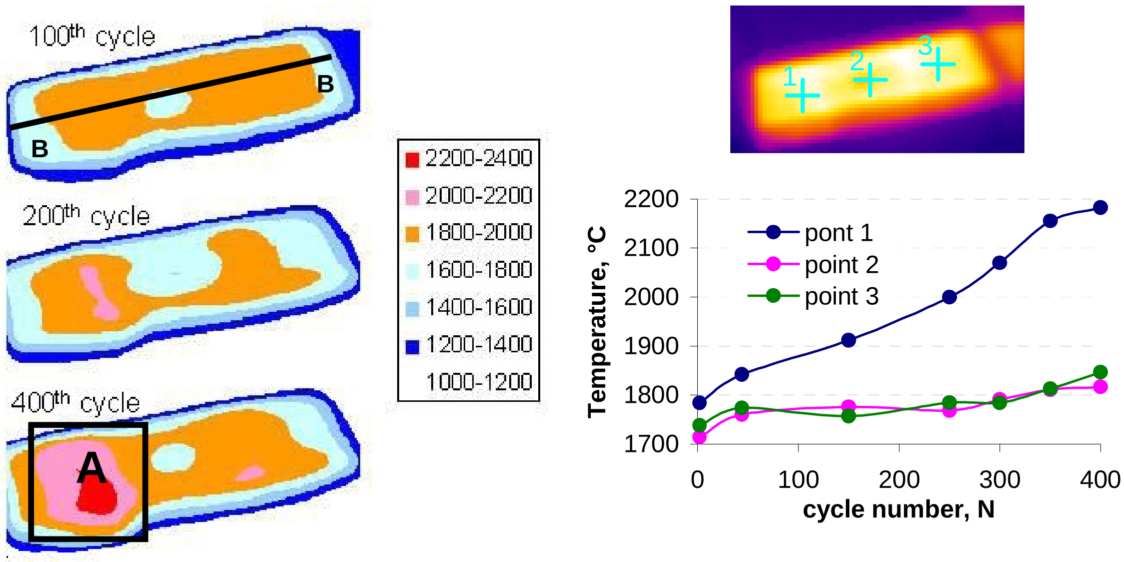

Figure A5.4 - 14. Thermal fatigue test of the module FT 85-9 at 23.1 MW/m^2: (a). Surface temperature fields, (b). Surface temperature increase during loading

Figure A5.4 - 15 demonstrates the images of section for the module FT 85-9 after high heat flux testing. Presented images show the most possible damages in structure of a CFC module.
The damages in area of HIPed zone joined Cu-heat sink and CFC tiles is shown in Figure A5.4 - 15a. During manufacturing the CFC surface is first coated with thin Ti layer for carbide formation (AMC®) and second brazed with OFHC-Cu (more detail see in Chapter 2.4.2). The cracks, which occur probably during thermal fatigue loading, extend both in carbides layer (1) and on the border between TiC and OFHC-Cu interlayer (2). Figure A5.4 - 15b shows a crack extended on the border between OFHC-Cu and CuCrZr heat sink.

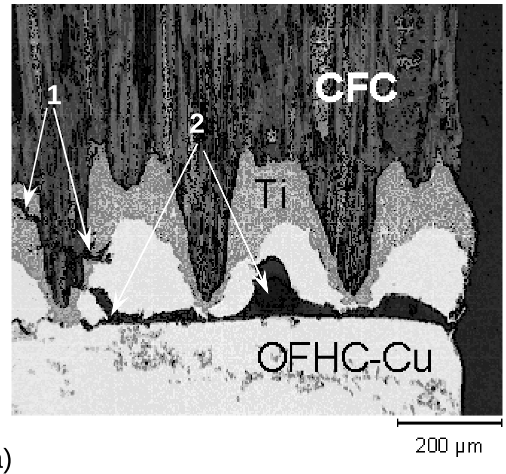

(a)

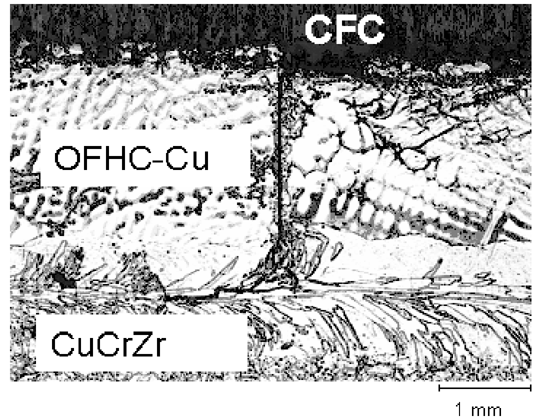

(b)

Figure A5.4 - 15. Cracks in structure of the CFC module FT 85-9

Thermal fatigue performance of the module FT 85-12 (1 dpa)

The module FT 85-12 irradiated at 1 dpa was tested according description in Table 2 (Appendix 5.3). Two series of thermal fatigue loadings at 11.5 and 14.8 MW/m2 were performed. The surface temperature decrease due to CFC annealing during loading at 11.5 MW/m2 is clearly observed in Figure A5.4 - 16. Temperature was measured in the center of each tile during 1000 cycles. Figure A5.4 - 17 shows the temperature fields during 1000 cycles at 14.8 MW/m2. Overheated area on the edge became smaller due to annealing of CFC. No temperature increase on the surface was observed.

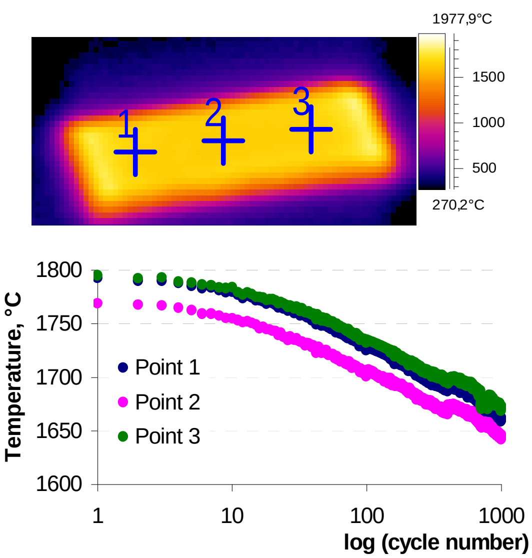

Figure A5.4 - 16. Temperature of the irradiated module FT 85-12 (1 dpa) during thermal fatigue test at 11.5 MW/m2

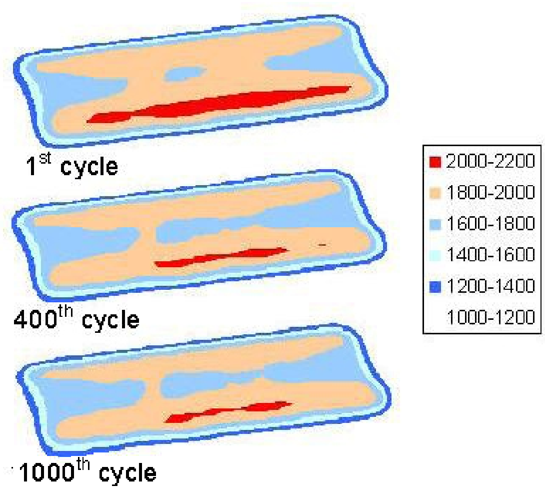

Figure A5.4 - 17. Temperature fields of the irradiated module FT85-12 (1 dpa) during thermal fatigue test at 14.8 MW/m2

1. High heat flux tests of primary wall mock-ups. Final report EFDA. 2003
2. S. Deschka. Thermomechanisches Verhalten gefügter Divertormodule unter fusionsrelevanten Belastungen. Dissertation. RWTH Aachen.

Curriculum Vitae

PERSONAL DETAILS

Name:	Anna Kapustina
Address:	Bocksgasse 9 52428 Jülich Germany
E-mail:	kapustina@mail.ru

Day of birth	September 3, 1975 in Sewerodwinsk (Russia)
Nationality	Russian
Field of specialization	New materials science

EDUCATION

February 2001- June 2004	**Postgraduate studies** Forschungszentrum Juelich, Germany Insitut für Werkstoffe und Verfahren der Energietechnik
August 1992- June 1997	**Technical University of Nizhny Novgorod (Russia)** Material Studies and High Temperature Technologies department awarded diploma with honor

INTERNSHIPS

March - May, 1999	**Postgraduate internship in Germany**: Rittmeyer Feintechnik (Muenster) - precise mechinic FH Muenster, Laser Zenterum (Steinfurt) - laser technologies Thyssen Krupp AG (Dortmund) - new material studies
January - June, 1997, July-September, 1996	Machine building plant «Normal» (Nizhny Novgorod) -material science studies
July-September, 1995	Automobile building plant «Sevdormash» (Severodvinsk) - Ingeneer in construction bureau
July -September, 1993	Plant «Zevs» (Nizhny Novgorod) - material studies

WORK EXPERIENCE

February 2001-Juli 2004	**Forschungszentrum Juelich, Germany** Science staff member
July 1997 –2001	**Technical University of Nizhny Novgorod** Junior science staff member